An Investigation of Bone Image Texture Analysis for Predicting Fracture Risk

by

Farhana Jahan

A Thesis submitted to the Faculty of Graduate Studies
in partial fulfillment of the requirements for the degree of

Master of Science

Department of Computer Science
The University of Manitoba
Winnipeg, Manitoba
Canada

Abstract

Osteoporosis is caused by loss of bone mineral content, which leads to bone fractures or structural deformations of bone. Osteoporosis usually occurs when people get older, after menopause in women, or it can be caused by a lack in the intake of a sufficient amount of calcium and vitamin D. Until recently, osteoporosis was considered to be an unavoidable part of aging, but today, approved and effective treatments can be used to deal with the consequences. At present, determination of risk of bone abnormalities is done by measuring the density of bone (largely determined by calcium content). Dual energy X-ray Absorptiometry (DXA) is the gold standard technique for measuring bone mineral density (BMD). Even though BMD is one of the principal determinants of bone strength, BMD measurements do not give information about variation of trabecular structure of bone. That's why DXA alone has limited ability to predict who will sustain an osteoporotic fracture. To predict fracture risk of patients, the texture analysis of the DXA images is of interest as a measure to predict fracture in addition to BMD.

This thesis focuses on the application of texture analysis to digital images of bone scans of patients at risk of fracture and osteoporosis. Texture analysis was performed by analyzing the variation of grey level patterns of pixels of DXA images. Texture analysis of such images will give an idea of the variation of grey scale patterns of pixels between normal and osteoporotic DXA images of bone. Existing texture analysis measures such as contrast measures of co-occurrence matrices and mean slope value

of fractal dimension based measure are used to analyze the texture of DXA images. An alternative partitioning technique is proposed as a measure of the texture analysis.

Contents

Abstract ii
Table of Contents v
List of Figures vi
List of Tables ix
Acknowledgments xii
Dedication xiii

1 Introduction **1**
1.1 Background 1
1.1.1 Medical Imaging 1
1.1.2 Basic Bone Structure 2
1.1.3 Compact Bone 3
1.1.4 Trabecular Bone 4
1.1.5 Osteoporosis 4
1.1.5.1 Causes of Osteoporosis 7
1.1.6 Dual Energy X-ray Absorptiometry (DXA) 8
1.1.7 Texture Analysis 10
1.1.8 Statistical Methods and Tests Used for Analysis 12
1.1.8.1 Mean, Standard Deviation and T-test 12
1.2 Problem Statement 16
1.3 Hypothesis 18
1.4 Chapter Outline 19

2 Literature Review **20**
2.1 Literature Review on Osteoporosis and Fracture Risk 22
2.1.1 Low Bone Mineral Density and Fracture Burden in Postmenopausal Women 22
2.1.2 Contribution of clinical risk factors to bone density-based absolute fracture risk assessment in postmenopausal women 23
2.1.3 Computerized Radiographic Analysis of Osteoporosis 24

2.2 Literature Review on Image Segmentation 25
2.2.1 Efficient Graph-Based Image Segmentation 25
2.2.2 Image Segmentation Using Colour And Texture Features . . . 26
2.2.3 Adaptive Perceptual Colour-Texture Image Segmentation . . . 26
2.2.4 Normalized Cuts and Image Segmentation 27
2.2.5 Content-Based Image Retrieval Using Rectangular Segmentation 27
2.3 Literature Review on Quad-Tree Segmentation 29
2.3.1 Quad-Tree Segmentation for Texture-Based Image Query . . . 29
2.3.2 Quad-Tree Decomposition Texture Analysis in Paper Formation Determination 30

3 Texture Measures Based on Existing Methods 31
3.1 Region of Interest (ROI) 37
3.2 Co-occurrence Matrices 41
3.3 Co-occurrence Matrix Based Measure 43
3.4 Fractal Dimension 51
3.5 Fractal Dimension Based Measure 55
3.6 Two Variable Discriminant Tests 57
3.7 Statistical Analysis of the Experimented Results of ROI Images . . . 59
3.7.1 F-ratio Test 59
3.7.2 Mean, Standard Deviation and T-test 61
3.8 Summary 67

4 Alternative Texture Measures Based on Partitioning 68
4.1 Segmentation And Texture Analysis of DXA scan Image 69
4.1.1 Segmentation Using Quad-Tree Decomposition 69
4.1.2 A Rectangular Segmentation Technique 72
4.2 A Proposed Gray Level Variation Measure Based on Partitioning . . 75
4.3 The Proposed Partitioning Method 77
4.4 Validation of the Proposed Partitioning Method 81
4.5 Texture Analysis of DXA scan ROI Images Using The Proposed Partitioning Method 91
4.6 Two Variable Discriminant Tests 93
4.7 Statistical Analysis of the Experimented Results of ROI Images . . . 95
4.7.1 Mean, Standard Deviation and T-test 96
4.7.1.1 Normal vs. Osteoporotic Hip ROI 99
4.7.1.2 Normal vs. Osteoporotic Spine ROI 100
4.8 Summary 101

5 Conclusion 103

A Numerical Results 108

List of Figures

1.1 Radiological appearance of cortical and cancellous bone. (Image obtained from Nather et al [5].). 3
1.2 Compact bone having Haversian canal in each osteon. (Image obtained from Nather et al [5].). 5
1.3 Internal structure of bone with normal bone loss and bone having osteoporosis. (Image obtained from Bupa [6]). 6
1.4 The orientation of the surface can be determined from the variations of texture of the image. (Image obtained from Mihran [18]). 11
1.5 Sample DXA scan images of (a) total hip and (b) lumbar spine. (Images courtesy of the Manitoba Bone Density Program [26]). 17

3.1 DXA images of normal total hip (Images courtesy of the Manitoba Bone Density Program [26]). 33
3.2 DXA images of osteoporotic total hip (Images courtesy of the Manitoba Bone Density Program [26]). 34
3.3 DXA images of normal lumbar spine (Images courtesy of the Manitoba Bone Density Program [26]). 35
3.4 DXA images of osteoporotic lumbar spine (Images courtesy of the Manitoba Bone Density Program [26]). 36
3.5 DXA scan image of (a) total hip and (b) lumbar spine, with ROI. . . 38
3.6 Left two columns represents the normal and right two columns represents the osteoporotic hip ROIs of Figures 3.1 and 3.2. 39
3.7 Left two columns represents the normal and right two columns represents the osteoporotic spine ROIs of Figures 3.3 and 3.4. 40
3.8 Directions used for (a) the distance (b) the matrix entries 42
3.9 The process block diagram of the co-occurrence matrix based measures. 45
3.10 Left side plots for contrast and right side plots for homogeneity of the hip ROIs, for the given d values, of Figure 3.6. N, O, N_M and O_M represents the normal, osteoporotic, mean of normal and osteoporotic of hip ROIs, respectively. 47

3.11 Left side plots for contrast and right side plots for homogeneity of the hip ROIs, for the given d values, of Figure 3.6. N, O, N_M and O_M represents the normal, osteoporotic, mean of normal and osteoporotic of hip ROIs, respectively. 48
3.12 Left side plots for contrast and right side plots for homogeneity of spine ROIs, for the given d values, of Figure 3.7. N, O, N_M and O_M represents the normal, osteoporotic, mean of normal and osteoporotic of spine ROIs, respectively. 49
3.13 Left side plots for contrast and right side plots for homogeneity of spine ROIs, for the given d values, of Figure 3.7. N, O, N_M and O_M represents the normal, osteoporotic, mean of normal and osteoporotic of spine ROIs, respectively. 50
3.14 (a) Octagonal 7-pixel wide neighbourhood. (b) Distance of pixels of Figure (a) from the center of the neighbourhood [19]. 53
3.15 Two fragment of an image [19]. 54
3.16 Distance and brightness data of the neighbourhood pixels of the image fragment of Figure 3.15 [19]. 54
3.17 The process block diagram of the fractal dimension based measures. . 56
3.18 Scatter plots of the results of fractal dimension for all ROI images of Figures 3.6 and 3.7. N, O, N_M and O_M represents the normal, osteoporotic, mean of normal and osteoporotic of ROI images, respectively. 57
3.19 Plotted the results of homogeneity and contrast obtained using the co-occurrence matrix based method for normal and osteoporotic ROIs of Figures 3.6 and 3.7 in (a) and (b), respectively. 58

4.1 Sample DXA image of hip and the results of quad-tree decomposition on that image. (Images courtesy of the Manitoba Bone Density Program [26]. (c) Quad-tree Decomposition With the DXA image I, threshold 0.30 and mindim 8 (d)With the DXA image I, threshold 0.30 and mindim 16. 72
4.2 Results of the proposed rectangular segmentation with mindim 8 and 16 and threshold 1.2. (Images courtesy of the Manitoba Bone Density Program [26].) 74
4.3 The flowchart of the proposed partitioning method. 80
4.4 Left column represents the normal bone images and right column represents the abnormal bone images. 83
4.5 Plots of the results of proposed method based on partitioning for all sample images of Figure 4.4. The Y-axis shows the results of γ_3 and the blue marker indicates the threshold (T) of γ_3. 86

4.6 Left side plots for contrast and right side plots for homogeneity of the sample images, for the given d values, of Figure 4.4. *Normal*, *Abnormal*, N_M and A_M represents normal, abnormal, mean of normal and abnormal of sample images, respectively. 89
4.7 Left side plots for contrast and right side plots for homogeneity of the sample images, for the given d values, of Figure 4.4. *Normal*, *Abnormal*, N_M and A_M represents normal, abnormal, mean of normal and abnormal of sample images, respectively. 90
4.8 2-sample scatter plot of the results of fractal dimension for the sample images of Figure 4.4. *Normal*, *Abnormal*, N_M and A_M represents normal, abnormal, mean of normal and abnormal of sample images, respectively. 91
4.9 Plotted the results of γ_3 obtained using the proposed partitioning method, where m=16, of normal and osteoporotic ROIs of Figures 3.6 and 3.7 in (a) and (b), respectively, using the scatter plots. N, O, N_M and O_M represents the normal, osteoporotic, mean of normal and osteoporotic of ROIs, respectively. 93
4.10 Plotted the results of γ_2 and γ_3 obtained using the proposed partitioning method, where m=16, of normal and osteoporotic ROIs of Figures 3.6 and 3.7 in (a) and (b), respectively. 94

List of Tables

3.1 F-ratio test results of contrast for all hip ROIs of Figures 3.6. The critical value ($-t_\alpha$) for df=(9,9), and α=0.05, is 3.1789. 61

3.2 F-ratio test results of contrast for all spine ROIs of Figures 3.7. The critical value ($-t_\alpha$) for df=(9,9), and α=0.05, is 3.1789. 61

3.3 Mean, standard deviation and t-test results of contrast for all hip ROIs of Figures 3.6. $\bar{x}$ and $\bar{y}$ represent the mean and S_x, S_y represent the standard deviation of the normal and osteoporotic hip ROIs, respectively. The critical value ($-t_\alpha$) for df=18, and α=0.05, is 2.101. . . . 63

3.4 Mean, standard deviation and t-test results of contrast for all spine ROIs of Figures 3.7. $\bar{x}$ and $\bar{y}$ represent the mean and S_x, S_y represent the standard deviation of the normal and osteoporotic spine ROIs, respectively. The critical value ($-t_\alpha$) for df=18, and α=0.05, is 2.101. 63

3.5 Mean, standard deviation and t-test results of the homogeneity for all hip ROIs of Figures 3.6. $\bar{x}$ and $\bar{y}$ represent the mean and S_x, S_y represent the standard deviation of the normal and osteoporotic hip ROIs, respectively. The critical value ($-t_\alpha$) for df=18, and α=0.05, is 2.101. 64

3.6 Mean, standard deviation and t-test results of the homogeneity for all spine ROIs of Figures 3.7. $\bar{x}$ and $\bar{y}$ represent the mean and S_x, S_y represent the standard deviation of the normal and osteoporotic spine ROIs, respectively. The critical value ($-t_\alpha$) for df=18, and α=0.05, is 2.101. 64

3.7 Mean, standard deviation and t-test results that obtained using the results of fractal dimension for all normal and osteoporotic ROIs of Figures 3.6 and 3.7. $\bar{x}$ and $\bar{y}$ represent the mean and S_x, S_y represent the standard deviation of the normal and osteoporotic ROIs, respectively. The critical value ($-t_\alpha$) for df=18, and α=0.05, is 2.101. 66

4.1 Results of β obtained using the proposed measures based on partitioning for all sample images in Figure 4.4. 84

4.2 Results obtained using the proposed measures based on partitioning where m=10, for all images in Figure 4.4. 85
4.3 Results obtained using the proposed measures based on partitioning where m=12, for all images in Figure 4.4. 85
4.4 Results obtained using the proposed measures based on partitioning where m=16, for all images in Figure 4.4. 85
4.5 Results of contrast and homogeneity obtained using the co-occurrence matrix based measures for all generated sample images, represents the normal and abnormal group of images, in Figure 4.4 at distance d=(1,1), d=(2,2), d=(0,1) and d=(0,2). 87
4.6 Results of contrast and homogeneity obtained using the co-occurrence matrix based measures for all generated sample images, represents the normal and abnormal group of images, in Figure 4.4 at distance d=(1,0), d=(2,0), d=(3,3) and d=(4,4). 88
4.7 Results obtained using fractal dimension based texture measures for all generated sample images, represents the normal and abnormal group of images, of Figure 4.4. 91
4.8 F-ratio results of γ_3 measures for all ROIs of Figures 3.6 and 3.7. The critical value ($-t_\alpha$) for df=(9,9), and α=0.05, is 3.1789. 96
4.9 Two-sample t-test results of γ_3 of the partitioning method for all ROIs of Figures 3.6 and 3.7. H indicates whether the hypothesis is accepted or not. The critical value ($-t_\alpha$) for df=18, and α=0.05, is 2.101. . . . 98
4.10 Mean, standard deviation and one-sample t-test results of γ_3 of the partitioning method for all ROIs of Figures 3.6 and 3.7. The critical value for df=18 and α=0.05, is 1.833 99

A.1 Results obtained using co-occurrence based texture measures for all hip ROI images in Figure 3.6 for distance d=(1,1), d=(2,2), d=(0,1) and d=(0,2). 109
A.2 Results obtained using co-occurrence based texture measures for all hip ROI images in Figure 3.6 for distance d=(1,0), d=(2,0), d=(3,3) and d=(4,4). 110
A.3 Results obtained using co-occurrence based texture measures for all spine ROI images in Figure 3.7 for distance d=(1,1), d=(2,2), d=(0,1) and d=(0,2). 111
A.4 Results obtained using co-occurrence based texture measures for all spine ROI images in Figure 3.7 for distance d=(1,0), d=(2,0), d=(3,3) and d=(4,4). 112
A.5 Results obtained using fractal dimension based texture measures for all ROI images of Figures 3.6 and 3.7. 113

A.6 Tabulated the results of β, γ_1, γ_2 and γ_3 that obtained using a proposed partitioning method, where m=16, of normal and osteoporotic hip ROIs of Figure 3.6. 114
A.7 Tabulated the results of β, γ_1, γ_2 and γ_3 that obtained using a proposed partitioning method, where m=16, of normal and osteoporotic spine ROIs of Figure 3.7. 115

Acknowledgments

I would like to begin by expressing my gratitude to my supervisor, Professor Desmond Walton, Department of computer Science, University of Manitoba, for accepting me as a master's student and for his guidance, comments, support and inspiration during the whole program. I wish to express my gratefulness to my supervisor, Department of Computer Science and Faculty of Graduate Studies of the University of Manitoba for all scholarships, awards and funding during my master's program. I would like to thank my thesis committee members, Dr. W. Leslie of St. Boniface General Hospital, Dr. Neil Arnason of Department of Computer Science, and Dr. Andrew L. Goertzen of Department of Radiology, Health Sciences Centre, for their valuable time, comments and suggestions. I am also thankful to all professors of Computer Science department, particularly Dr. Helen Cameron for her valuable suggestions, comments and encouragement.

Finally, I am grateful to my parents, husband and in-laws for their heartfelt support and sacrifice along the way to help make my dream come true.

This thesis is dedicated to my parents and husband.

Chapter 1

Introduction

1.1 Background

An important use of computers in medical imaging is to process digital images to display the information contained in the images in more useful forms. According to Bushberg et al. [1], the application of computers was introduced into the field of medical imaging during the early 1970s and since then computers have become integral to medical science. The focus of this thesis is medical imaging.

1.1.1 Medical Imaging

At the early stage, use of computers in medical imaging was mainly in nuclear medicine, to get a series of images of the organ-specific kinetics of radiopharmaceuticals. Since then, computers have gradually become an essential tool in several imaging modalities, for example, x-ray computed tomography (CT), magnetic resonance imaging (MRI), single photon emission computed tomography (SPECT), position emission

tomography (PET), and digital radiography. Medical imaging is one of the principal tools of diagnosis. One of the key uses of computers in medical imaging is the processing of digital images, using image processing tools, to present the information contained in the images in more constructive and precise forms. In this thesis, for the processing of images, several computer graphics and image processing tools for different kind of images, particularly for dual energy x-ray absorptiometry (DXA) images were used. At present, bone mineral density analysis by means of DXA image analysis, measures the average distribution of bone mineral content at a specific area to determine the risk of osteoporosis, and fracture. Even though, until recently, determining the risk depending on the bone mineral contents of DXA image has been a standard way of determining the risk, this sometimes is not able to determine the risk of fracture of bone. Changes to the internal structure of bone may cause the risk of osteoporosis or fracture. Hence it is of interest to study the variation of grey level patterns of pixels of DXA images, assuming the grey level patterns of pixels varies with the variation of trabecular structure of bone, to determine the risk of osteoporosis and related fractures.

1.1.2 Basic Bone Structure

Bone is regarded as living tissue consisting mainly of mineralized (calcified) collagen. Collagen is a protein that provides a soft structure, strength and flexibility to bone in movement. Calcium phosphate is the mineral that adds strength to bones and makes the bone structure solid. In fact, bones are organs consisting of hard living tissue that gives a body structure. Bone is composed of two kinds of tissues; cortical

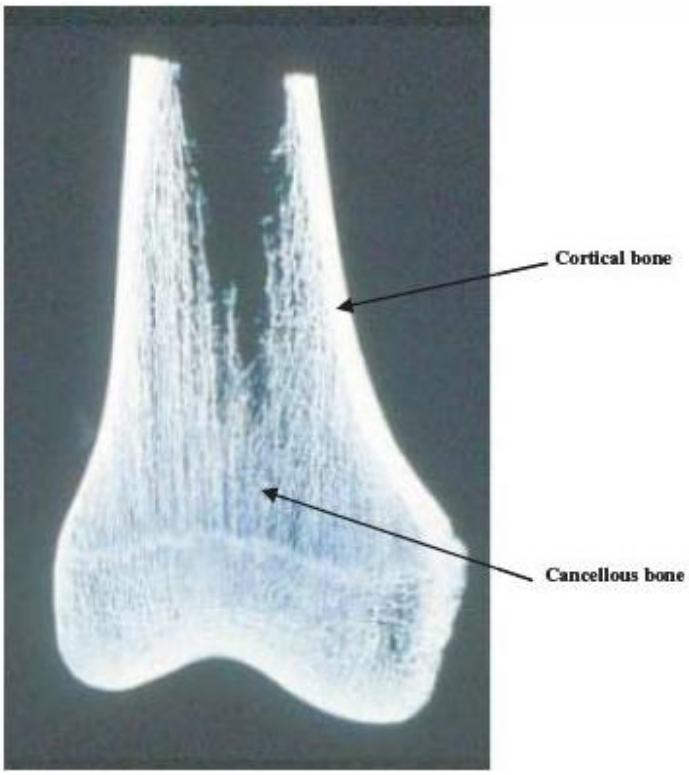

Figure 1.1: Radiological appearance of cortical and cancellous bone. (Image obtained from Nather et al [5].).

(compact) tissue and cancellous (trabecular) tissue [2]. Inside the bone there is bone marrow that is the spongy tissue. The quantity of these two kinds of bone differ depending on strength or weakness and may vary in different bones or in different parts of the same bone. In the radiological appearance of a sample bone in Figure 1.1, the dense cortical bone and the porous trabecular bone is shown.

1.1.3 Compact Bone

Compact bone is dense in texture and is the hard bone material of the outer layer of bone. There are a lot of solid matter in the compact bone, while the hollow

space is small. Bone tissue consists of repeating circular-like units called osteons or Haversian systems. According to Carter [3], a Haversian canal is a channel in compact bone that contains blood vessels and runs longitudinally in the center of Haversian systems of compact tissue. Each osteon consists of layers of hard bone cells with spaces between each layer. According to CliffsNotes [4], blood vessels and osteons are connected to each other as well as to the central canal by fine cellular extensions. Nutrients and wastes are exchanged through these cellular extensions between the bone cells and blood vessels. Nather et al. [5] describe how compact bone consists of a structure of Haversian systems or osteons. Figure 1.2 shows an example of compact bone consisting of osteons where each osteon has a Haversian canal in the center.

1.1.4 Trabecular Bone

The trabecular bone is thin and is the inner layer of mature bone. This bone contains a smaller quantity of solid matter, while the spaces are large. The trabecular bone consists of a series of interlinked plates (trabeculae) of bone which is discussed by Nather et al. [5]. According to CliffsNotes [4], there is no central canal in trabecular bone as it consists of only a few cell layers and each bone cell is able to exchange nutrients with its close blood vessels.

1.1.5 Osteoporosis

Osteoporosis is a disease that causes bones to become more fragile, porous and more likely to break or fracture easily. Osteoporosis usually occurs when people get older, especially, if they do not get enough of certain essential nutrients including

Figure 1.2: Compact bone having Haversian canal in each osteon. (Image obtained from Nather et al [5].).

calcium and vitamin D. That is why bone mineral density (BMD) plays an important role to predict the risk of osteoporosis. According to the information of Bupa [6], human bone is constantly broken down and replaced throughout life, but in early adulthood, mid 20s to mid 30s, the rate is more likely the same and is called the peak bone mass. In later adulthood, after mid 30s onward, the rate of bone breakdown gradually increases which makes the bone more thin and causes osteoporosis. Such diseases slowly deteriorate bone strength because the internal mesh of bone which consists of protein and minerals becomes fragile. The most common areas that become

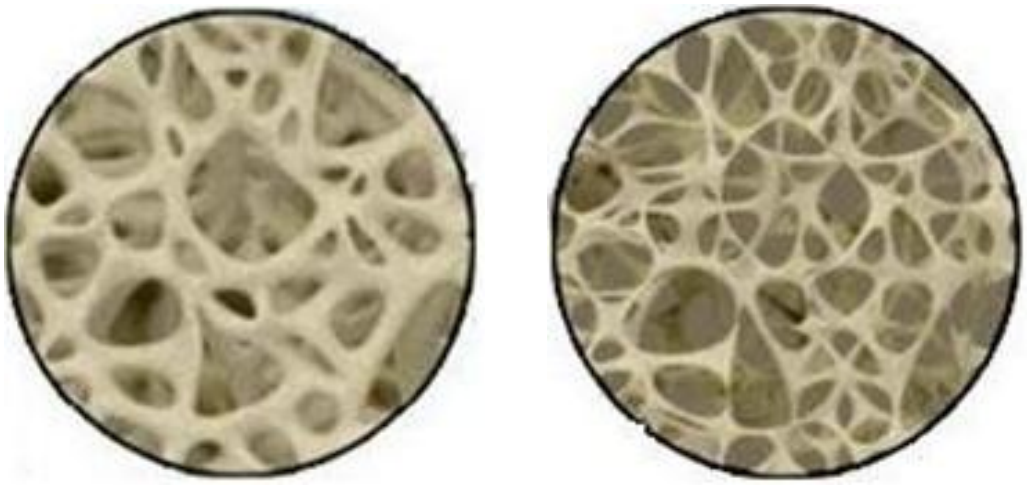

(a)Normal bone (b)Bone with osteoporosis

Figure 1.3: Internal structure of bone with normal bone loss and bone having osteoporosis. (Image obtained from Bupa [6]).

thinner are the hip, spine and wrists which will be at increased risk of fracture. The internal structure of normal and osteoporotic bone is shown in Figure 1.3.

The World Health Organization(WHO) defines osteoporosis as "a disease characterized by low bone mass and micro architectural deterioration of bone tissue, leading to enhanced bone fragility and a consequent increase in fracture risk", mentioned by Karunanithi et al. [7]. The BMD value of a patient with respect to the mean BMD of the normal healthy young adult population is called a T-score. Medical experts predict the risk of osteoporosis from the T-score of a DXA image of a patient, which is the patient's BMD in relation to the mean of the normal young adult population in their peak bone mass years.

1.1.5.1 Causes of Osteoporosis

Osteoporosis is common in an aging population, particularly in females. According to a published study by Cranney et al. [8], fracture rates significantly increase among women of 65 years of age or older. According to Bupa [6], there are several clinical risk factors that may cause osteoporosis, such as low bone density, rapid loss of bone density, internal structure of bone, age, sex, body size, family history, ethnicity, early menopause, diet, medications, alcohol consumption, nutritional deficiency, heavy smoking, a previous fragility fracture, long-term immobility, low levels of vitamin D or dietary calcium, etc. In particular, there are two main characteristics of persons who may become at risk for osteoporosis. The first is a low peak bone density. The second one is a rapid loss of bone density, especially after menopause or later in life. Baylink and Lau [9] hypothesize that if peak bone density is low, only a small amount of additional bone loss causes people to reach a bone density level that is regarded as being at risk for osteoporosis.

Epidemiologic studies indicate that the population is aging, and more people are affected by osteoporosis. For instance, a healthy woman of 50 years of age has almost a 50% risk of having an osteoporotic fracture during the rest of her lifetime and a 15% risk of a hip fracture, with the associated risk of death or loss of independence. An abrupt increasing rate of the occurrence of osteoporosis is noticed worldwide. In Canada, according to Brown et al. [10], about one woman in four and one man out of eight over the age of 50 are expected to develop osteoporosis. Of the people who sustain a hip fracture, more than 20% die within one year despite treatment, and an equal number require long-term care. According to the Osteoporosis Society of

Canada [11], more than 1.4 million people in Canada are suffering from osteoporosis. Moreover, by 2041, about 25% of the population will be over 65 years of age. Hence, within a few decades, the occurrence rate of osteoporosis will increase spectacularly. Women tend to have hip fractures more often than men because they lose bone mass more quickly after menopause.

1.1.6 Dual Energy X-ray Absorptiometry (DXA)

DXA stands for dual energy x-ray absorptiometry. It is a way of measuring bone mineral density (BMD). DXA delivers low dose x-rays of two different energies to a patient's bones to distinguish bone from soft tissue; it provides an accurate measurement of bone density at sites of interest. Absorption of soft tissue is subtracted out to find out the absorption of each beam by bone, which helps to determine the BMD of bone. Spine and hip DXA are regarded as standards for diagnosing osteoporosis as well as to monitor changes in bone density. Thus, DXA is the most widely used bone density measurement technology. DXA is mostly commonly performed to measure BMD from the lumbar spine (L1 to L4 levels) and proximal femur ("hip").

A T-score for BMD values is used to distinguish between normal and osteoporotic bone. It is defined as the number of standard deviations above or below average peak young-adult bone density and provides three different levels of bone mineral density: if a T-score is above -1, bone density is called normal; if a T-score is between -1 and -2.5, bone density is called osteopenic; and if T-score is below -2.5, it is defined as osteoporosis [12] [13].

DXA reports the density of bone as the number of grams per square centimeter of bone (g/cm2). The units of bone mineral density is gram per square centimeter (g/cm2), as the density of bone mineral in the path of the beam is divided by the cross sectional area of the beam [14]. The T-score is the comparison of a patient's bone density with that of a healthy young adult while the Z-score is a comparison with people matched for sex, age and ethnicity. Lower bone mineral density (BMD) is indicated by more negative T-scores and Z-scores [15]. DXA cannot determine the cause of low BMD. Although this can be due to osteoporosis, other medical conditions can also cause low BMD.

In DXA, two different X-ray energies irradiate the region of interest to measure the amount of X-ray absorption (attenuated) by the patient's tissue. The amount of beam absorption (attenuation) is determined by the X-ray's energy, amount (thickness) of tissue, and composition (density) of the tissue. When the amount of bone is higher, the reduction in X-ray beam intensity is greater [16].

DXA is the most widely used technique for bone measurements to determine the risk of fracture and osteoporosis of the patient. The DXA image of a patient helps the doctor to assess the density of patient's bones and predict the risk of osteoporosis. One of the limitations of DXA is its variable bias in terms of body size and sex [17]. Another limitation of DXA is that it does not display the microstructure of the bone. Lastly, the DXA is not always able to detect impaired bone.

1.1.7 Texture Analysis

Texture usually refers to how smooth or rough, soft or hard, coarse or fine etc. a natural scene or real object is. Textures can be classified in two ways; tactile and visual textures. Tactile textures provide an instant tangible feeling of an object; on the other hand, visual texture provides the visual impression of spatial variations of colour, orientation and intensity of that object from the image. Results of texture analysis give an idea of the texture, such as rough or smooth, of bone in each small region (partition). Rough texture is an indication of the deterioration of internal structure. Thus, texture is a significant component for image analysis which helps the segmentation, classification and synthesis problems of images. Image segmentation is a technique that divides the image into small blocks according to the criterion of homogeneity of pixel values. Image classification is a technique to classify each individual pixel based on the spectral information. Spectral information is the information collected from the spectral classes where spectral classes are groups of pixels that are uniform (or near-similar) with respect to their brightness values [18]. Image synthesis is the process of creating new images from some form of image description such as test patterns, image noise and computer graphics [19].

Texture of an image is defined as a function of the variation of spatial distribution of pixel intensities or grey values of a pixel. Figure 1.4 shows an image where the variations of texture is defined by the distribution of bricks in the image. So, from the variations of texture we can extract the orientation of the surface.

Texture analysis is useful in various applications, particularly, for the analysis of medical images. Since bone structural parameters cannot be determined from BMD

Figure 1.4: The orientation of the surface can be determined from the variations of texture of the image. (Image obtained from Mihran [18]).

alone, determination of the microstructure of trabecular bone, in addition to bone mineral density, is needed for early determination of risk of osteoporotic fractures. In this thesis, texture is used as an indicator of the internal structure of bone and methods are examined for texture analysis of bone scan images to discriminate images of diseased bone from the images of normal bone. Texture analysis was performed by analyzing the variation of grey level patterns of pixels of DXA images to discriminate them into normal and osteoporotic groups. The results obtained were compared with the results where the images were discriminated based on the BMD values.

Texture analysis is done by using the existing measures based on co-occurrence matrices [20] as well as fractal dimension [21]. A partitioning technique to analyze grey scale patterns of DXA images is also proposed.

1.1.8 Statistical Methods and Tests Used for Analysis

The statistical methods and tests used for the analysis of the experimented results of both the existing and proposed methods are discussed below.

1.1.8.1 Mean, Standard Deviation and T-test

The mean of a data set is defined as the sum of the data divided by the total number of pieces of data:

$$Mean(\bar{x}) = \frac{Sum\ of\ the\ data}{Number\ of\ pieces\ of\ data}$$

where x represents the value of the data set.

The standard deviation is a statistical measure of variability. The standard deviation, s, of a data set is defined to be the root mean square (RMS) deviation of the values from their mean:

$$Standard\ deviation\ (s) = \sqrt{\frac{\sum(x-\bar{x})^2}{n-1}}$$

where n represents the total number of pieces of data. The variance is the square of the standard deviation (s), represented by s^2.

A t-test is a statistical hypothesis test where the test statistic follows a t-distribution, a probability distribution that occurs in the problem of estimating the mean of a

normally distributed population with a small sample size, if the null hypothesis is true [22]. Independent one-sample t-test is used in testing the null hypothesis that the population mean is equal to a specified value μ. The formula of one-sample t-test (t-value) is,

$$t = \frac{\bar{x} - \mu}{s/\sqrt{n}}$$

where $\bar{x}$ is the mean, s is the standard deviation of the data set and n is the total number of pieces of data.

In the above expression, μ is a specified value which was arrived at by experimentation. A hypothesis test can be performed for μ by employing the test statistics (t-value) and using the t-table to obtain the critical value(s) for the test [22].

In a t-test, two hypotheses are compared; one is a null hypothesis (shortened to H_0), the other is an alternative hypothesis (shortened to H_a). The null hypothesis describes some aspect of the statistical behaviour of a set of data. It is assumed that the null hypothesis is valid unless the actual behaviour of the data contradicts it. Thus, when the null hypothesis proves invalid then the alternative hypothesis proves valid. The alternative hypothesis describes the opposite aspect of the statistical behaviour of a set of data. In other words, the alternative hypothesis is just the negation of the null hypothesis.

The statistical significance level, α, indicates how unlikely a value of $\bar{x}$ will be tolerated before rejecting the null hypothesis. The t-tests were performed with $\alpha = 0.05$ (5%). The degrees of freedom is the number of values in the final calculation of a statistic that are free to vary. For a normally distributed population with mean μ the random variable (t-value) has the t-distribution with $n-1$ degrees of freedom in one-sample t-test and $n+m-2$ degrees of freedom in two-sample t-test, where n and m represents the total number of pieces of data of two groups [22]. The number of degrees of freedom used in the test is 9 in one-sample t-test and 18 in two-sample t-test because there are 10 samples in each category (normal or osteoporotic of hip or spine). There are two types of one-sample t-test; left tailed and right tailed. The critical value for a left-tailed test is denoted as $-t_\alpha$ and for a right-tailed test as t_α. For example, the critical values for df=9, α=0.05, are -1.833 for a left-tailed test and 1.833 for a right-tailed test (Table III, page T-7 of [22]). If the calculated t value of the left tailed t-test is below the critical value chosen for statistical significance, α, then the null hypothesis is rejected while the alternative hypothesis is accepted. Each of these statistics can be used to perform either a one-tailed test or a two-tailed test. For experiment, left-tailed one-sample t-test were performed with df=9 and α=0.05 and two-sample t-test were performed with df=18 and α=0.05=0.05.

The F-ratio test is a statistical technique used to determine if the variances of two independent samples are equal or not. It is a test to determine the homogeneity of variances between two samples. The value of the F-ratio test is given by,

$$F\text{–}ratio = \frac{{S_1}^2}{{S_2}^2}$$

where ${S_1}^2$ and ${S_2}^2$ are the largest and smallest variances respectively of two independent groups of samples [23]. In the F-ratio test, for each sample the degrees of freedom (df) is determined by $(n-1)$, where n is the number of observed samples in each group [23]. If the variances of two groups of samples are equal or close then the F-ratio will not show significant results compare to its critical value stated in the F-ratio distribution table. If the F-ratio test result is not significant, it is assume that the variances are homogeneous otherwise it is assume that the variances of two groups of samples are not homogeneous. Then, apply another standard t-test to determine the difference of means between two samples. The t-test is highly robust to the presence of unequal variances of two independent samples [24].

The two-sample t-test is another commonly used hypothesis test. The method is used to test whether the average difference between two sets of data is really significant or not and determine whether two samples from a normal distribution (in x and y) could have the same mean when the standard deviations are unknown but assumed equal [25]. In this test it can be assumed that mean are equal for both sets of data or not. The null hypothesis (H_0) is: "The population means are the same" and the alternative hypothesis (H_a) is: "The population means are not the same". The equation used to compute the t-value is,

$$t = \frac{\bar{x} - \bar{y}}{s\sqrt{\frac{1}{n} + \frac{1}{m}}}$$

where s is the grand standard deviation, $\bar{x}$ and $\bar{y}$ are the mean and n and m are the total number of pieces of data in the x and y data sets. The degrees of freedom (df) of

the two-sample t-test is, $(n + m - 2)$. The grand standard deviation, s, is calculated by,

$$s = \sqrt{\frac{{s^2}_x + {s^2}_y}{2}}.$$

The MATLAB function ttest2 was used for the hypothesis testing of the difference in means of normal and osteoporotic ROIs. This is a commonly used MATLAB function for the two-sample t-test. The syntax is, [H,P,CI,STATS]=ttest2(x,y,alpha,tail,vartype) [26] [27]. In this function, x, y represents the matrices of the image, alpha represents that the test performs at the (100*alpha)% significance level, tail represents whether the test is one-sample or two-sample t-test and vartype represents whether the test performs under the assumption of equal or unequal population mean. There are two options for vartype: equal and unequal. The result of H is 1 if the null hypothesis is rejected and 0 otherwise. P is the critical value and CI is the confidence interval of the t-test. [STATS] returns the test statistics (t-value), degrees of freedom (df) and grand standard deviation of the data sets. For experiments, the value used for [alpha,tail,vartype] was 5%, "both" and "equal", respectively.

1.2 Problem Statement

Many people experience osteoporosis, fractures and related comorbidities. Resultantly, osteoporosis and fracture burdens are increasing; it becomes an issue of concern. At present Bone Mineral Density (BMD) is used to measure the density of minerals (such as calcium) which represents up to 80% of bone strength. Laurent [28]

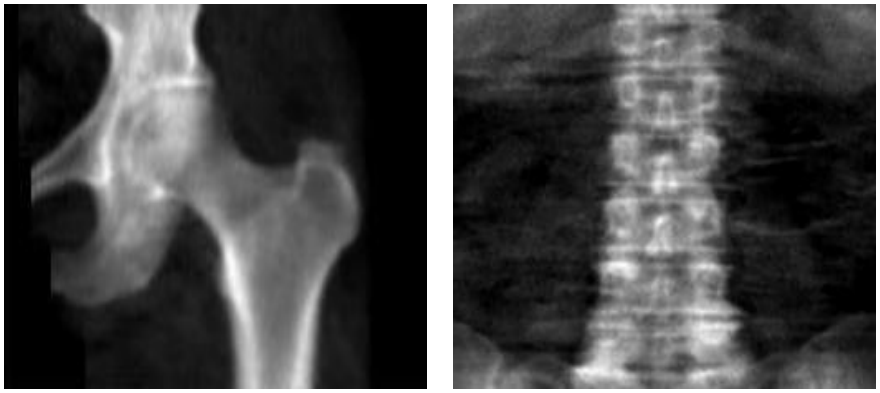

(a)Total hip (b)Lumbar spine

Figure 1.5: Sample DXA scan images of (a) total hip and (b) lumbar spine. (Images courtesy of the Manitoba Bone Density Program [26]).

mentioned that BMD alone is not always sufficient to accurately determine the risk of fracture, even though low BMD and high fracture risk has a strong correlation. Many fractures occur in women with both normal and osteopenic bone mineral densities. If treatment decisions are made only on the basis of BMD values, then many people would not receive treatment at an early stage. Because another important risk factor of osteoporosis is the deteriorated trabecular structure of bone. Therefore, trabecular bone structure should be considered to determine the risk of osteoporosis and, fractures.

At present, bone density is measured by dual-energy X-ray absorptiometry (DXA) scans. By analyzing the data of a DXA image medical experts obtain BMD value and assess whether the patient is at risk of fracture or not. Figure 1.5 shows sample DXA images of total hip and lumbar spine that were obtained from the Manitoba Bone Density database [29]. It is assumed that the grey scale pattern of DXA

image of a deteriorated trabecular structure of bone varies more than the grey scale pattern of DXA image of a healthy bone. Considering this assumption the thesis proposes a method to discriminate grey level images based on significant non-uniform variations of pixels grey level intensity. The obtained discrimination of DXA images will be compared with the known grouping of DXA images where discrimination were performed based on the BMD values.

1.3 Hypothesis

According to Lima et al. [30], alteration in the number of trabecular bone significantly increases the fracture risk in the area composed of trabecular bone. The variations in terms of the rate of bone loss are often greater in the trabecular bone [31]. In the bone scan image such as DXA image and CT image, the porous trabecular bone appears darker than the dense cortical bone. From the radiological appearance of bone in Figure 1.1, the variation of grey scale intensity of pixels with respect to the trabecular and cortical bone is clearly visible.

The hypothesis of the thesis is that the variation of grey scale patterns of DXA images can provide measures which can be use to discriminate the images into groups of normal and abnormal. The assumption is that the trabecular breakdown of bone will appear as larger area of darker pixel in the DXA image. In this thesis, the proposed partitioning method will discriminate the DXA images into normal and osteoporotic group from the variation of the grey scale intensity of pixels. The concept of determining the trabecular breakdown from the variation of grey scale pattern is close to the idea of grey scale pattern used by Fratzl and Paris [32].

1.4 Chapter Outline

The thesis is organized as follows. Literature related to the problem is reviewed in Chapter 2. Texture analysis and experimental results using the contrast measure of co-occurrence matrices and the mean slope value of fractal dimension are discussed in Chapter 3. The statistical analysis of the experimental results are also discussed in Chapter 3. In Chapter 4, the proposed texture measures based on partitioning is described. The validation tests of the partitioning method and the statistical analysis of the experimental results of DXA images using the proposed texture measures are discussed in Chapter 4; it is followed by the concluding Chapter 5, which describes the contribution of the thesis.

Chapter 2

Literature Review

Osteoporosis and fractures are ever-increasing among the aging population. According to the published statistics of Papadimitropoulos et al. [33], over 25,000 hip fractures occur in Canada every year. Hip fracture results in death in up to 20% of cases and disability in up to 50% cases. About 70% of the hip fractures are due to osteoporosis [34].

Much research has been done in the area of osteoporosis as well as determining the risk of osteoporosis and fracture. Existing works focus mainly on BMD values to determine the risk of fracture. As mentioned in Chapter 1, there are many other risk factors that may cause osteoporosis and fractures. Among those risk factors, trabecular bone structure, age and sex are very important. So, all these important risk factors should be taken into consideration, in addition to the BMD value of patients.

Some of the research focuses on clinical interest of bone texture analysis in osteoporosis [35], correlations between grey-level variations in 2 D projection images

(trabecular bone score) and 3D microarchitecture [36], low bone mineral density as a fracture burden [8], process of interpretation of two-dimensional densitometry image for the prediction of bone mechanical strength [37], reproducibility and sources of variability in radiographic texture analysis of densitometric calcaneal images [38], radiographic analysis of osteoporosis [39], contribution of clinical risk factors to bone density-based absolute fracture risk assessment in postmenopausal women [40] and similar areas. The work by Cranney et al. [8], Leslie et al. [40] and Caligiuri et al. [39] in the above list focused on the importance of those risk factors along with BMD values as a determinant of the risk of osteoporosis, fracture, and similar problems. Their results show that bone mineral density alone cannot fully characterize fracture risk, so bone structure as well as age could be an important determinant of fracture risk.

Texture analysis of bone is an important technique for having a better understanding about the roughness or smoothness of the bone. In an attempt to identify significant variation of the texture of an image, the image is partitioned and then texture measures are applied to each partition. This is the idea of the rectangular segmentation presented by Pan and Wong [41].

2.1 Literature Review on Osteoporosis and Fracture Risk

Literature on risk factors of osteoporosis and fractures such as age and trabecular structure are discussed in this section.

2.1.1 Low Bone Mineral Density and Fracture Burden in Postmenopausal Women

Cranney et al. [8] discuss the fracture rates in relation to bone mineral density at different skeletal sites in different age groups (such as age 50-64 years, age $\geq$ 65 years and over) of people. For their research, they did a historical cohort study with a mean observation period of 3.2 years. The study group was constructed from the Manitoba Bone Density Program database. For the study they compared fracture patterns among women 50 to 64 years of age with those among women 65 years of age or older. They evaluated the percentage of osteoporotic fractures and the rates of fracture in postmenopausal women. In their study, they found that most of the postmenopausal women with osteoporotic fractures had nonosteoporotic bone mineral density values.

Outcomes of the experiment, over the period of 3.2 years, shows that a total of 765 (out of 16505 women) women experienced a fracture which correspond to 14.5 per 1000 person-years of overall fracture rate. Among the 765 osteoporotic fractures, 520 fractures occurred in women who were 65 years or older in age. So, the majority of the fractures occurred in postmenopausal women either with normal or

osteopenic bone mineral density. Bone mineral density is one of the important factors in determining fracture risk. Nonetheless, their study suggests and supports the need to consider other important risk factors to better assess fracture risk, particularly for people with minor risk based only on their bone mineral density. They suggested modifying osteoporosis treatment guidelines in order to determine an individual's 10-year probability of fracture that considers other important risk factors (e.g. prior fracture and age) along with bone mineral density [42] [43].

Cranney et al. [8] mention that, according to [44], the World Health Organization is developing algorithms for the calculation of 10-year fracture risk which will incorporate important risk factors in addition to BMD. This system is called FRAX, which has been available since 2008 [45]. Moreover, both the Scientific Advisory Board of Osteoporosis Canada and the Canadian Association of Radiologists recommend clinical risk factors of osteoporosis, such as age, sex, prior fracture history, and medication history, in addition to bone mineral density should be used for the generation of 10-year prediction of fracture and fracture risk.

2.1.2 Contribution of clinical risk factors to bone density-based absolute fracture risk assessment in postmenopausal women

Leslie et al. [40] focused on age, clinical risk factors (CRFs) and bone mineral density (BMD) for their study and show the importance of other clinical risk factors, in addition to BMD, for better assessment of fracture risk. They mentioned that hip fractures are associated with increasing age, specific CRFs and low BMD. For the ex-

perimentation, to compare the importance of CRFs with BMD, they use two models; one is a unidimensional BMD only model, and the other is the full model which incorporates age, CRFs and BMD. The researchers selected 213 postmenopausal women who provided their CRF data and who were also referred for BMD assessment to determine fracture risk. The average age of those women were 65.3 years and age ranges from 50 to 87.9 year. From their results, Leslie et al. found that more women who were considered being at "low risk" of fracture in BMD-only model are found to be at "high risk" in the full model. Hence, the study results show the importance of the role played by all CRFs for the determination of fracture risk. The limitation of the study of Leslie et al. is that their model were not designed for men, premenopausal women, or non-caucasians [46].

2.1.3 Computerized Radiographic Analysis of Osteoporosis

Even though BMD is a good predictor of fracture risk, BMD cannot identify with certainty who will (or will not) have a fracture and only provides a relative assessment of fracture risk. Caligiuri et al. [39] proposed a texture analysis of the trabecular pattern of conventional spine radiographs to determine bone structure, which is a predictor of fracture risk. For the analysis, the researchers used spine radiographs of 43 individuals and compared those with BMD measurements that were obtained from dual-photon absorptiometry, which has much lower spatial resolution than DXA. The study results of Caligiuri et al. show that bone structure analysis, in addition to BMD, may give a more sensitive and specific predictor of risk for osteoporosis and other related fractures. The results are discussed in the paper on pages 2 to 3 by

Caligiuri et al. The results are not reproduced in the thesis to avoid the copyright infringement.

2.2 Literature Review on Image Segmentation

In computer vision, image segmentation is defined as the process of partitioning a digital image into several regions. The aim of image segmentation is to identify the changes in each small region of an image and then use those data for further analysis. Understanding medical images is one of the potential practical applications of image segmentation. There are several techniques developed for image segmentation. Much work has been done using different segmentation techniques for the segmentation of images. The literature reviewed here include segmentation techniques such as quad-tree decomposition, rectangular segmentation, normalized cuts, graph based representation, discrete wavelet frame decomposition, image segmentation based on low-level features for colour and texture, etc.

2.2.1 Efficient Graph-Based Image Segmentation

Felzenszwalb and Huttenlocher [47] proposed an algorithm for the segmentation of an image into regions. They define a predicate, using a graph-based representation, to measure the evidence of a boundary between two regions of the image. The segmentation algorithm of Felzenszwalb and Huttenlocher, based on this predicate, makes greedy decisions but produces segmentation that satisfies global properties. Their algorithm applies image segmentation using two different kinds of local neighbourhoods in constructing the graph.

2.2.2 Image Segmentation Using Colour And Texture Features

Özden and Polat [48] discuss a colour image segmentation method based on features like colour, texture, and spatial information. In their experiment, Özden and Polat used a discrete wavelet frame (DWF) decomposition method, which is a variation of the discrete wavelet transform, to characterize texture of a region of an image. Then the researchers applied colour and spatial feature space analysis of the image, in the mean shift algorithm of Comanicui and Meer [49], and extended the use of these texture features to create an improved segmentation.

2.2.3 Adaptive Perceptual Colour-Texture Image Segmentation

Chen et al. [50] discussed a new approach for image segmentation based on low-level features for colour and texture. The main focus of their proposed method is the segmentation of natural scenes where the statistical characteristics of colour and texture of each segment are not uniform. Chen et al. proposed a method based on two types of low-level features; one describes the local colour composition in terms of their spatially dominant colours and the other describes spatial characteristics of the grey level components of the texture. For segmentation, Chen et al. used the texture characteristics which were obtained from the above-mentioned low-level features of their proposed algorithm.

2.2.4 Normalized Cuts and Image Segmentation

Shi and Malik [51] proposed a segmentation method, namely normalized cut, which is a graph-theoretic criterion for measuring a better partition of an image, in the paper "Normalized Cuts and Image Segmentation". A graph G = (V,E) can be divided into two sets A, B; where A$\bigcup$B=V and A$\bigcap$B=$\emptyset$ and these two parts can be connected by removing the edges. The degree of difference between these two parts is computed as the total weight of the removed edges. This is called the cut in graph theoretic language. Cut is defined as: $cut(A, B)$= $\sum_{u \in A, v \in B} w(u, v)$, where w is the weight on each edge. The optimal partitioning of these two sets minimizes the cut value of a graph. However, to find the minimum cut of a graph, Shi and Malik considered the cut cost as a fraction of the total edge connections to all nodes in the graph. This measure is called the normalized cut (Ncut):

$$Ncut(A, B) = \frac{cut(A, B)}{assoc(A, V)} + \frac{cut(A, B)}{assoc(B, V)}.$$

Here, $assoc(A, V)$= $\sum_{u \in A, t \in V} w(u, t)$ is the total connection from nodes in A to all nodes in the graph and assoc(B,V) is the total connection from nodes in B to all nodes in the graph. Each cut is considered as one segment of an image.

2.2.5 Content-Based Image Retrieval Using Rectangular Segmentation

Pan and Wong [41] used an efficient rectangular segmentation method for content-based image retrieval of colour images. They compute the histogram distance, for

every horizontal and vertical cut, between the mean histogram of two partitions based on the colour histogram matrix of the image. Histogram distances are used to define the similarity or difference of two colour histogram representations. The larger the histogram distance means the more different two partitions are in terms of the distribution of grey level values on that part. They then determine the largest weighted histogram distance as the best cut. Pan and Wong used the best cut i of two partitions of blocks $P_i(h_1, ..., h_k)$ and $Q_i(h_{k+1}, ..., h_k)$, where i is $max(D(mean(P_i), mean(Q_i)).w_i)$. Here, w_i and D denotes the weight of cut i and the distance between mean of P_i and Q_i, respectively. If the weighted histogram distance of the best cut is above a specified threshold, Pan and Wong proposed to partition the image along the best cut; otherwise, keep them separate like before. For each segmented block/region Pan and Wong followed the same process iteratively to find new regions until no more new segmented regions are created. For all segmented regions, the colour histogram is calculated by averaging the histograms of all blocks in that region. It is assumed that all regions belong to one cluster. The sum of colour histogram distances within each cluster is then calculated. For example, the within-cluster sum of a cluster with regions $C(R_1, ..., R_M)$, is

$$sumd(C) = \sum_{m=1}^{M} D(R_m, cent_c)$$

where $cent_C$ is the mean of the histograms of the cluster C. All regions of cluster C is formed as one object if the within-cluster sum is below a threshold (Pan and Wong used 1.5 as a threshold in their experiment). If $sumd(C)$ does not form an object, then use k-means clustering algorithm (starting with k=2) and determine the

within-cluster sum by

$$tsumd(k) = \sum_{n=1}^{k} sumd(C_n).$$

To make sure that the k-mean clustering converges, increase the value of k until $tsumd(k)$ or $tsumd(k) - tsumd(k-1)$ is below the threshold value 1.5. So, each cluster forms an object once the regions are clustered.

2.3 Literature Review on Quad-Tree Segmentation

Quad-tree segmentation is a segmentation technique used for texture analysis. Images are subdivided into blocks that are more homogeneous than the image itself. Images can be subdivided until the blocks are as small as 1-by-1 pixels.

2.3.1 Quad-Tree Segmentation for Texture-Based Image Query

Smith and Chang [52] used quad-trees for segmentation of images in the paper "Quad-Tree Segmentation for Texture-Based Image Query". In that paper, Smith and Chang reported on using a quad-tree decomposition to extract texture features and spatial blocks as a hierarchy of scales in each image. Depending on the texture content of children blocks, the parent blocks are subdivided iteratively. Texture features are extracted from the wavelet representation of the image. Quad-tree data decomposition continued the texture segmentation by grouping image spatial blocks. Smith and Chang continued the segmentation process by using the homogeneous rectangular blocks of texture within the image to perform indexing in the database.

2.3.2 Quad-Tree Decomposition Texture Analysis in Paper Formation Determination

Lieng [53], used quad-tree segmentation technique for segmentation of the texture pattern as discussed in the paper "Quadtree Decomposition Texture Analysis in Paper Formation Determination". For the determination of paper formation, Lieng evaluated the complete formation of a texture image. Lieng compared the difference between the maximum and the minimum grey level values, as well as the preset threshold values. If the difference of the maximum and minimum grey level values exceeds the threshold, the image is divided into four equal subimages. Then, the new subimages are evaluated separately. The author followed these procedures iteratively until the difference (maximum - minimum) is not exceeded or the subimage size is a 1-by-1 pixel.

Chapter 3

Texture Measures Based on Existing Methods

Texture characterizes the coarseness or smoothness of the surface. Image texture characterizes the variation of an image based on the variation of the grey level values and colour intensity of the image [54]. In other words, texture illustrates the property of the surface of an image. Sometimes texture is defined as the repetition of pattern on the surface of the image. Generally, the texture of an image is a complex visual pattern which includes regions with sub-patterns that characterize the brightness, color, shape, size, etc. [55] of the image.

Texture analysis has been widely used in the field of image processing, graphics and computer vision. Many features of an object can be extracted from texture matrices. Different methods are available for representing various texture patterns of images. Such methods are based on co-occurrence matrices, fractal dimension, run

length, grey level differences and neighbouring grey level dependence statistics [56]. Each method has its own model to analyze the texture of an image. This chapter focuses on the application of existing texture measures based on co-occurrence matrices and fractal dimension of DXA images for predicting the risk of osteoporosis and to distinguish osteoporotic bone from normal bone. All numerical results are listed in the Appendix.

The images were obtained from the Manitoba Bone Density database [29]. Sample images of women between ages 65 and 75 were taken from a single DXA scanner (Prodigy, GE Lunar). The samples of DXA images were obtained as grouped into normal and osteoporotic, according to the BMD value of bone, from the Manitoba Bone Density database.

DXA images of normal total hip are shown in Figure 3.1. Figure 3.2 shows the DXA scan images of osteoporotic total hip. DXA images of normal and osteoporotic lumbar spine are shown in Figures 3.3 and 3.4, respectively.

The images shown in the figures are relabelled to preserve anonymity. The labelling convention of the images is as follows: N for normal bone and O for osteoporotic bone; NS1 to NS10 are images of normal spine bone; OS1 to OS10 are images of osteoporotic spine bone; NH1 to NH10 are images of normal hip bone; and OH1 to OH10 are images of osteoporotic hip bone.

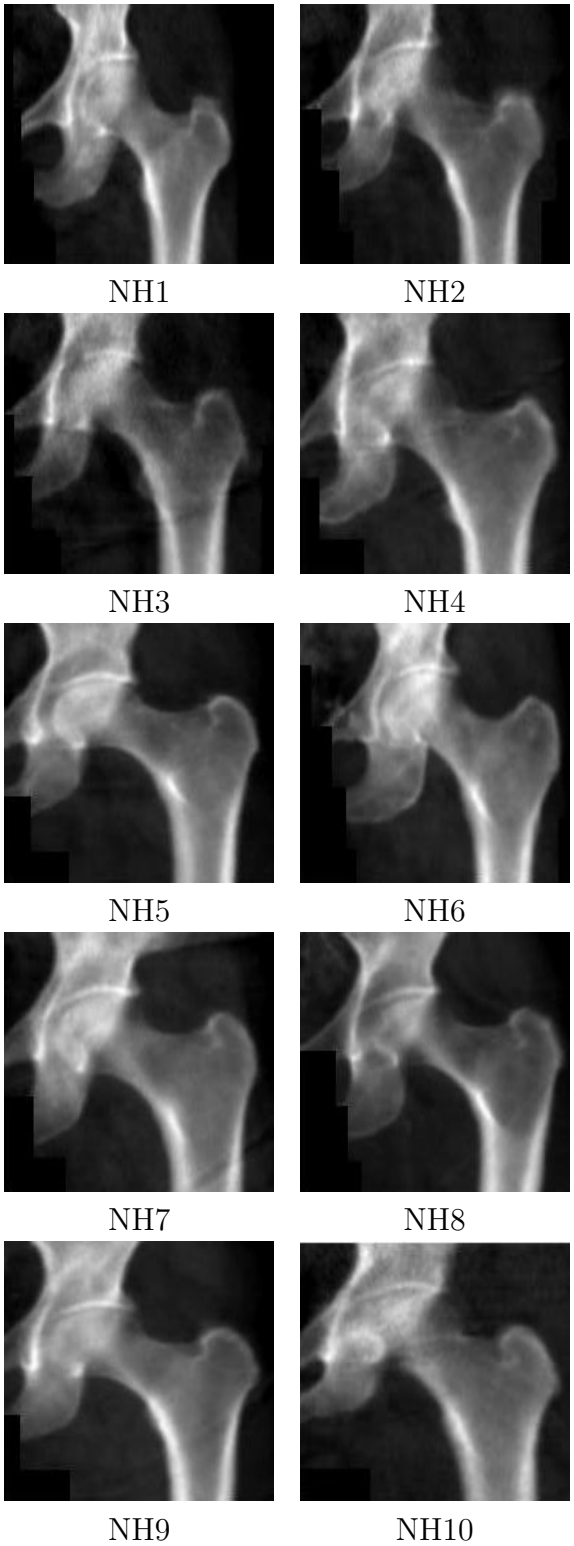

Figure 3.1: DXA images of normal total hip (Images courtesy of the Manitoba Bone Density Program [26]).

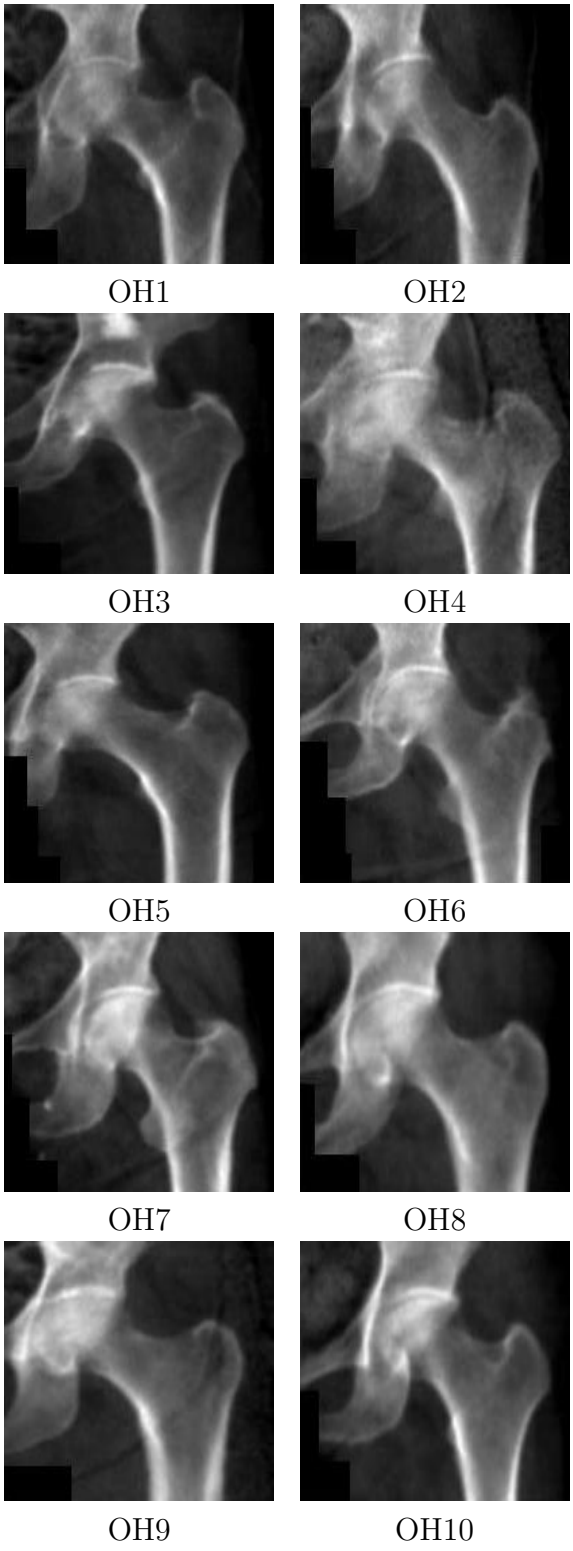

Figure 3.2: DXA images of osteoporotic total hip (Images courtesy of the Manitoba Bone Density Program [26]).

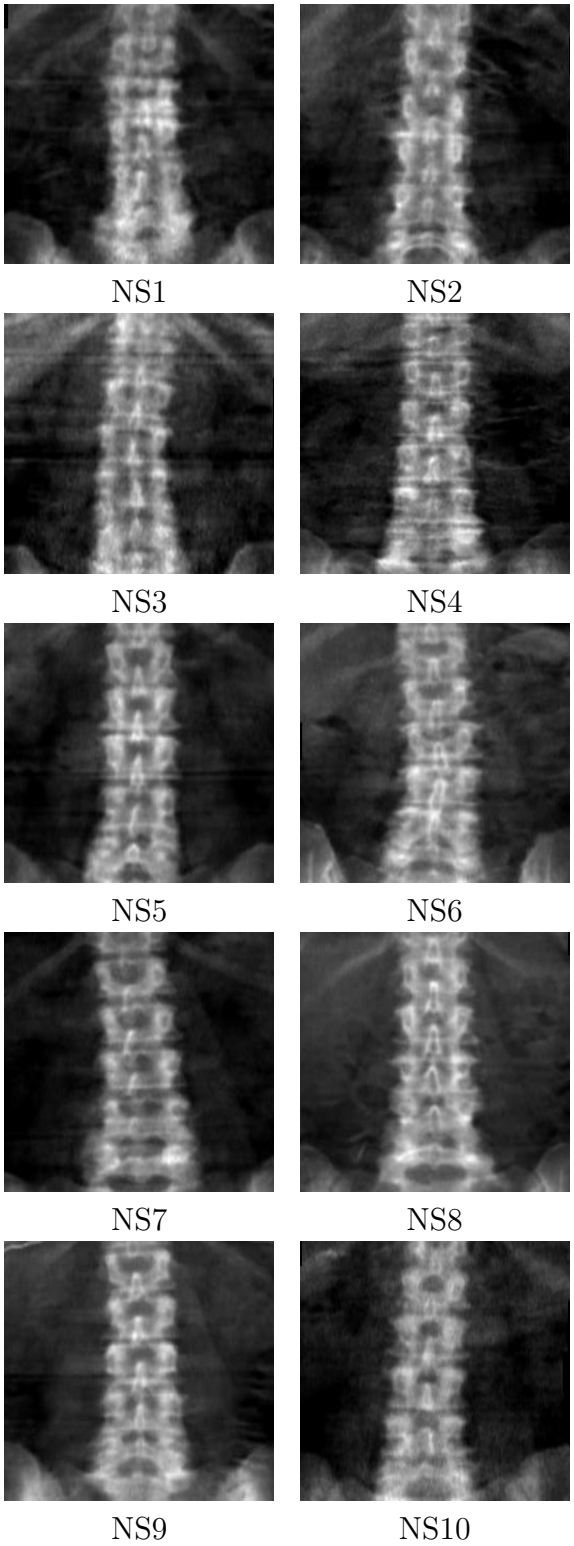

Figure 3.3: DXA images of normal lumbar spine (Images courtesy of the Manitoba Bone Density Program [26]).

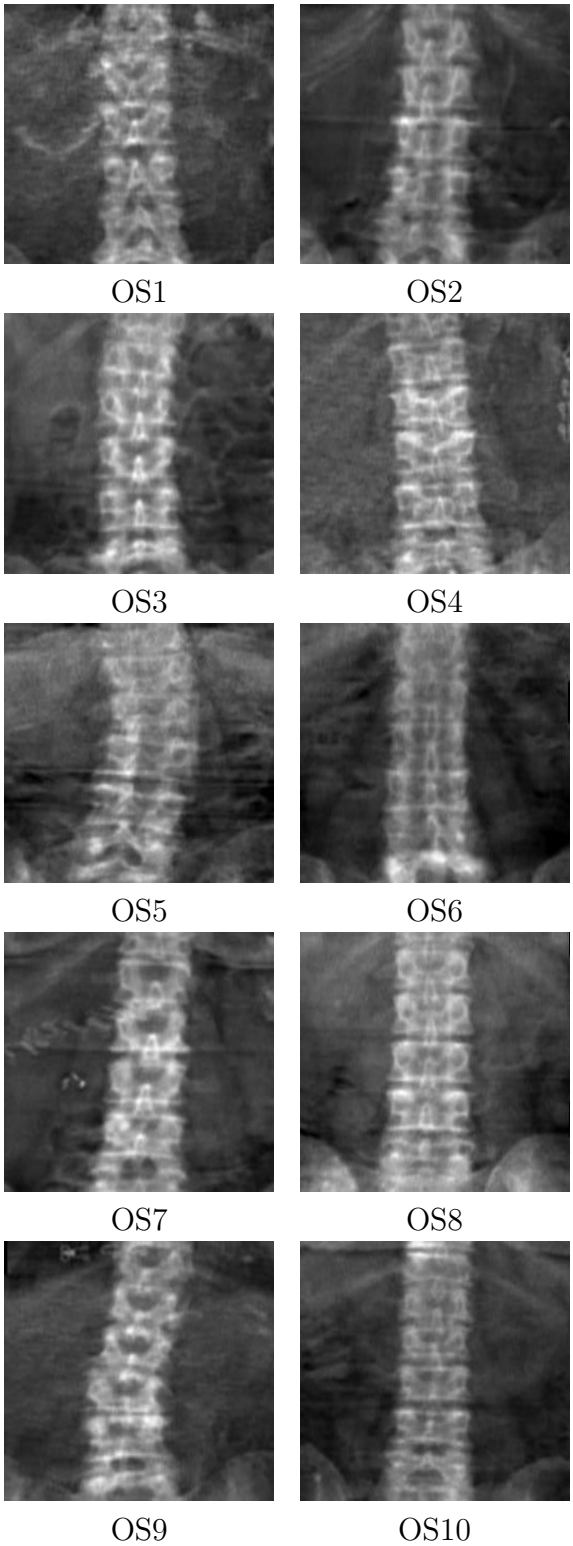

Figure 3.4: DXA images of osteoporotic lumbar spine (Images courtesy of the Manitoba Bone Density Program [26]).

3.1 Region of Interest (ROI)

To avoid the effect of the background of the images on the texture analysis, suitable regions of interest (ROIs) which contain only bone material of that part of hip/spine where most fractures occur were selected from the DXA images. Most hip fractures occur near the upper end of femoral neck to the inter-trochanteric region of hip [57], and most spine fractures occur in the middle to lower part of the spine (L1 to L4 levels) [58]. A single ROI was selected for each hip image, extending along the femoral neck from the base of the femoral neck to the inter-trochanteric region, as shown in Figure 3.5 (a). A single ROI was selected for each spine image, the lower part of the spine, as shown in Figure 3.5 (b). The hip ROIs are same in size for all DXA images of total hip. Similarly, the spine ROIs are same in size for all DXA images of lumbar spine. For experiment purposes, the hip ROIs are interpolated onto a grid as the way they are aligned in the original image will not fit in the method. ROI images were obtained from the DXA images using software called SnagIt. Using SnagIt, the DXA image was rotated through a 60 degree angle and the ROI was then cropped from the DXA image. The changes of the ROI images for this interpolation will be minor and it is assumed that they will not affect the purpose of the experiment as the interpolation was done for both the normal and osteoporotic hip DXA images.

The labelling convention of the ROI images is as follows. F (Femur) for ROI of hip bone images, and S (Spine) for ROI of spine bone images. FN1 to FN10 are the ROIs of normal hip bone images (shown in Figure 3.1) while FO1 to FO10 are ROIs of the osteoporotic hip bone images (shown in Figure 3.2). Likewise, SN1 to SN10

are the ROIs of the normal spine bone images (shown in Figure 3.3) while SO1 to SO10 are the ROIs of the osteoporotic spine bone images (shown in Figure 3.4). The femur ROIs are shown in Figure 3.6 and the spine ROIs are shown in Figure 3.7.

Texture analysis was done by analyzing the variation of the grey level patterns of pixels between the normal and osteoporotic DXA scan ROI images and compared to the discrimination of the groupings of the DXA images in the Manitoba Bone Density database where grouping were done based on the BMD values. In this chapter, two existing texture analysis methods, the experimental results using these methods and the statistical analysis of the experimental results of the sample ROI images of Figures 3.6 and 3.7 will be described.

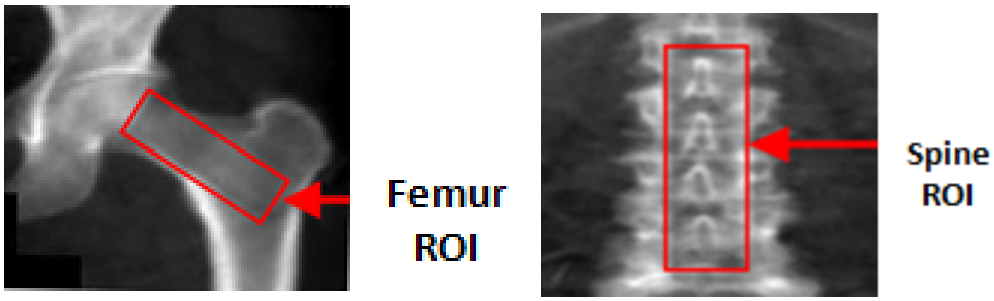

(a)Total hip (b)Lumbar spine

Figure 3.5: DXA scan image of (a) total hip and (b) lumbar spine, with ROI.

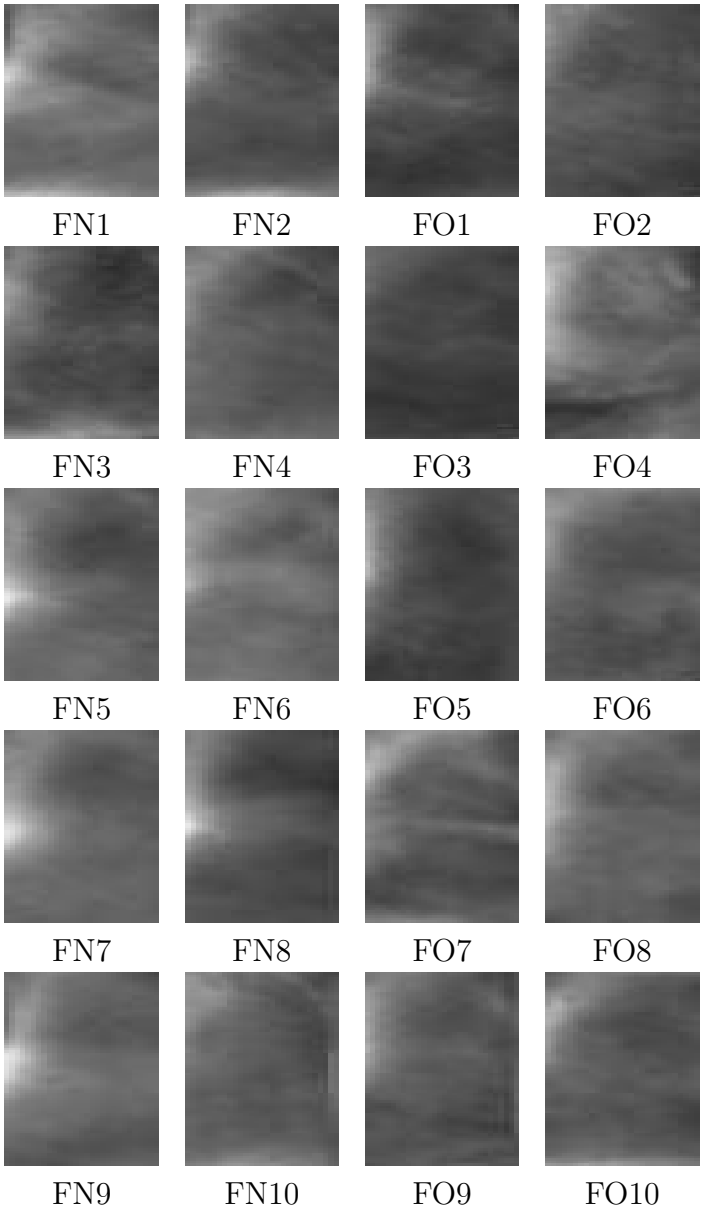

Figure 3.6: Left two columns represents the normal and right two columns represents the osteoporotic hip ROIs of Figures 3.1 and 3.2.

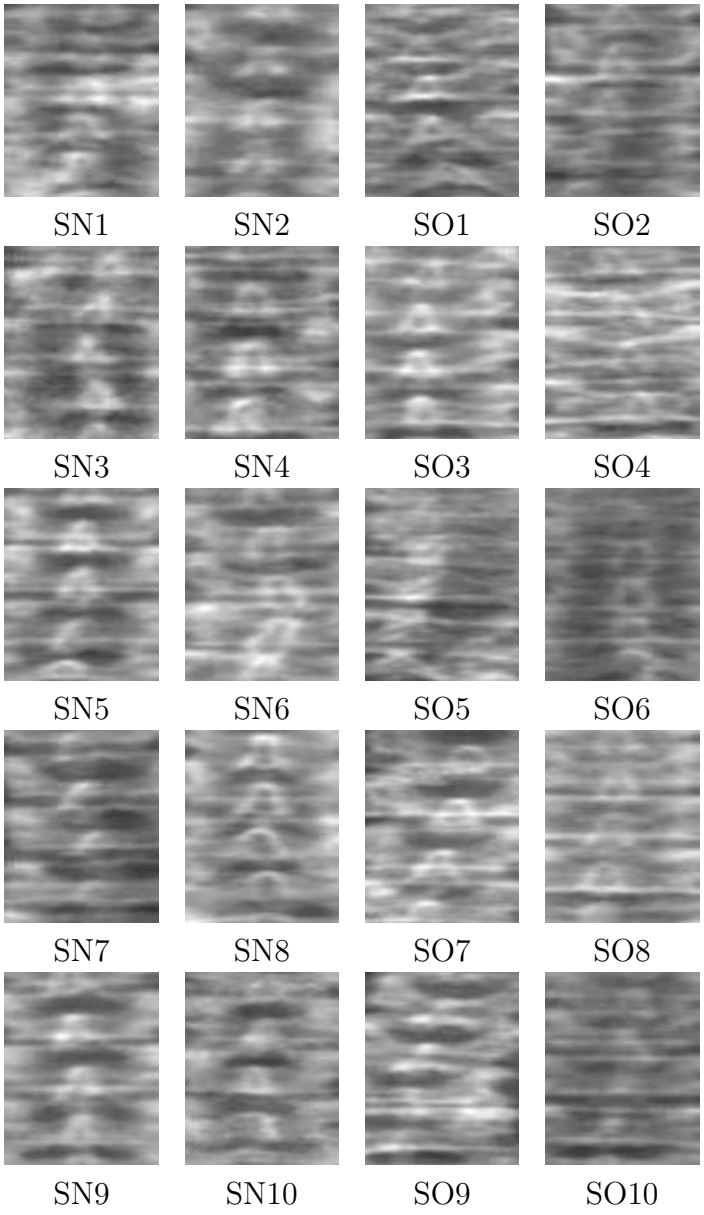

Figure 3.7: Left two columns represents the normal and right two columns represents the osteoporotic spine ROIs of Figures 3.3 and 3.4.

3.2 Co-occurrence Matrices

The grey level co-occurrence matrix is one of the most widely used texture analysis tools for extracting features of an object. This method is based on the repeated occurrence of grey level values (of pixels) in the texture. The co-occurrence matrix of an image with G grey levels is defined as follows [59].

For G grey levels, the G×G co-occurrence matrix $P_{\mathbf{d}}$ for a displacement vector $\mathbf{d} = (dx, dy)$ has entries P_{ij}. The entry P_{ij} of $P_{\mathbf{d}}$ is the number of occurrences of the pair of grey levels i and j of an image, represented as a matrix I, which are separated by a distance $\mathbf{d} = (dx, dy)$ apart. In general the co-occurrence matrix is given as

$$P_{\mathbf{d}}(i,j) =\mid ((r,s),(t,v)) : I(r,s) = i, I(t,v) = j \mid$$

where $(r,s),(t,v)\epsilon$ N×N, $(t,v) = (r+dy, s+dx)$. Or, if u is a matrix of grey levels then the co-occurrence matrix is

$$P_{\mathbf{d}}(i,j) =\mid ((\alpha,\beta),(\lambda,\mu)) : u(\alpha,\beta) = i, u(\lambda,\mu) = j \mid$$

where $(\lambda,\mu) = (\alpha+dy, \beta+dx)$. The (x,y) directions used for the distance, and corresponding (i,j) directions used for matrix entries, are shown in Figure 3.8.

Thus, the entries of the co-occurrence matrices indicates how frequently two pixels with grey levels i and j appear in the image at a given distance $\mathbf{d}$ [56]. For example, consider a 4×4 symmetric matrix of an image consisting of 3 different grey values given as follows.

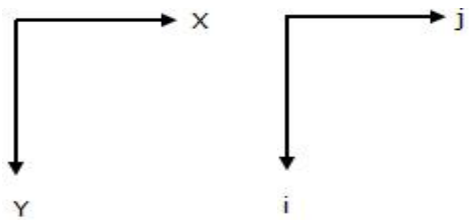

(a) (b)

Figure 3.8: Directions used for (a) the distance (b) the matrix entries

$$\begin{bmatrix} 1 & 1 & 0 & 0 \\ 1 & 1 & 0 & 0 \\ 0 & 0 & 2 & 2 \\ 0 & 0 & 2 & 2 \end{bmatrix}$$

The 3×3 grey level co-occurrence matrix for the above image for distance $\mathbf{d} = (1, 0)$ is given as follows:

$$P_{\mathbf{d}} = \begin{bmatrix} 4 & 0 & 2 \\ 2 & 2 & 0 \\ 0 & 0 & 2 \end{bmatrix}$$

In the above matrix the entry $(0, 0)$ of $P_{\mathbf{d}}$ is 4 because there are four pixel pairs of $(0, 0)$ which are separated by a distance of $(1, 0)$. Similarly, the entry $(0, 1)$ of $P_{\mathbf{d}}$ is 0 because there is no pixel pairs of $(0, 1)$ which are separated by a distance of $(1, 0)$.

For example, consider a 4×4 asymmetric matrix of an image consisting of 4 different grey values given as follows.

$$\begin{bmatrix} 3 & 2 & 3 & 0 \\ 1 & 3 & 3 & 0 \\ 2 & 2 & 1 & 1 \\ 2 & 3 & 3 & 1 \end{bmatrix}$$

The 4×4 grey level co-occurrence matrix for the above image for distance $\mathbf{d} = (1, 0)$ is given as follows:

$$P_{\mathbf{d}} = \begin{bmatrix} 1 & 1 & 0 & 0 \\ 0 & 1 & 1 & 1 \\ 0 & 0 & 1 & 2 \\ 0 & 2 & 1 & 1 \end{bmatrix}$$

In the above matrix the entry $(2, 1)$ of $P_{\mathbf{d}}$ is 0 because there is no pixel pairs of $(2, 1)$ which are separated by a distance of $(1, 0)$. Similarly, the entry $(3, 1)$ of $P_{\mathbf{d}}$ is 2 because there are two pixel pairs of $(3, 1)$ which are separated by a distance of $(1, 0)$.

3.3 Co-occurrence Matrix Based Measure

Co-occurrence matrices are used in many image processing applications such as automatic extraction of features from images. Classification of bone scan images by distinguishing normal bone from abnormal bone may be possible by using properties of the co-occurrence matrices. Depending on the classification task, the extracted

textural properties of the image help to identify abnormalities in the bone image.

A process block diagram of the co-occurrence matrix based measure is given in Figure 3.9. The co-occurrence matrix contains certain properties about the spatial distribution of the grey levels from the texture image. Haralick [60] proposed a number of texture features, such as contrast, homogeneity, correlation, energy and entropy that can be evaluated from the grey level co-occurrence matrices for describing the texture of the image. Among these features, changes of texture in normal and osteoporotic bone may be better visible from the contrast.

Contrast represents the dissimilarity or differences of the texture and homogeneity represents the similarity of the texture. The contrast and homogeneity are defined by the given formulas and these formulas are taken from the article of texture analysis by Tuceryan and Jain [20].

$$Contrast = \sum_{i} \sum_{j} (i-j)^2 P_d(i,j) \tag{3.1}$$

$$Homogeneity = \sum_{i} \sum_{j} \frac{P_d(i,j)}{1+ \mid i-1 \mid}. \tag{3.2}$$

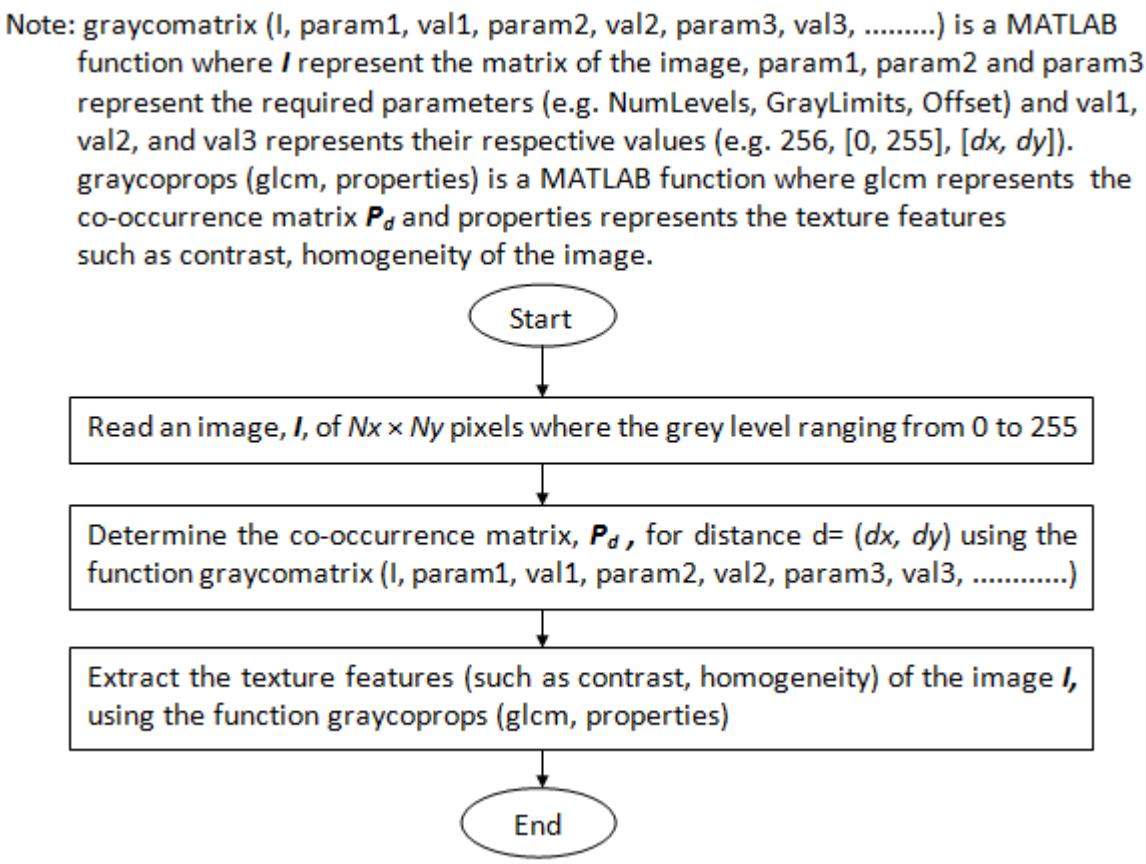

Figure 3.9: The process block diagram of the co-occurrence matrix based measures.

For the texture analysis, the co-occurrence matrices for all ROI images of Figures 3.6 and 3.7 were determined. The MATLAB function graycomatrix(I, param1, val1, param2, val2, param3, val3, ...) [61] was used for determining the co-occurrence matrices of the images. In this function, I represents the matrix of the image. param1, val1, param2, val2, param3, val3, ... represent required parameters and their respective values. E.g., *NumLevels, GrayLimits, Offset* are the required parameters and *256, [0,255], [dx,dy]* may be used as their respective values. Once the co-occurrence matrices are determined, texture features are extracted from the co-occurrence matrices using the MATLAB function graycoprops(glcm, properties) where glcm represents

the co-occurrence matrix and properties represents the texture features of the image such as contrast, homogeneity, correlation, energy and entropy [61]. The contrast and homogeneity are defined by equations (3.1) and (3.2) respectively. The MATLAB function graycoprops(glcm,'contrast','homogeneity') returns the results of contrast and homogeneity of the co-occurrence matrix glcm.

Depending on the adjacency, a 2D square pixel image, for displacement vectors in four different directions can be used. For the experiments, the entries of the co-occurrence matrix were used to evaluate the contrast and homogeneity for the images for different values of **d**. To avoid the intensive computation that involved to determine the co-occurrence matrix, the common values of distances **d** such as 0, 1 and 2 were used by Materka and Strzelecki [62]. Following the literature by Materka and Strzelecki, the distances d = 0, 1, 2, 3 and 4 were considered for the experiment.

For the hip ROI images of Figure 3.6, the results of contrast and homogeneity for **d**=(1,1),**d**=(2,2), **d**=(0,1) and **d**=(0,2) are tabulated in Table A.1. The results of contrast and homogeneity for **d**=(1,0), **d**=(2,0), **d**=(3,3) and **d**=(4,4) are tabulated in Table A.2. For the lumbar spine ROI images of Figure 3.7, the results of contrast and homogeneity for **d**=(1,1),**d**=(2,2), **d**=(0,1) and **d**=(0,2) are tabulated in Table A.3. The results of contrast and homogeneity for **d**=(1,0), **d**=(2,0), **d**=(3,3) and **d**=(4,4) are tabulated in Table A.4. The tabulated results of Tables A.1, A.2, A.3 and A.4 are plotted in Figures 3.10, 3.11, 3.12 and 3.13, respectively, using the 2-sample scatter plots. In Figures 3.10, 3.11, 3.12 and 3.13, the 2-sample scatter plots are subtitled with the distance, d, that is used for the plotted data.

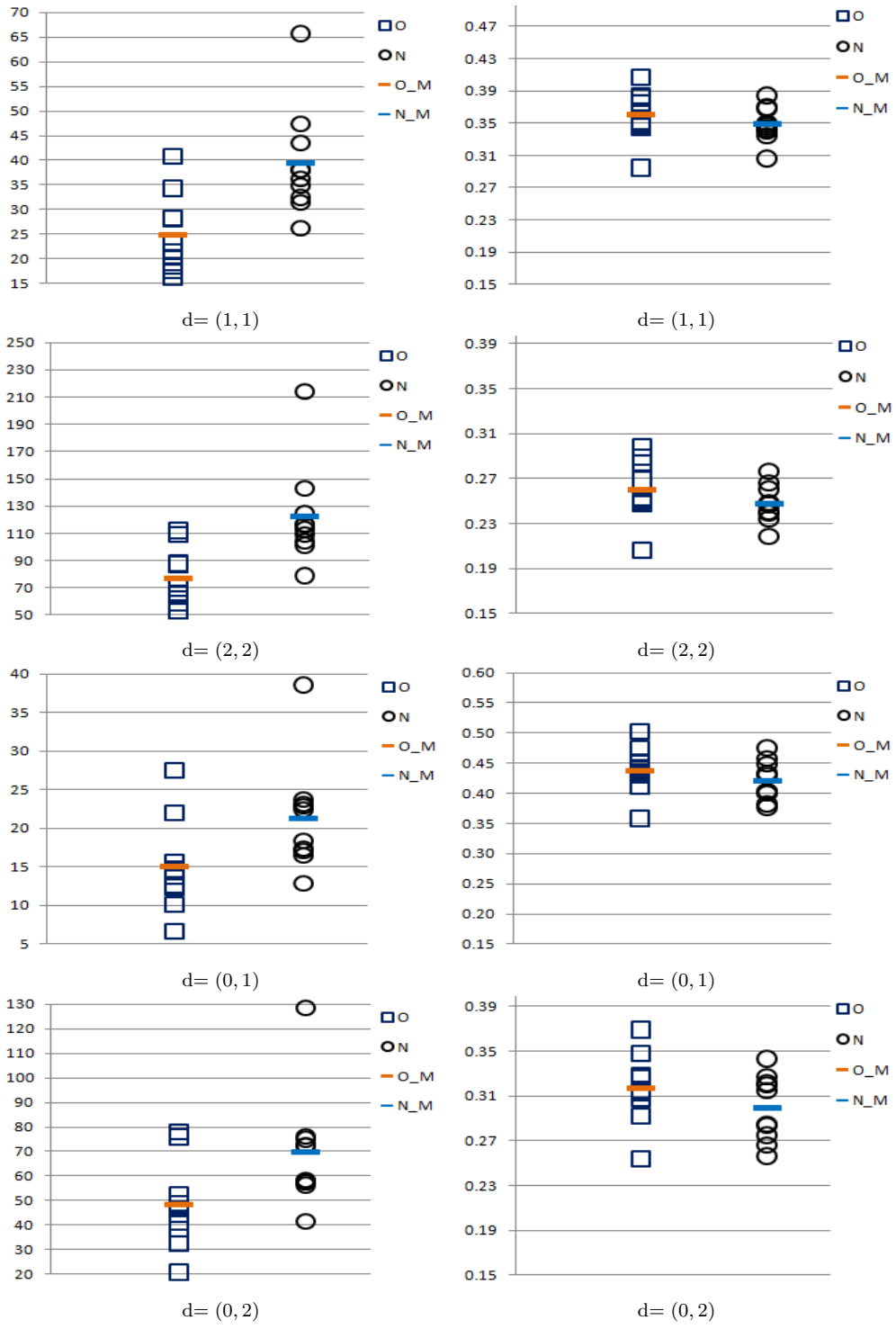

Figure 3.10: Left side plots for contrast and right side plots for homogeneity of the hip ROIs, for the given d values, of Figure 3.6. N, O, N_M and O_M represents the normal, osteoporotic, mean of normal and osteoporotic of hip ROIs, respectively.

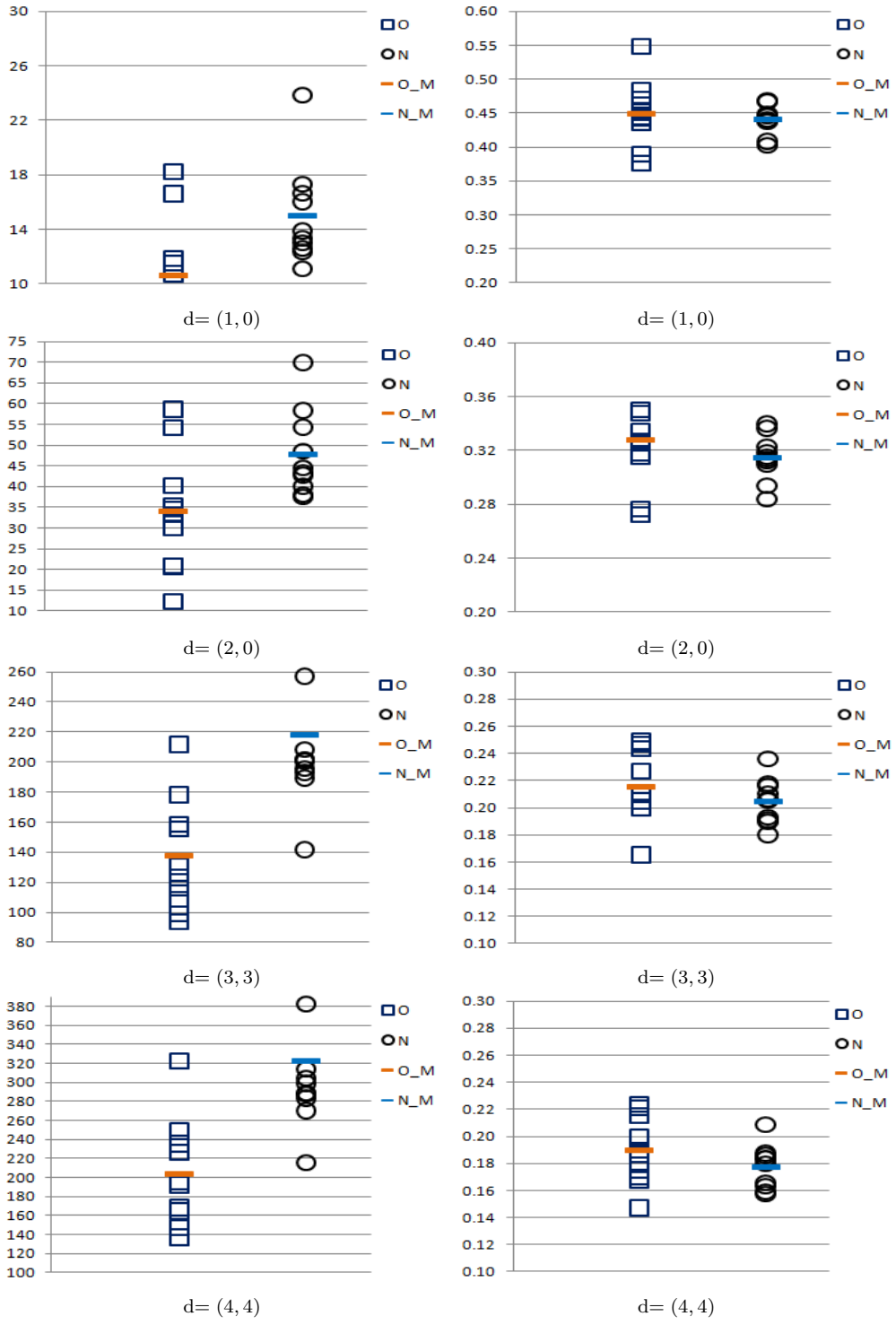

Figure 3.11: Left side plots for contrast and right side plots for homogeneity of the hip ROIs, for the given d values, of Figure 3.6. N, O, N_M and O_M represents the normal, osteoporotic, mean of normal and osteoporotic of hip ROIs, respectively.

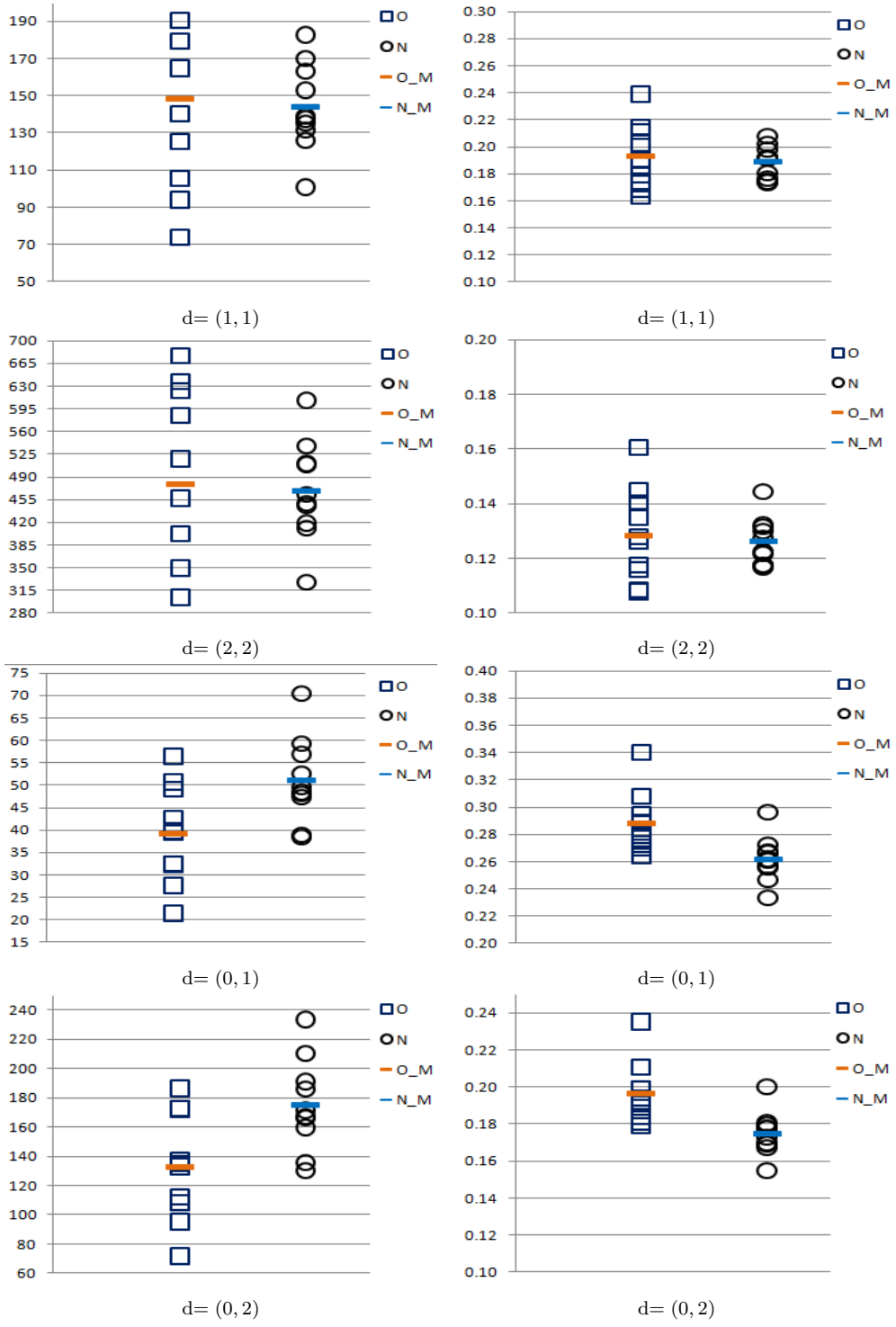

Figure 3.12: Left side plots for contrast and right side plots for homogeneity of spine ROIs, for the given d values, of Figure 3.7. N, O, N_M and O_M represents the normal, osteoporotic, mean of normal and osteoporotic of spine ROIs, respectively.

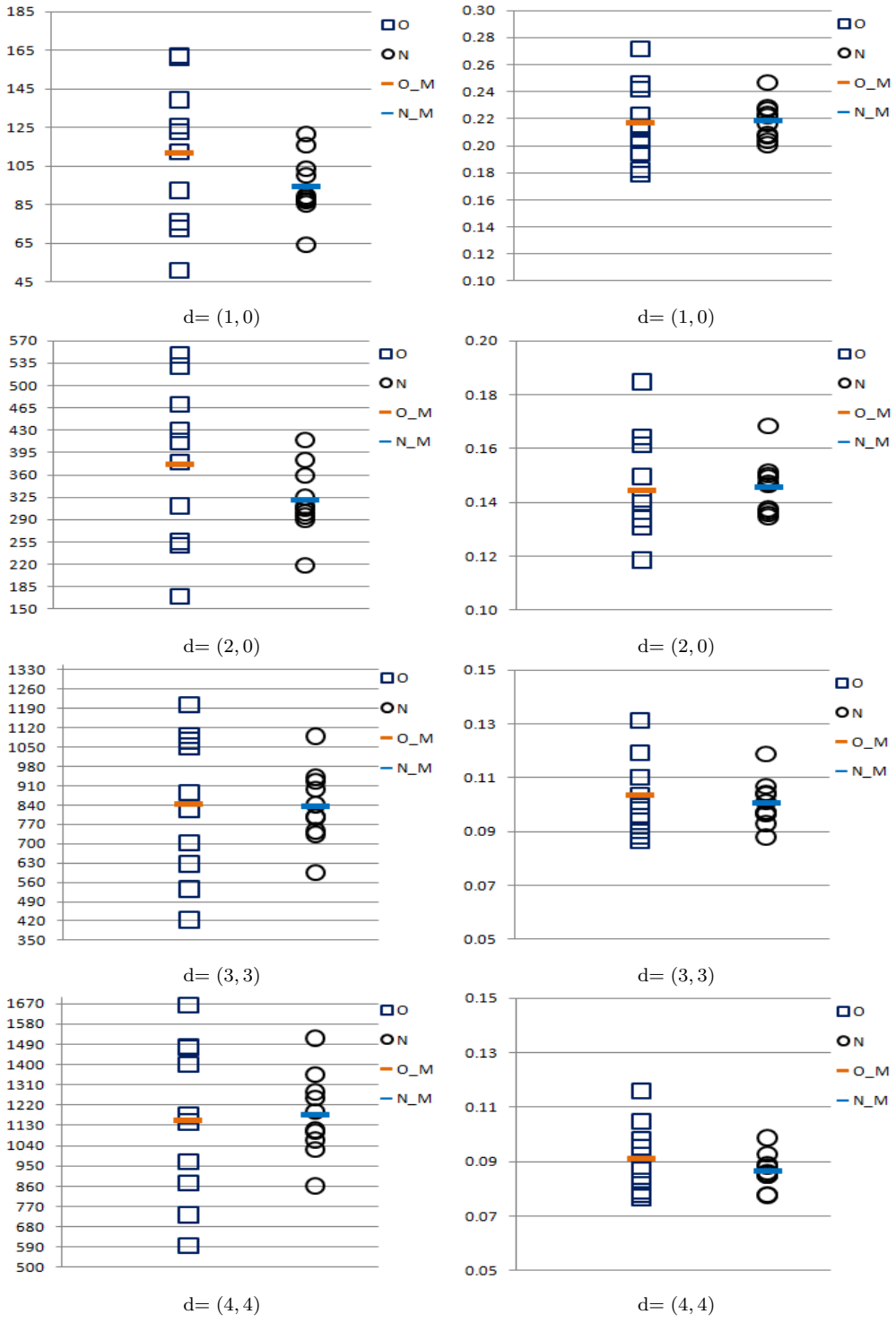

Figure 3.13: Left side plots for contrast and right side plots for homogeneity of spine ROIs, for the given d values, of Figure 3.7. N, O, N_M and O_M represents the normal, osteoporotic, mean of normal and osteoporotic of spine ROIs, respectively.

From the plotted results of Figures 3.10 and 3.11, it is noticed that there is overlap between the range of contrast of normal hip ROIs and that of osteoporotic hip ROIs. Similarly, there is overlap between the range of homogeneity of normal hip ROIs and that of osteoporotic hip ROIs. Hence, it is difficult to determine any pattern to discriminate the normal and osteoporotic hip ROIs from the contrast or homogeneity of hip ROI images. The 2-sample scatter plots of Figures 3.10 and 3.11 present the contrast and homogeneity of the normal and osteoporotic hip ROIs.

From the plotted results of Figures 3.12 and 3.13, it is difficult to determine any pattern to discriminate the normal and osteoporotic spine ROIs because of the large overlap of the range of contrast of normal spine ROIs with that of osteoporotic spine ROIs. Similarly, there is large overlap between the range of homogeneity of normal spine ROIs and that of osteoporotic spine ROIs. Hence, it is difficult to determine any pattern to discriminate the normal and osteoporotic spine ROIs from the contrast or homogeneity of the normal and osteoporotic spine ROIs.

3.4 Fractal Dimension

Fractal dimension is another widely used texture measure. Fractal refers to the self-similarity at different scales of an object pattern from an image. For instance, a given bounded set A is said to be self-similar when A is the union of N distinct copies of itself, where each has been scaled down by a ratio of r.

According to Tuceryan and Jain [20], the fractal dimension D with respect to the number N and ratio r is defined as: $D = (logN)/(log(1/r))$. From the fractal dimension, we can measure the irregularity or roughness/coarseness of the surface of an object. The larger the fractal dimension, the more rough the texture is.

According to Russ [21], the Hurst coefficient is an efficient measure of the fractal dimension of an image. The Hurst procedure gives a plot of the brightness differences of points along a surface as a function of distance between points on a log-log axes. The method can be summarised as follows.

Divide the whole image into 5-, 9-, 7- or 11-pixel wide regions. For each region, determine the pixel class according to the distance from the centre of the neighbouring pixels. Pixels at the same distance from the centre are in the same pixel class. For each pixel class, find the brightest and darkest pixel values and determine the brightness difference of pixels for that class. Compute the log of the brightness difference and the log of the distance of a pixel calss. The brightness difference and the distance are used to construct a Hurst plot. The slope value of a pixel class is determined by using the log of brightness difference and the log of distance for that class. Compute the average slope values of all pixel classes of a region. Then compute the mean of all average slope values of all regions of the image which is the fractal dimension based measure. Plot the mean slope value of the image. Variations of texture of the image will be visible from the mean slope value.

For example, consider the octagonal 7-pixel wide neighbourhood region consisting of 37-pixels shown in Figure 3.14 (a). In this region pixels are labelled according to the distance from the center. Pixels at the same distance fall in the same pixel class.

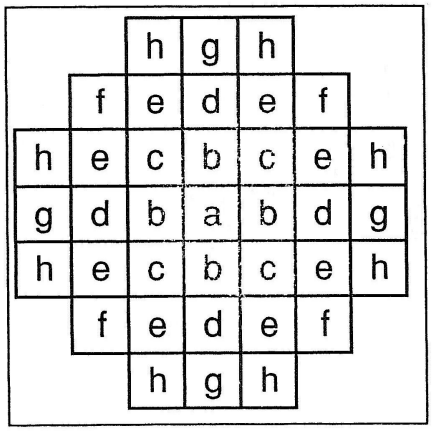

(a)

Pixel class	Number	Distance from center
a	1	0
b	4	1
c	4	1.414 (√2)
d	4	2
e	8	2.236 (√5)
f	4	2.828 (√8)
g	4	3
h	8	3.162 (√10)

(b)

Figure 3.14: (a) Octagonal 7-pixel wide neighbourhood. (b) Distance of pixels of Figure (a) from the center of the neighbourhood [19].

The pixel classes and distances from the centre of the region are shown in Figure 3.14 (b). Two image fragments consisting of pixel values (grey level values) are shown in Figure 3.15. The distances and their brightness data for the neighbourhood are shown in Figure 3.16.

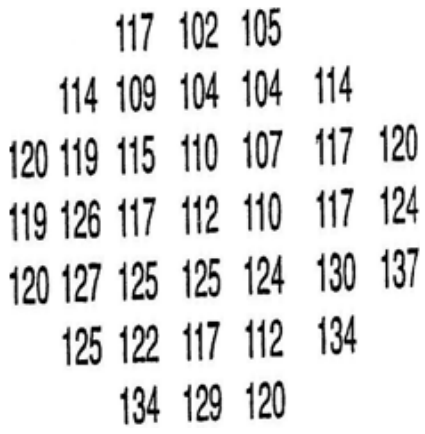

(a)Image fragment a

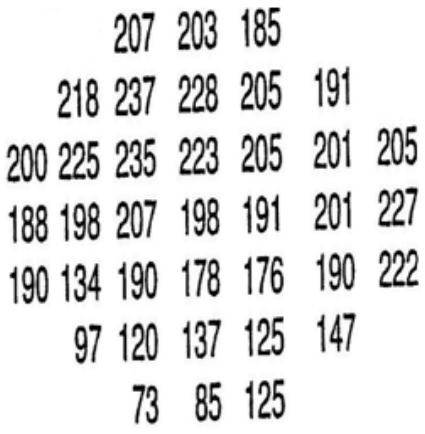

(b)Image fragment b

Figure 3.15: Two fragment of an image [19].

Distance (pixels)							
Image fragment a	1	$\sqrt{2}$	2	$\sqrt{5}$	$\sqrt{8}$	3	$\sqrt{10}$
Brightest	110	107	104	104	104	102	102
Darkest	125	125	126	130	134	134	137
Range	15	18	21	26	30	32	35
Image fragment b							
Brightest	178	176	137	120	97	85	73
Darkest	223	235	235	237	237	237	237
Range	45	59	98	117	140	152	159

Figure 3.16: Distance and brightness data of the neighbourhood pixels of the image fragment of Figure 3.15 [19].

3.5 Fractal Dimension Based Measure

Fractal dimension measures the irregularity or roughness/coarseness of the surface of an object. So, fractal dimension may be used to determine which bone scan images are not normal. The Hurst coefficient method which is described above was used to determine fractal dimensions of all the images in Figure 3.6 and Figure 3.7. The process block diagram of the fractal dimension based measure is shown in Figure 3.17. The procedure is described below.

Divide the whole image into several n×n pixel wide regions where n can be any integer. For the experiment, 16 was used as the value of n. Using the Hurst coefficient method, determine the pixel class for the first octagonal 7-pixel wide region where pixels at the same distance are put in the same class. After the classification of the distance classes, compute the brightness difference of that class and the log of the brightness and that of the distance for each class.

Evaluate the slope value from the log of brightness difference and log of distance of each class. Follow this procedure for the first 16×16 pixels, then compute the average of all slopes of that region. Continue this procedure for all regions in the image. Once the average slope value of each region is determined, calculate the mean of all average slope values of all regions of the image. From the mean of all average slope values, the variations of the texture of the image can be observed.

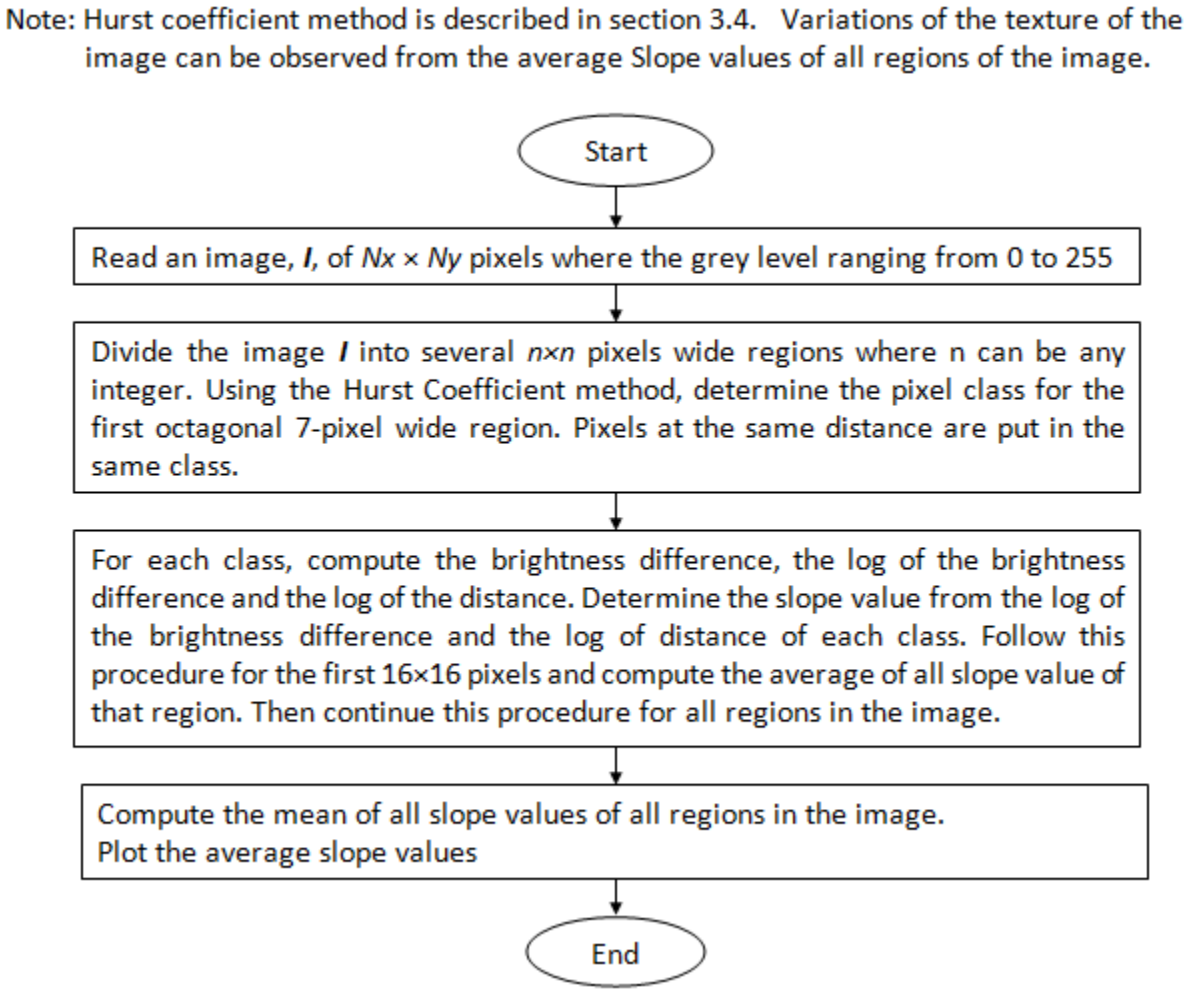

Figure 3.17: The process block diagram of the fractal dimension based measures.

For the ROI images of Figures 3.6 and 3.7, the mean slope values of fractal analysis are tabulated in Table A.5 and the results plotted in Figure 3.18, using the 2-sample scatter plot. From these results, it is noticed that there is overlap between the range of mean slope value of normal hip ROIs and that of osteoporotic hip ROIs. Hence, it is difficult to determine any pattern to discriminate the normal and osteoporotic hip ROIs from the mean slope values of hip ROI images. Similarly, it is difficult

to determine any pattern to discriminate the normal and osteoporotic spine ROIs because of the large overlap of the range of mean slope value of normal spine ROIs with that of osteoporotic spine ROIs. Hence, it is difficult to determine any pattern to discriminate the normal and osteoporotic spine ROIs from the mean slope values of the normal and osteoporotic spine ROIs.

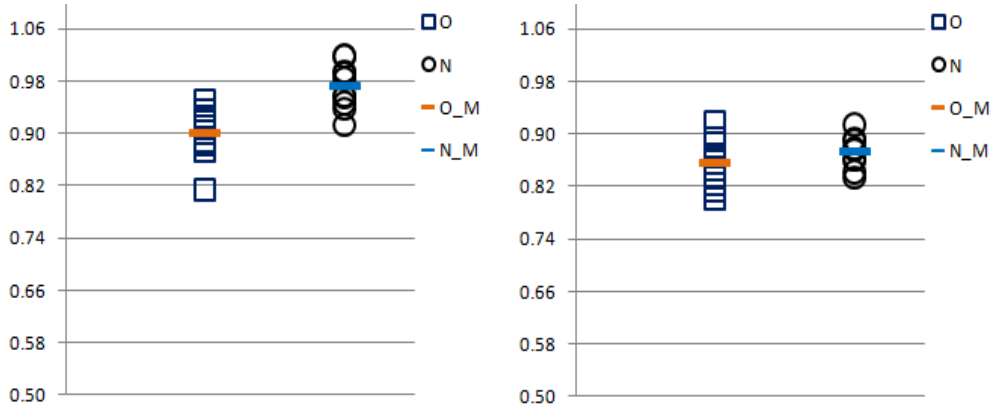

(a)Hip ROIs (b)Spine ROIs

Figure 3.18: Scatter plots of the results of fractal dimension for all ROI images of Figures 3.6 and 3.7. N, O, N_M and O_M represents the normal, osteoporotic, mean of normal and osteoporotic of ROI images, respectively.

3.6 Two Variable Discriminant Tests

Two variable discriminant tests such as 2D plot, linear discriminant analysis, correlation matrix and principal component analysis were done using the experiment results of the existing co-occurrence matrix based method of the ROI images of Figures 3.6 and 3.7. Among these 2D plots are shown to visualize the difference very well between the normal and osteoporotic ROI images. The results of contrast plotted with respect to homogeneity using 2D plots, shown in Figure 4.9.

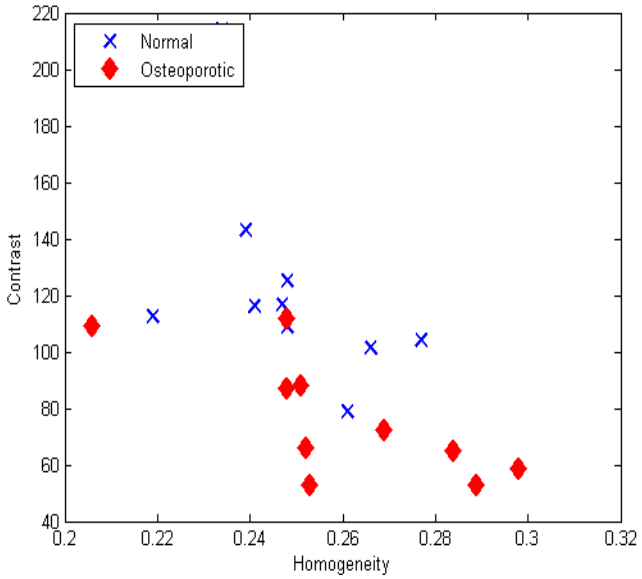

(a)For hip ROIs at $d = (2, 2)$

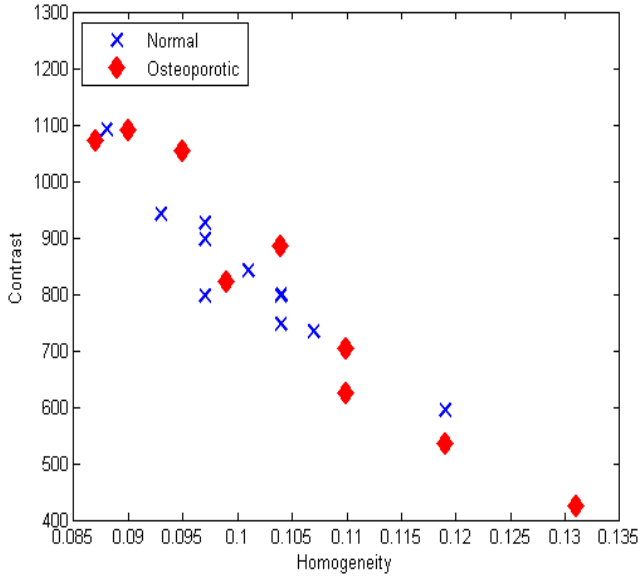

(b)For spine ROIs at $d = (3, 3)$

Figure 3.19: Plotted the results of homogeneity and contrast obtained using the co-occurrence matrix based method for normal and osteoporotic ROIs of Figures 3.6 and 3.7 in (a) and (b), respectively.

3.7 Statistical Analysis of the Experimented Results of ROI Images

Texture analysis on the ROI images using the co-occurrence matrices and fractal dimension method are discussed above. The contrast and homogeneity measures for Figures 3.6 and 3.7 for various values of the distance $d = (d_x, d_y)$ are tabulated in Tables A.1 and A.2, for hip ROIs and Tables A.3 and A.4, for spine ROIs. The tabulated results are plotted in Figures 3.10 and 3.11, for hip ROIs and Figures 3.12, and 3.13, for spine ROIs. The statistical analysis of the experimented results of the ROI images using the existing co-occurrence matrices and fractal dimension method are discussed below.

3.7.1 F-ratio Test

The F-ratio test is another hypothesis testing method to determine the homogeneity of two independent groups of samples. As mentioned earlier, for the two-sample t-test the variances of contrast of the normal and osteoporotic ROIs are assumed to be the same. To test the homogeneity of variances, a F-ratio of contrast is calculated. The t-tests were performed at 5% significance level ($\alpha = 0.05$) and the degrees of freedom (df) both for normal and osteoporotic ROIs is $(n - 1) = 9$, because there are 10 samples of ROIs in each group. By F-ratio distribution table lookup [63], the critical value for df=(9,9), and α=0.05, is 3.1789.

The null and alternative hypotheses are

$$H_0 : The\ variances\ of\ contrast\ of\ normal\ and\ osteoporotic\ ROIs\ are\ equal$$

$$H_a : The\ variances\ of\ contrast\ of\ normal\ and\ osteoporotic\ ROIs\ are\ not\ equal$$

The F-ratio test results of contrast for hip ROIs are tabulated in Table 3.1 for all distance d. From the tabulated results, it is noticed that the calculated t-value, for all distance d, are smaller than the critical value $(-t_\alpha)$ 3.1789. Therefore, comparing the critical value $(-t_\alpha)$ and the F-ratio value it is noticed that the null hypothesis is accepted for the variances of contrast of hip ROIs of Figure 3.6 for all distance d which means the variances of contrast of the normal and osteoporotic hip ROIs are homogeneous.

Similarly, F-ratio test results of contrast for spine ROIs are tabulated in Table 3.2 for all distances d. From the tabulated results, it is noticed that the calculated F-ratio values are smaller than the critical value $(-t_\alpha)$ 3.1789 for distance $d = (0, 1)$ and $(0, 2)$ and larger than the critical value $(-t_\alpha)$ 3.1789 for the distances $d = (1, 1)$, $(2, 2)$, $(1, 0)$, $(2, 0)$, $(3, 3)$ and $(4, 4)$. Therefore, he F-ratio test results for spine ROIs are inconsistent. Comparing the critical value $(-t_\alpha)$ and F-ratio value it is noticed that the null hypothesis is accepted for distance $d = (0, 1)$ and $(0, 2)$ where the variances are homogeneous, and rejected for the distances $d = (1, 1)$, $(2, 2)$, $(1, 0)$, $(2, 0)$, $(3, 3)$ and $(4, 4)$ where the variances are not homogeneous.

Results of Contrast of Hip ROIs								
	d=(1,1)	d=(2,2)	d=(0,1)	d=(0,2)	d=(1,0)	d=(2,0)	d=(3,3)	d=(4,4)
F-ratio	1.92	2.81	1.43	1.75	1.34	1.97	3.06	3.02

Table 3.1: F-ratio test results of contrast for all hip ROIs of Figures 3.6. The critical value $(-t_\alpha)$ for df=(9,9), and α=0.05, is 3.1789.

Results of Contrast of Spine ROIs								
	d=(1,1)	d=(2,2)	d=(0,1)	d=(0,2)	d=(1,0)	d=(2,0)	d=(3,3)	d=(4,4)
F-ratio	3.93	3.86	1.33	1.35	5.20	5.34	3.74	3.68

Table 3.2: F-ratio test results of contrast for all spine ROIs of Figures 3.7. The critical value $(-t_\alpha)$ for df=(9,9), and α=0.05, is 3.1789.

3.7.2 Mean, Standard Deviation and T-test

The measures of mean, standard deviation and t-test for the results of contrast of the co-occurrence matrices for the images of Figures 3.6 and 3.7 are shown in Tables 3.3 and 3.4, respectively. Similarly, the measures of mean, standard deviation and t-test for the results of homogeneity of the co-occurrence matrices for the images of Figures 3.6 and 3.7 are shown in Tables 3.5 and 3.6, respectively. The tabulated results of mean, standard deviation and t-test are represented by $\bar{x}$ (for normal ROI images) and $\bar{y}$ (for osteoporotic ROI images), S_x (for normal ROI images), S_y (for osteoporotic ROI images) and t-value, respectively. Two-sample t-tests of contrast values are determined. In the two-sample t-test, two sample means are compared to discover whether they come from the same population. In other words, the two-sample t-test determine if there is any difference between the mean of the two given population. The t-tests were performed at 5% significance level ($\alpha = 0.05$) and the degrees of freedom is $(n + m - 2) = 18$ because there are 10 samples in each group

of ROIs. By table lookup (Table III, page T-7 of [22]) for the two-sample t-test, the critical value for df=18 and α=0.05, is 2.101.

The null and alternative hypotheses are

$$H_0 : The\ mean\ of\ contrast\ of\ normal\ and\ osteoporotic\ ROIs\ are\ equal$$

$$H_a : The\ mean\ of\ contrast\ of\ normal\ and\ osteoporotic\ ROIs\ are\ not\ equal$$

The two-sample t-test results of contrast for hip ROIs are tabulated in Table 3.3 for all distance d. From the tabulated results, it is noticed that the calculated t-value from the expression mentioned earlier, for all distance d, are greater than the critical value $(-t_\alpha)$ 2.101. Therefore, comparing the critical value $(-t_\alpha)$ and the t-value it is noticed that the null hypothesis is rejected for the hip ROIs of Figure 3.6 for all distance d which shows the group mean of contrast of the normal ROIs are not equal to that of the osteoporotic hip ROIs. Similarly, the two-sample t-test results are tabulated in Table 3.4. From the tabulated results of Table 3.4, it is noticed that the results are not consistent for all distances d.

Results of Contrast of Hip ROIs								
Measurement	d=(1,1)	d=(2,2)	d=(0,1)	d=(0,2)	d=(1,0)	d=(2,0)	d=(3,3)	d=(4,4)
$\bar{x}$	39.41	122.08	21.29	69.58	15.02	47.76	217.83	321.83
$\bar{y}$	24.89	76.47	14.97	48.32	10.64	33.97	137.46	203.77
S_x	11.02	36.39	7.06	23.37	3.71	10.34	66.32	97.37
S_y	7.95	21.70	5.91	17.66	4.29	14.51	37.89	56.06
t-value	3.79	3.92	2.43	2.51	2.61	2.55	3.91	3.92

Table 3.3: Mean, standard deviation and t-test results of contrast for all hip ROIs of Figures 3.6. $\bar{x}$ and $\bar{y}$ represent the mean and S_x, S_y represent the standard deviation of the normal and osteoporotic hip ROIs, respectively. The critical value $(-t_\alpha)$ for df=18, and α=0.05, is 2.101.

Results of Contrast of Spine ROIs								
Measurement	d=(1,1)	d=(2,2)	d=(0,1)	d=(0,2)	d=(1,0)	d=(2,0)	d=(3,3)	d=(4,4)
$\bar{x}$	143.845	468.077	51.011	175.220	94.331	320.562	836.845	1175.160
$\bar{y}$	148.158	478.938	39.206	132.427	111.619	375.693	841.779	1150.562
S_x	23.873	77.624	9.517	31.697	16.622	54.682	136.353	185.232
S_y	47.347	152.489	10.976	36.817	37.896	126.331	263.852	355.166
t-value	0.082	0.132	2.582	2.755	-0.926	-0.859	0.264	0.491

Table 3.4: Mean, standard deviation and t-test results of contrast for all spine ROIs of Figures 3.7. $\bar{x}$ and $\bar{y}$ represent the mean and S_x, S_y represent the standard deviation of the normal and osteoporotic spine ROIs, respectively. The critical value $(-t_\alpha)$ for df=18, and α=0.05, is 2.101.

The two-sample t-test results of homogeneity for hip ROIs are tabulated in Table 3.5 for all distance d. From the tabulated results, it is noticed that the calculated t-value for all distance d, are smaller than the critical value $(-t_\alpha)$ 2.101. Therefore, comparing the critical value $(-t_\alpha)$ and the t-value it is noticed that the null hypothesis is accepted for the hip ROIs of Figure 3.6 for all distance d which shows the group mean of homogeneity of the normal ROIs are equal or close to that of the osteoporotic hip ROIs. Similarly, the two-sample t-test results of homogeneity for the spine ROIs

are tabulated in Table 3.6 for all distance d. From the tabulated results, it is noticed that the calculated t-value for all distance d, are smaller than the critical value $(-t_\alpha)$ 2.101. Therefore, comparing the critical value $(-t_\alpha)$ and the t-value it is noticed that the null hypothesis is accepted for the spine ROIs of Figure 3.6 for all distance d which shows the group mean of homogeneity of the normal ROIs are equal or close to that of the osteoporotic hip ROIs.

Results of Homogeneity of Hip ROIs								
Measurement	d=(1,1)	d=(2,2)	d=(0,1)	d=(0,2)	d=(1,0)	d=(2,0)	d=(3,3)	d=(4,4)
$\bar{x}$	0.349	0.248	0.421	0.299	0.441	0.315	0.205	0.177
$\bar{y}$	0.360	0.260	0.438	0.317	0.450	0.328	0.216	0.190
S_x	0.022	0.017	0.033	0.030	0.022	0.017	0.017	0.016
S_y	0.030	0.027	0.038	0.031	0.048	0.039	0.026	0.025
t-value	-0.919	-1.191	-1.067	-1.281	-0.547	-0.959	-1.131	-1.266

Table 3.5: Mean, standard deviation and t-test results of the homogeneity for all hip ROIs of Figures 3.6. $\bar{x}$ and $\bar{y}$ represent the mean and S_x, S_y represent the standard deviation of the normal and osteoporotic hip ROIs, respectively. The critical value $(-t_\alpha)$ for df=18, and α=0.05, is 2.101.

Results of Homogeneity of Spine ROIs								
Measurement	d=(1,1)	d=(2,2)	d=(0,1)	d=(0,2)	d=(1,0)	d=(2,0)	d=(3,3)	d=(4,4)
$\bar{x}$	0.189	0.126	0.262	0.175	0.218	0.146	0.101	0.087
$\bar{y}$	0.193	0.128	0.288	0.196	0.217	0.144	0.103	0.091
S_x	0.012	0.009	0.017	0.012	0.014	0.010	0.009	0.006
S_y	0.024	0.017	0.022	0.017	0.029	0.021	0.014	0.013
t-value	-0.482	-0.397	-3.028	-3.296	0.155	0.191	-0.491	-0.953

Table 3.6: Mean, standard deviation and t-test results of the homogeneity for all spine ROIs of Figures 3.7. $\bar{x}$ and $\bar{y}$ represent the mean and S_x, S_y represent the standard deviation of the normal and osteoporotic spine ROIs, respectively. The critical value $(-t_\alpha)$ for df=18, and α=0.05, is 2.101.

After analyzing the two-sample t-test results of the hip ROIs of Table 3.3, it it noticed that the group mean of contrast of normal group of hip ROIs is not equal to

the group mean of contrast of osteoporotic hip ROIs group, for all listed distances. From the two-sample t-test results of the spine ROIs of Table 3.4, it is observed that the group mean of contrast of normal group of spine ROIs are close to that of the osteoporotic spine ROIs group, for all listed distances. Also, from the two-sample t-test results of the hip and spine ROIs of Tables 3.5 and 3.6, it is noticed that the homogeneity results of normal group of ROIs are very close to that of the osteoporotic group of ROIs.

Texture measures using fractal dimension are tabulated in Table A.5 and the plotted results are shown in Figure 3.18, for all the ROI images of Figures 3.6 and 3.7.

The measures of mean, standard deviation and two-sample t-test for the results of mean slope values that obtained using the fractal dimension based method are listed in Table 3.7 for hip and spine ROIs of Figures 3.6 and 3.7. The t-tests were performed at 5% significance level ($\alpha = 0.05$) and the degrees of freedom is $(n + m - 2) = 18$ because there are 10 samples in each group of ROIs. By table lookup (Table III, page T-7 of [22]), the critical values for df=18 and α=0.05, is 2.101.

The null and alternative hypotheses are

$$H_0 : The\ mean\ of\ slope\ values\ of\ normal\ and\ osteoporotic\ ROIs\ are\ equal$$

$$H_a : The\ mean\ of\ slope\ values\ of\ normal\ and\ osteoporotic\ ROIs\ are\ not\ equal$$

The two-sample t-test results of mean slope values that were obtained using the fractal dimension based measure for the hip and spine ROIs are tabulated in Table 3.7. From the tabulated results, it is noticed that the calculated t-value for hip ROIs, are greater than the critical value $(-t_\alpha)$ 2.101. Therefore, comparing the critical value $(-t_\alpha)$ and the t-value it is noticed that the null hypothesis is rejected for the hip ROIs of Figure 3.6 which shows the group mean of slope values of normal are not equal to that of the osteoporotic hip ROIs. Similarly, for spine ROIs, comparing the critical value $(-t_\alpha)$ and the t-value it is noticed that the null hypothesis is accepted, as the t-value is smaller than the critical value $(-t_\alpha)$ 2.101, which shows the group mean of slope values of normal are equal or close to that of the osteoporotic spine ROIs.

Fractal Dimension Method		
Measurement	Hip ROIs	Spine ROIs
$\bar{x}$	0.97	0.87
$\bar{y}$	0.90	0.86
S_x	0.04	0.02
S_y	0.04	0.04
t-value	4.26	1.09

Table 3.7: Mean, standard deviation and t-test results that obtained using the results of fractal dimension for all normal and osteoporotic ROIs of Figures 3.6 and 3.7. $\bar{x}$ and $\bar{y}$ represent the mean and S_x, S_y represent the standard deviation of the normal and osteoporotic ROIs, respectively. The critical value $(-t_\alpha)$ for df=18, and α=0.05, is 2.101.

3.8 Summary

After analyzing all tabulated and plotted results obtained from the contrast results of co-occurrence matrices, it is difficult to determine a texture measure for DXA images to discriminate the normal and osteoporotic ROIs. Similarly, it is difficult to discriminate the normal and osteoporotic ROIs from the mean slope values of fractal dimension based measure. Thus, the texture analysis of ROI images using the contrast measures of co-occurrence matrices and the slope values of fractal dimension based measure did not contribute any texture measure for the observed normal and osteoporotic samples (ROIs) and the considered parameters (distance, contrast, homogeneity and slope value), that independently can discriminate the normal and osteoporotic ROIs. More intensive experimentation with various distances, d, on a large number of samples may provide better results of contrast to discriminate normal and osteoporotic ROIs. Therefore, it is also noted that failure to determine the diseased bone of the patient using the results of co-occurrence matrices and fractal dimension does not suggest the failure of those methods. An alternative method for analysing the variation of grey-scale patterns of ROIs to discriminate the DXA images into normal and osteoporotic groups is proposed in the next chapter.

Chapter 4

Alternative Texture Measures Based on Partitioning

One of the key uses of computers in medical imaging is the processing of digital images to present the information included in the images in more constructive and precise forms. The usual texture measures using fractal dimension and co-occurrence matrices seem suitable for analyzing texture of objects because they characterize roughness or smoothness. This chapter proposes a new method based on partitioning for texture analysis of DXA images. The proposed texture analysis method based on partitioning looks at different regions to find the variations of grey level patterns of pixels between the normal and osteoporotic ROIs and verify if the discrimination of the DXA images are the same as they were done in the Manitoba Bone Density database according to the BMD values.

This chapter describes the texture measures based on partitioning. The validation of the proposed method is shown using two groups of randomly generated images. Experimental results of the validation test, using the proposed partitioning method, co-occurrence matrix and fractal dimension method, are tabulated. The experimental results are plotted in Figure 4.9 for the DXA scan ROI images of Figures 3.6 and 3.7. All numerical results are listed in the Appendix.

4.1 Segmentation And Texture Analysis of DXA scan Image

In DXA images, the bone does not occupy the whole frame. The quad-tree decomposition or rectangular segmentation is used to segment the image. In computer vision, image segmentation is defined as the process of partitioning a digital image into several regions. The purpose of image segmentation is to split the image into small segments according to the criterion of homogeneity to get a suitable ROI from those segment. There are several techniques developed for image segmentation.

4.1.1 Segmentation Using Quad-Tree Decomposition

Quad-tree decomposition is a segmentation technique that divides a square image into four equal-sized square blocks and then check each individual block to confirm that it meets some criterion of homogeneity. When a block meets that criterion it will not be divided further while it will be subdivided again into four blocks if it does not meet the criterion. This process is continued iteratively until each block meets

the criterion. Quad-tree decomposition of an image puts the image in different blocks of different sizes.

The MATLAB function qtdecomp(I, threshold, mindim) [61] is used for quadtree decomposition. In this function argument I represents the matrix of an image, threshold represent a threshold value, and mindim represent the minimum dimension of the smallest block of the image. The threshold value is used as the criterion to split a block and is specified as a value between 0 and 1.

If the difference between the maximum value and the minimum value of a block's grey level is greater than the threshold then the block is subdivided into four equal-sized blocks. The threshold value is scaled according to the number of grey levels of uint8 (grey level values ranges from 0 to 255) or uint16 (grey level values ranges from 0 to 65,535).

Since, at each iteration, quad-tree decomposition divides images into four equal-sized square blocks, the dimensions of the image should be a power of 2, such as 128-by-128 or 512-by-512, for the the images to be divided until the blocks are as small as a single pixel. For instance, if an image is 192-by-192 then it can be divided into blocks of size 96-by-96, then 48-by-48, 24-by-24, 12-by-12, 6-by-6, and finally 3-by-3. It cannot be further divided.

The images used for the work presented in this thesis are rectangular, not square; they were padded with zeros before being used as an argument in the qtdecomp()

function for the quad-tree decomposition. Figure 4.1 shows a sample of an original DXA image of hip and the results of quad-tree decomposition, using the qtdecomp() function on that image, with a threshold value of 0.30, and mindim values of 8 and 16, respectively. If the matrix of an image (I) is uint8, the threshold value provided is multiplied by 255 to determine the actual threshold to use; if I is uint16, the threshold value supplied is multiplied by 65535. Various values for threshold were used in experiments. Among those threshold values, the value of 0.30 gave blocks which appeared most homogeneous with respect to the intensity of the grey level.

The images of Figure 4.1 show that it is difficult to extract a suitable ROI segment using the quad-tree decomposition technique because the segments obtained using the quad-tree decomposition are square not rectangular. Therefore, quad-tree decomposition is not a suitable segmentation technique to obtain a rectangular ROI segment using this method.

Among those segmentation techniques reviewed in Chapter 2, the rectangular segmentation used by Pun and Wong [41] seems suitable for the segmentation of bone scan images. Other image segmentation techniques reviewed in Chapter 2 may not be as suitable for DXA images because such techniques require the definition of parameters, e.g., low-level features of colour, graph-based representation, etc., for segmentation but the DXA images are grey scale images not colour images. A rectangular segmentation technique is discussed below.

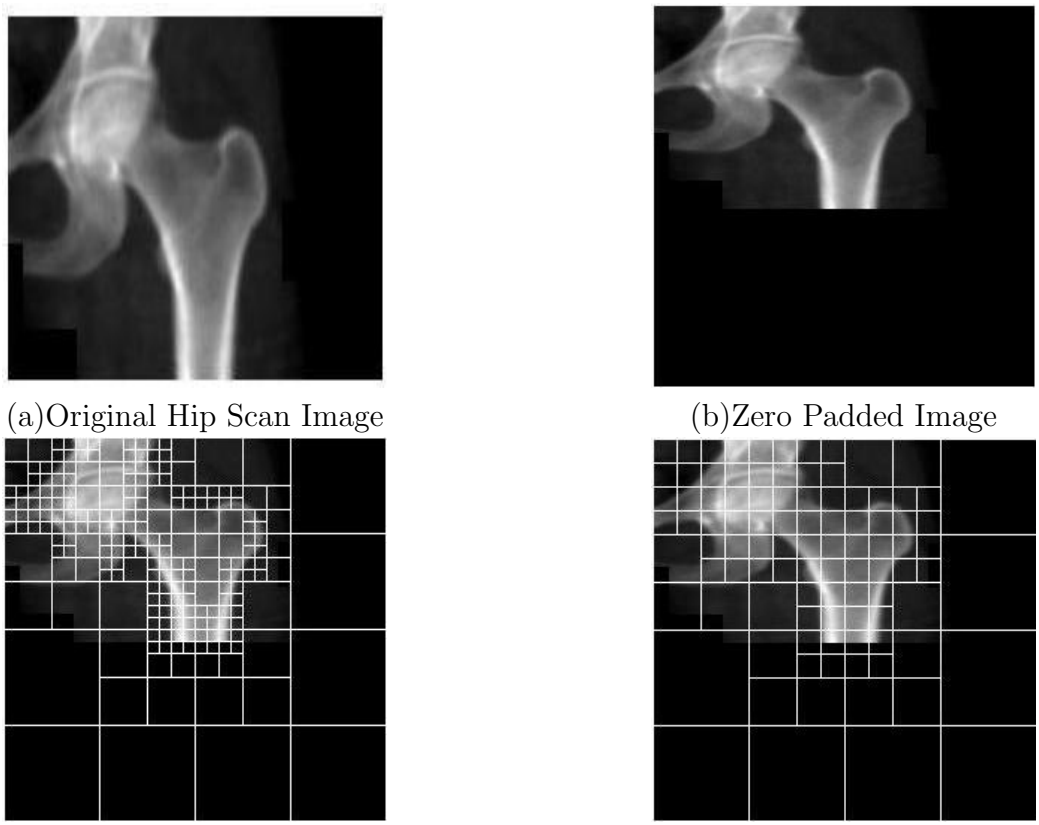

(a)Original Hip Scan Image (b)Zero Padded Image

(c)Quad-tree Decomposition With mindim 8, (d)Quad-tree Decomposition With mindim 16

Figure 4.1: Sample DXA image of hip and the results of quad-tree decomposition on that image. (Images courtesy of the Manitoba Bone Density Program [26]. (c) Quad-tree Decomposition With the DXA image I, threshold 0.30 and mindim 8 (d)With the DXA image I, threshold 0.30 and mindim 16.

4.1.2 A Rectangular Segmentation Technique

A rectangular segmentation technique which is close to the idea of that used by Pun and Wong [41] but not exactly the same, was examined. Pan and Wong's rectangular segmentation is for colour images. That is why Pan and Wong consider the weighted histogram distance of the best cut for partitioning the image. The rectangular segmentation method was adapted for grey scale images where the variation of grey level density is taken into account; it is presumed to indicate the variation of

the bone from being normal.

According to Gonzalez and Woods [64], a grey level is the brightness of pixels in a digitized image expressed in integers, ranging from 0 (black) to 255 (white) for an 8-bit digital signal. Grey level values of pixel play an important role in texture analysis of images. Consider an image of $M \times N$ pixels of grey levels ranging from 0 to 255. The values of M and N of a sample DXA images are typically between 0 to 350. Subdivide the $M \times N$ image horizontally into segments of size $m \times N$ where m is an integer with typical values of 8 or 16. There will be H_x such segments where $H_x = M/m$. Then, again subdivide the $M \times N$ image vertically into segments of size $M \times m$. Likewise, there will be H_y segments where $H_y = N/m$. After the horizontal and vertical subdivision of an image, each segment will be look like a rectangular block of size $m \times m$ and there will be $H_x \times H_y$ number of rectangular blocks or segments. So, the minimum dimension mindim, of the smaller block, in this method is m. At this point, determine the mean grey level value of each block. Then determine the ratio of the mean grey level value of two adjacent horizontal blocks or segments where the

$$ratio = \frac{Mean\ \ Grey\ \ Level\ \ Values\ \ (Bigger\ \ One)}{Mean\ \ Grey\ \ Level\ \ Values\ \ (Smaller\ \ One)}.$$

If the ratio of two adjacent blocks is greater than a threshold value (e.g.,1.2) then these two blocks will be merged because we assume these two blocks are homogeneous in terms of their grey level distributions. From experimentation it appears that a threshold value of 0.12 for the sample DXA images gives better results in determining the homogeneity of a block/segment where the grey level values of that

block are homogeneous. If the ratio of two adjacent horizontal blocks is less than the threshold value then two blocks will remain separate like before. These steps will be followed for all blocks of the image starting horizontally from the top leftmost two blocks and proceed horizontally until the bottom rightmost two blocks. Similarly, determine the ratio of the mean grey level values of two adjacent vertical blocks or segments and follow the same procedure to merge two adjacent blocks if the ratio is greater than the threshold value. Again these steps will be followed for all blocks of the image starting vertically from the top leftmost two blocks and proceed vertically until the bottom rightmost two blocks. So, using this rectangular segmentation technique the segmentation of DXA images is done. Figure 4.2 shows the results of segmentation using the proposed rectangular segmentation with mindim 8 and 16, respectively.

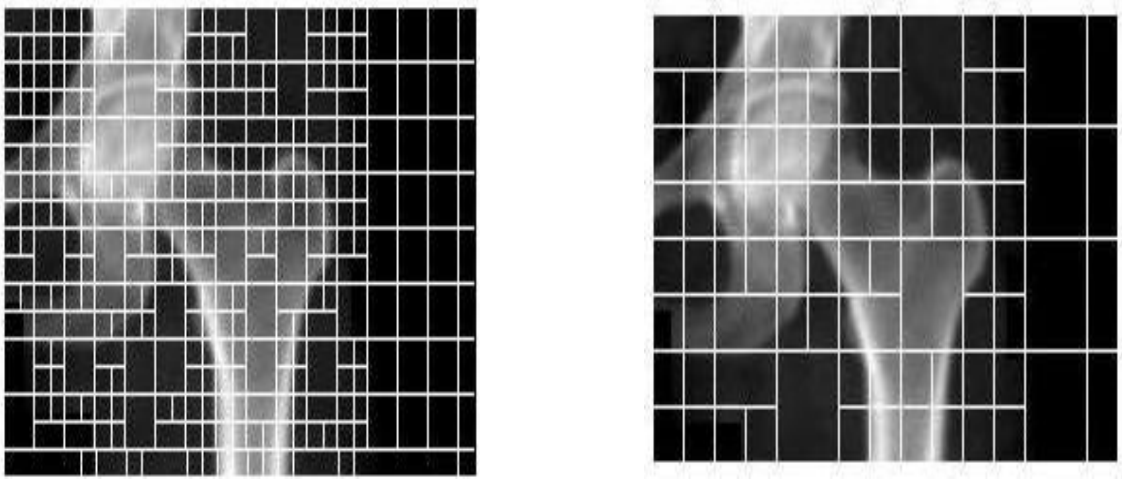

(a) Rectangular segmentation with mindim 8 (b) Rectangular segmentation with mindim 16

Figure 4.2: Results of the proposed rectangular segmentation with mindim 8 and 16 and threshold 1.2. (Images courtesy of the Manitoba Bone Density Program [26].)

The rectangular segmentation results of Figure 4.2 show that it is difficult to obtain a suitable region of interest (ROI) for determining texture measures. Therefore, the rectangular segmentation is not a suitable segmentation technique for the DXA image as it is difficult to obtain a suitable rectangular ROI segment using this method.

4.2 A Proposed Gray Level Variation Measure Based on Partitioning

Osteoporotic or other fractures occur when the internal structure of bone deteriorates. As bone deteriorates, variations in the texture appear, as can be observed in the normal and osteoporotic DXA images of total hip and lumbar spine in Figures 3.1, 3.2, 3.3 and 3.4. As mentioned earlier, it is assumed that the grey level patterns of DXA image of the deteriorated trabecular bone varies from that of bone with healthy trabecular structure. The partitioning method is developed based on this assumption of the variation of grey scale patterns. By partitioning of the ROI bone scan image, it is possible to distinguish the normal ROI images from the osteoporotic ROI images that is at risk of fracture by analyzing the variation of grey level patterns of pixels between the normal and osteoporotic ROIs.

After analyzing the grey level patterns of pixels of the DXA image, it is noticed that the pixel intensity is high for the part of the image that contains the bone material and the pixel intensity is low for the part of the image where the bone material

is not very clearly shown (may be soft tissue). So, the part of the image that contains the bone material has light (high intensity) pixel area and the part of the image where the bone material is not very clearly shown (may be soft tissue) has dark (low intensity) pixel area. In the partitioning method that part of the image which has light pixel area is referred to as "light pixel (lp)". That part of the image which contains dark pixel area is referred to as "dark pixel (dp)". In a ROI image, the ratio of the area containing hard bone material to the area which does not is represented is referred to as the lp/dp (light pixel to dark pixel) ratio.

It is difficult to reach a conclusion by considering the whole DXA image at once as it includes the background, that is why the ROI of the image is used for texture analysis. The proposed method based on partitioning is developed considering the variation of grey level patterns of pixels of DXA images. In the partitioning method, the measures which will be labelled as γ_1, γ_2 and γ_3 will be computed from the variation of grey scale intensity of pixels of DXA image.

4.3 The Proposed Partitioning Method

The idea of partitioning is to check consistency of the variation of the grey level patterns locally by the lp/dp ratio. The way the proposed partitioning method works is described below. The method is summarised in the flowchart given in Figure 4.3.

Consider an image of $N_x \times N_y$ pixels of grey levels ranging from 0 to 255. The values of N_x and N_y for the sample images are between 150 to 300. Subdivide the $N_x \times N_y$ image into rectangular partitions of size $M_x \times M_y$ where $M_x = N_x/m$, $M_y = N_y/m$ and m is an integer with typical values of 10, 12, 16, etc. If N_x and N_y are multiples of m, then there will be m^2 such partitions; if either N_x or N_y is a multiple of m; then there will be $m(m+1)$ partitions; otherwise, there will be $(m+1)^2$ partitions. If there are more than m^2 partitions, then the additional ones will be smaller.

To quantify dark pixel and light pixel in each partition, consider two grey level threshold values b and h. Several experiments with various values of threshold (b and h) were conducted to obtain a specific value for light and dark pixels that will provide good discrimination between the normal and osteoporotic ROIs consistent with the known grouping obtained from the Manitoba Bone Density Database. After analyzing the grey levels of DXA images two grey level threshold values were chosen, one for light pixel and another for dark pixel, to get better variation of pixel intensity between the normal and osteoporotic ROIs. For the experiments, a grey level of 150 was used for b as the threshold value for light pixel and a grey level 100 for h as the threshold value for the dark pixel. If the grey level value of a pixel is $\geq b$, consider

that pixel as light pixel. On the other hand, if the grey value is $\leq h$ consider that as dark pixel for the image.

Consider the whole image as one region and apply these thresholds to evaluate total light pixel to total dark pixel proportion in that image. Determine the total number of pixels considered as light pixel and the total number considered as dark pixel. The ratio of lp/dp for the whole image is

$$\beta = \frac{Total\ Number\ Of\ Light\ Pixels}{Total\ Number\ Of\ Dark\ Pixels}.$$

Let the total number of partitions be M, where M=m^2, $m(m+1)$, or $(m+1)^2$, whichever is applicable. For each partition determine the total number of pixels that have grey level values greater than or equal to b and consider those pixels as "light pixel (lp)". Also determine the total number of pixels that have grey level values less than or equal to h and consider those pixels as "dark pixel (dp)" for that region of the image. Using these numbers compute the lp/dp ratio α_j for that partition where j=(1,2,3,....,M).

Let $\sigma_j = \alpha_j/\beta$ be the scaled lp/dp ratio for each partition which shows the variation of lp/dp ratio for each partition compared to the whole image. If α_j=β then σ_j=1.

To see the data range of σ_j create a list of consistency intervals $[a_0, a_1), [a_1, a_2), \cdots \cdots \cdots, [a_{L-1}, a_L)$ where $a_0 < a_1 \cdots \cdots < a_L$ for some $a_L > 1$. Let

$$c_i = \mid \sigma_j : a_{i-1} \leq \sigma_j < a_i, j = 1, 2, ..., M \mid \tag{4.1}$$

The values used for experimentation were $a_i = 0.25i$, where $i = 0, \cdots \cdots, L = 10$. Hence, $\sigma_j < a_4 = 1$ corresponds to $\frac{\alpha_j}{\beta} < 1$ i.e. $\alpha_j < \beta$. Similarly, $\sigma_j < a_i$ corresponds to $\alpha_j < a_i \beta$. To determine the variation of grey level more clearly, compute

$$\gamma_1 = \frac{\sum_{k=5}^{L} c_k}{\sum_{k=1}^{4} c_k}, \gamma_2 = \frac{\sum_{k=7}^{L} c_k}{\sum_{k=1}^{2} c_k}, \gamma_3 = \frac{\sum_{k=8}^{L} c_k}{c_1}. \tag{4.2}$$

Several experiments with various range of consistency interval c_i, were conducted to obtain a γ_i measure that will provide better discrimination between the normal and osteoporotic ROIs and finally ended up with the γ_3 measure as the γ_3 measure works well for the observed ROIs. The obtained discrimination of ROIs, using the γ_3 measure, are consistent with the known grouping of DXA images that were obtained from the Manitoba Bone Density Database.

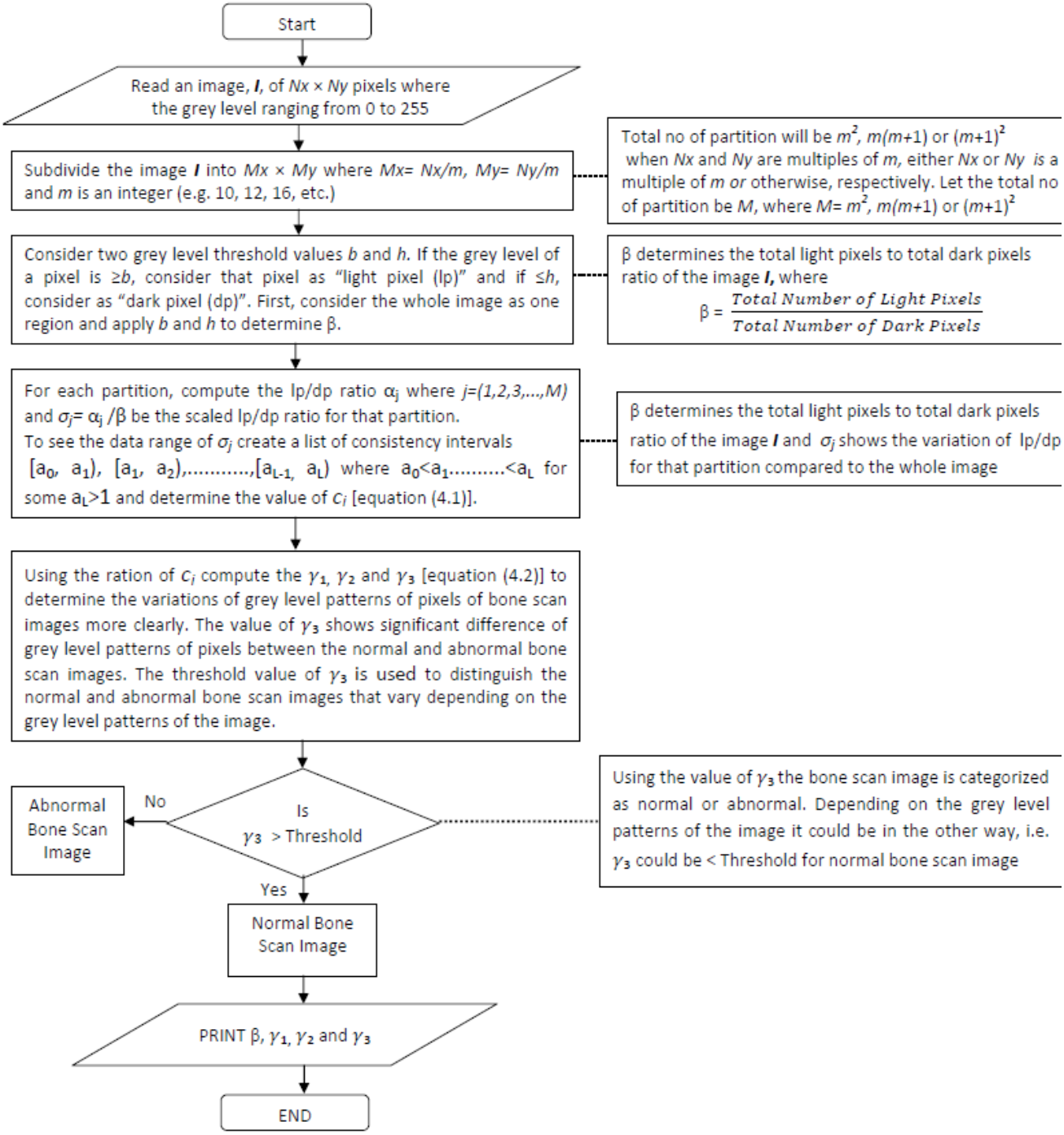

Figure 4.3: The flowchart of the proposed partitioning method.

4.4 Validation of the Proposed Partitioning Method

For the validation of the proposed partitioning method three pairs of sample images were generated using a random number generator. For each pair of images it was attempted to have approximately the same grey level density, but the density for different pairs was varied. The first image of each pair was generated to have a uniform grey level density distribution representing normal bone; the other image of the pair was generated to have a non-uniform grey level distribution representing abnormal bone.

The first image of the pair is prefixed with N, the other is prefixed with A. The MATLAB function `rand(n)` was used as the random number generator where `n` represents the size of the matrix or number of pixels to generate. For the generated images, the size of the matrix used is 256 by 256. The three pairs of sample images are shown in Figure 4.4.

In Figure 4.4, the grey level distribution of the normal images (from top to bottom) are uniform high, medium and low, respectively. On the other hand, the grey level distribution of the abnormal images (from top to bottom) are non-uniform high, medium and low, respectively. Images in Figure 4.4, labelled as N_Sample1, N_Sample2 and N_Sample3 are in normal group representing normal bone and A_Sample1, A_Sample2 and A_Sample3 are in abnormal group representing abnormal bone.

The mean grey level density distribution of the generated sample images was varied from pair to pair but for each pair the mean grey level density distribution is approximately the same for both images. Therefore, the grey level intensity of the images differs from one sample to another though they look very similar. The first

pair of images has lowest mean of grey level density distribution and the last pair of the images has the highest mean of grey level density distribution. The mean grey level density distribution was obtained from the ratio of the highest and lowest grey level density used to generate the sample images.

For the N_Sample1 image, the generated grey level values ranged from 0 to 255. The grey level values were generated randomly such that the ratio of the total number of pixels with intensities from 0 to 149, to the total number of pixels with intensities from 150 to 255, is 2.7. For the A_Sample1 image, 25 light pixel blocks were positioned randomly. The pixel intensities in the blocks were generated randomly with pixels of intensities from 0 to 149 in the dark pixel blocks, and intensities of 150 to 255 in light pixel blocks, such that the ratio of the total number of pixels with intensities from 0 to 149, to the total number of pixels with intensities from 150 to 255, is 2.7. This was repeated for the pair of N_Sample2 and A_Sample2 images. The generated grey level values ranged from 0 to 225, with 0 to 139 for dark pixels and 140 to 225 for light pixels, such that the ratio of the total number of pixels with intensities from 0 to 139, to the total number of pixels with intensities from 140 to 225, is 2.6. The same procedure was followed for the pair of N_Sample3 and A_Sample3 images where the generated grey level values ranged from 0 to 180, with 0 to 99 for dark pixels and 100 to 180 for light pixels such that the ratio of the total number of pixels with intensities from 0 to 99, to the total number of pixels with intensities from 100 to 180, is 3.0.

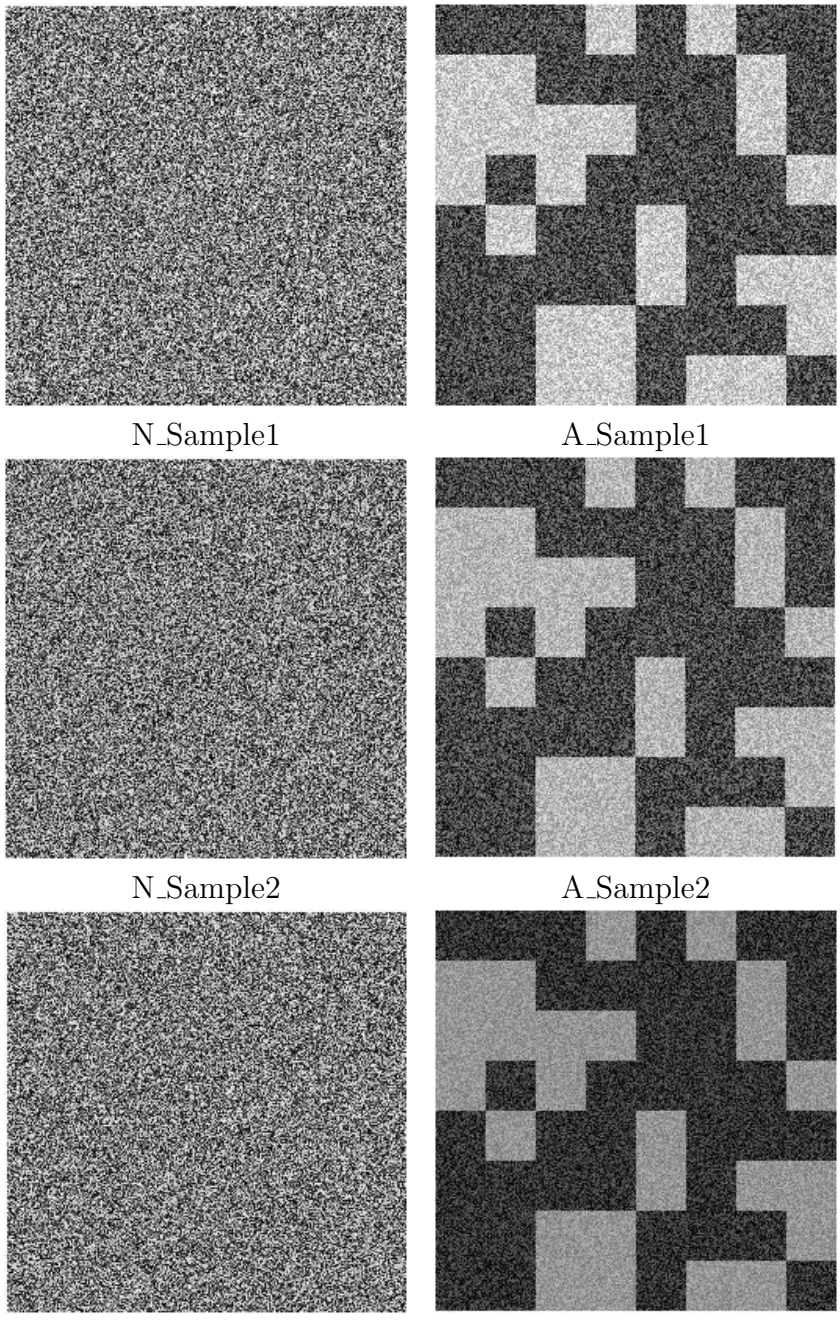

Figure 4.4: Left column represents the normal bone images and right column represents the abnormal bone images.

The proposed partitioning method was applied to the normal and abnormal sample images of Figure 4.4 for the validation of the method. Table 4.1 shows the results of β obtained by using the proposed method. Using the obtained β values determine the γ values for the normal and abnormal sample images. The results of β values obtained for the normal and abnormal sample images of Figure 4.4 correspond to the manner in which the samples were generated. The first sample of each group (normal and abnormal) has the largest β value and the last sample of each group has the smallest β value.

Proposed Partitioning Method	
Samples	**β**
N_Sample1	4.1753
N_Sample2	3.9463
N_Sample3	3.8461
A_Sample1	3.9008
A_Sample2	3.5503
A_Sample3	2.3665

Table 4.1: Results of β obtained using the proposed measures based on partitioning for all sample images in Figure 4.4.

The results of texture measures using the proposed method are tabulated in Tables 4.2, 4.3 and 4.4 for m=10, 12 and 16, respectively. Figure 4.5 shows the plotted results of all images of normal and abnormal group, respectively. After analyzing all these results, it is noticed that all the sample images in the normal group have a larger γ_3 value than those in the abnormal group. All the sample images in the normal group have $\gamma_3 \geq 3$ for m =10, 12 and 16. All sample images in the abnormal group have $\gamma_3 < 3$ for m =10, 12 and 16.

Proposed Partitioning Method			
Samples	***m=10***		
	$\gamma 1$	$\gamma 2$	$\gamma 3$
N_Sample1	1.381	1.238	8.667
N_Sample2	1.381	1.262	5.778
N_Sample3	1.381	1.262	3.467
A_Sample1	1.676	1.906	2.857
A_Sample2	1.703	1.818	2.565
A_Sample3	1.564	1.714	1.839

Table 4.2: Results obtained using the proposed measures based on partitioning where m=10, for all images in Figure 4.4.

Proposed Partitioning Method			
Samples	***m=12***		
	$\gamma 1$	$\gamma 2$	$\gamma 3$
N_Sample1	1.000	1.333	7.200
N_Sample2	1.000	1.309	6.000
N_Sample3	1.000	1.309	4.000
A_Sample1	1.880	2.091	2.263
A_Sample2	1.824	2.022	2.290
A_Sample3	1.571	1.813	2.457

Table 4.3: Results obtained using the proposed measures based on partitioning where m=12, for all images in Figure 4.4.

Proposed Partitioning Method			
Samples	***m=16***		
	$\gamma 1$	$\gamma 2$	$\gamma 3$
N_Sample1	0.969	1.146	5.040
N_Sample2	0.969	1.146	3.316
N_Sample3	0.985	1.146	3.000
A_Sample1	1.753	1.905	2.627
A_Sample2	1.723	1.826	2.500
A_Sample3	1.639	1.703	2.111

Table 4.4: Results obtained using the proposed measures based on partitioning where m=16, for all images in Figure 4.4.

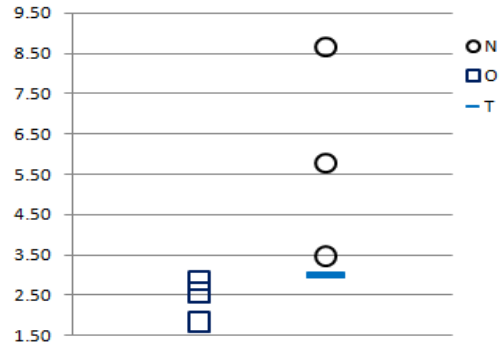

$(a) m = 10$

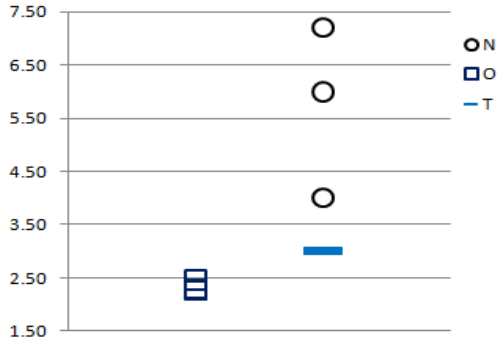

$(b) m = 12$

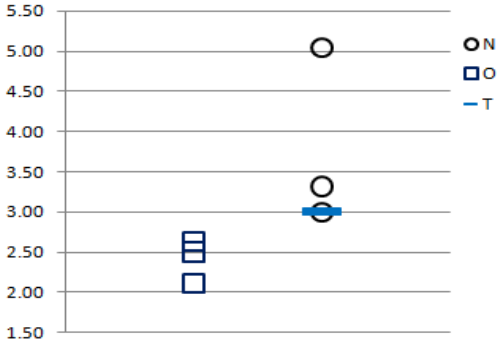

$(c) m = 16$

Figure 4.5: Plots of the results of proposed method based on partitioning for all sample images of Figure 4.4. The Y-axis shows the results of γ_3 and the blue marker indicates the threshold (T) of γ_3.

The results are as expected for the validation data which confirms that method and algorithm behave in a manner consistent with what they were designed for. The proposed partitioning method was applied to bone cross-section images. The results

were presented at a recent IASTED conference [65].

Two existing texture measures, co-occurrence matrices and fractal dimension, discussed in Chapter 3 were also applied to the sample images for comparison. Measures were computed for contrast, homogeneity, energy and entropy features, of the co-occurrence matrices. The measures for entropy and energy did not show significant differences between normal and abnormal sample images.

The contrast and homogeneity of the sample images at **d**=(1,1), **d**=(2,2), **d**=(0,1) and **d**=(0,2) are tabulated in Table 4.5 and at **d**=(1,0), **d**=(2,0), **d**=(3,3) and **d**=(4,4) are tabulated in Table 4.6.

Co-occurrence matrix								
	d=(1,1)		d=(2,2)		d=(0,1)		d=(0,2)	
Samples	Contrast	Homogeneity	Contrast	Homogeneity	Contrast	Homogeneity	Contrast	Homogeneity
N_Sample1	5106.76	0.539	5299.76	0.535	5088.82	0.540	5146.99	0.539
N_Sample2	4813.40	0.541	4933.62	0.536	4796.36	0.541	4837.63	0.540
N_Sample3	4973.32	0.540	5111.76	0.536	4907.36	0.541	4966.33	0.541
A_Sample1	1774.40	0.551	2112.10	0.545	1635.31	0.552	1801.59	0.550
A_Sample2	1496.76	0.553	1818.39	0.547	1385.02	0.554	1522.06	0.553
A_Sample3	956.64	0.561	1283.31	0.555	812.01	0.563	968.25	0.561

Table 4.5: Results of contrast and homogeneity obtained using the co-occurrence matrix based measures for all generated sample images, represents the normal and abnormal group of images, in Figure 4.4 at distance d=(1,1), d=(2,2), d=(0,1) and d=(0,2).

Co-occurrence matrix								
	d=(1,0)		d=(2,0)		d=(3,3)		d=(4,4)	
Samples	Contrast	Homogeneity	Contrast	Homogeneity	Contrast	Homogeneity	Contrast	Homogeneity
N_Sample1	5125.25	0.539	5117.70	0.539	5423.73	0.529	5546.18	0.524
N_Sample2	4789.64	0.541	4773.75	0.540	5088.49	0.530	5239.41	0.525
N_Sample3	4988.40	0.541	4983.60	0.540	5256.29	0.530	5373.13	0.525
A_Sample1	1637.76	0.551	1778.75	0.550	2462.15	0.540	2797.72	0.534
A_Sample2	1381.02	0.554	1499.93	0.553	2139.29	0.541	2443.36	0.535
A_Sample3	819.18	0.562	960.05	0.561	1619.27	0.550	1944.62	0.543

Table 4.6: Results of contrast and homogeneity obtained using the co-occurrence matrix based measures for all generated sample images, represents the normal and abnormal group of images, in Figure 4.4 at distance d=(1,0), d=(2,0), d=(3,3) and d=(4,4).

The tabulated results of Tables 4.5 and 4.6 are plotted in Figures 4.6 and 4.7, respectively. From the plotted results of Figures 4.6 and 4.7, it is noticed that the contrast values of sample images representing the normal group are relatively higher than that of the sample images representing the abnormal group. Similarly, the homogeneity values of sample images representing the normal group are relatively lower than that of the sample images representing the abnormal group. These results are consistent with the results discussed in Chapter 3, obtained using the MATLAB function graycomatrix for the DXA scan ROIs.

The mean slope values of all region of ROI obtained from the fractal dimension based measures, where the slope values were calculated from the log of brightness and the log of distance, are tabulated in Table 4.7. The mean slope values of Table 4.7 show that the sample images of normal group have smaller mean slope values while the samples from the abnormal group have larger mean slope values. The results tabulated in Table 4.7 are plotted in Figure 4.8.

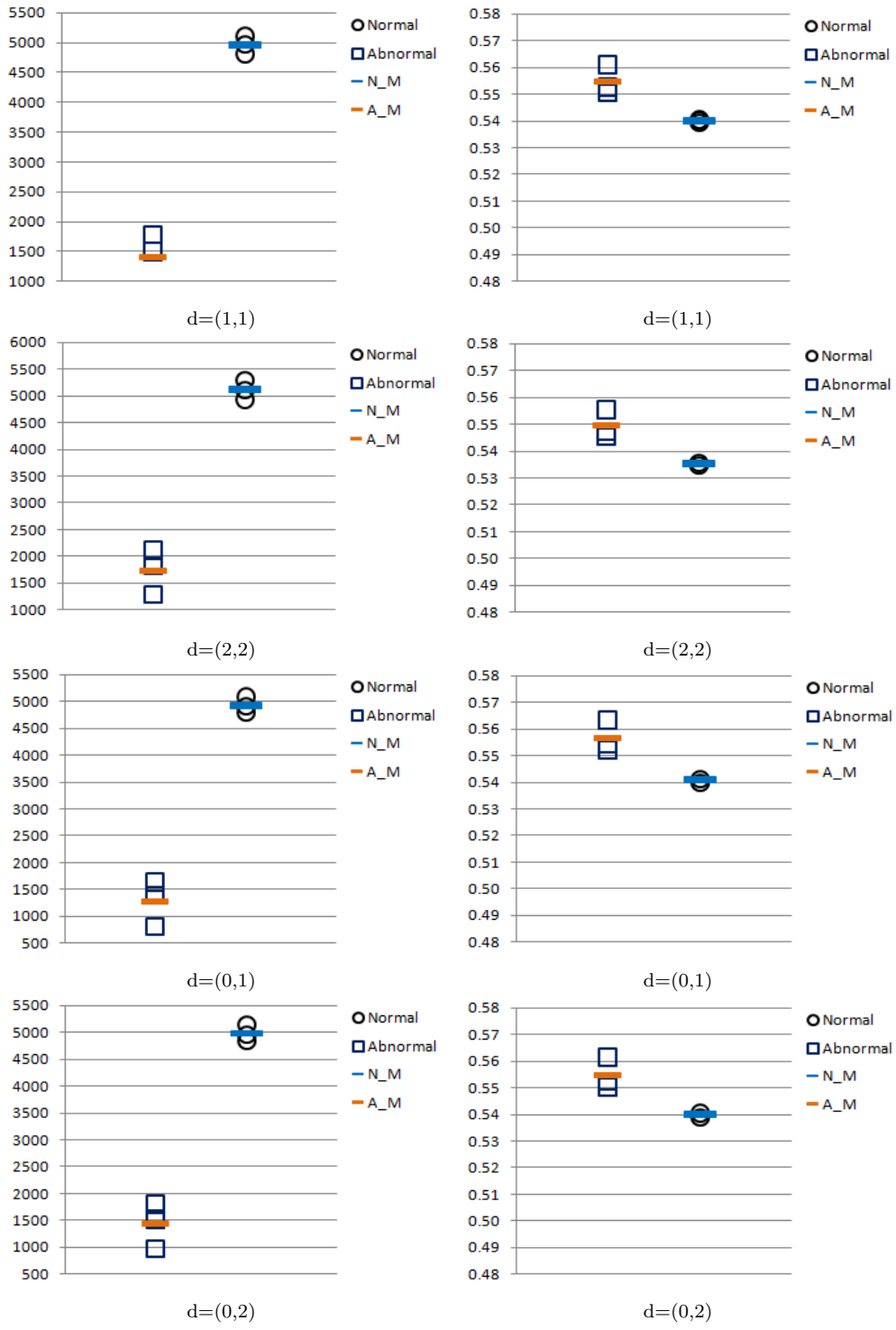

Figure 4.6: Left side plots for contrast and right side plots for homogeneity of the sample images, for the given d values, of Figure 4.4. *Normal*, *Abnormal*, N_M and A_M represents normal, abnormal, mean of normal and abnormal of sample images, respectively.

Figure 4.7: Left side plots for contrast and right side plots for homogeneity of the sample images, for the given d values, of Figure 4.4. *Normal*, *Abnormal*, N_M and A_M represents normal, abnormal, mean of normal and abnormal of sample images, respectively.

Fractal Dimension Method	
Samples	**Mean Slope Values**
N_Sample1	0.0960
N_Sample2	0.0936
N_Sample3	0.0903
A_Sample1	0.1289
A_Sample2	0.1332
A_Sample3	0.1466

Table 4.7: Results obtained using fractal dimension based texture measures for all generated sample images, represents the normal and abnormal group of images, of Figure 4.4.

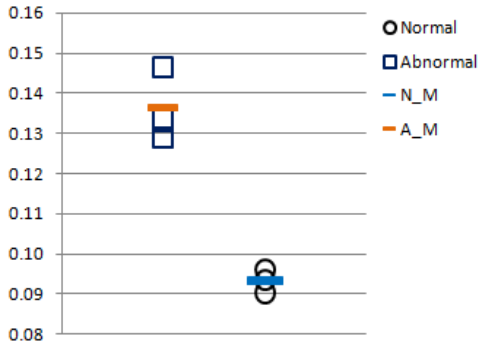

Figure 4.8: 2-sample scatter plot of the results of fractal dimension for the sample images of Figure 4.4. *Normal*, *Abnormal*, N_M and A_M represents normal, abnormal, mean of normal and abnormal of sample images, respectively.

4.5 Texture Analysis of DXA scan ROI Images Using The Proposed Partitioning Method

The γ_3 measure of the proposed partitioning method gives better performance, at $m = 16$, to distinguish normal and abnormal bone which is shown in the validation

results tabulated in Table 4.4 for the generated sample images of Figure 4.4.

The β, γ_1, γ_2 and γ_3 measures, using the proposed partitioning method (see Chapter 4, section 4.3), for the ROI images of Figures 3.6 and 3.7 are tabulated in Tables A.6 and A.7, respectively. From the tabulated results of hip ROIs, it is noticed that normal ROIs have $\gamma_3 > 0.2$ and osteoporotic ROIs have $\gamma_3 < 0.2$. On the other hand, from the tabulated results of spine ROIs, it is noticed that the γ_3 values do not show consistent differences between the normal and osteoporotic ROIs. Therefore, it is difficult to decide a threshold value for γ_3 from the tabulated results of spine ROIs. The spine is a more complicated composition of vertebrae and intervertebral discs. The vertebrae and intervertebral discs are not clearly visible in the spine ROIs. That's why there is a large overlap of the range of γ_3 for normal spine ROIs with the range of γ_3 for osteoporotic spine ROIs. The tabulated results of γ_3 of normal and osteoporotic hip ROIs are plotted in Figure 4.9 (a), using the 2-sample scatter plots. Similarly, the tabulated results of γ_3 of normal and osteoporotic spine ROIs are plotted in Figure 4.9 (b), using the 2-sample scatter plots.

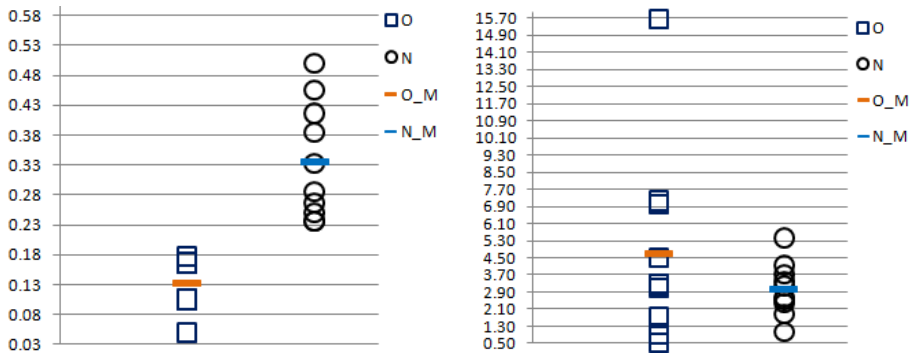

(a)For hip ROIs (b)For spine ROIs

Figure 4.9: Plotted the results of γ_3 obtained using the proposed partitioning method, where m=16, of normal and osteoporotic ROIs of Figures 3.6 and 3.7 in (a) and (b), respectively, using the scatter plots. N, O, N_M and O_M represents the normal, osteoporotic, mean of normal and osteoporotic of ROIs, respectively.

4.6 Two Variable Discriminant Tests

Two variable discriminant tests such as 2D plot, linear discriminant analysis, correlation matrix and principal component analysis were done using the experiment results of the proposed partitioning method of the ROI images of Figures 3.6 and 3.7. The 2D plot gives better result to show the discrepancies between the normal and osteoporotic ROIs compare to other two variable discriminant tests. Among these 2D plots are shown here.

To visualize the difference very well between the normal and osteoporotic ROI images, the results of γ_3 plotted with respect to γ_2 using the 2D plots shown in Figure 4.10.

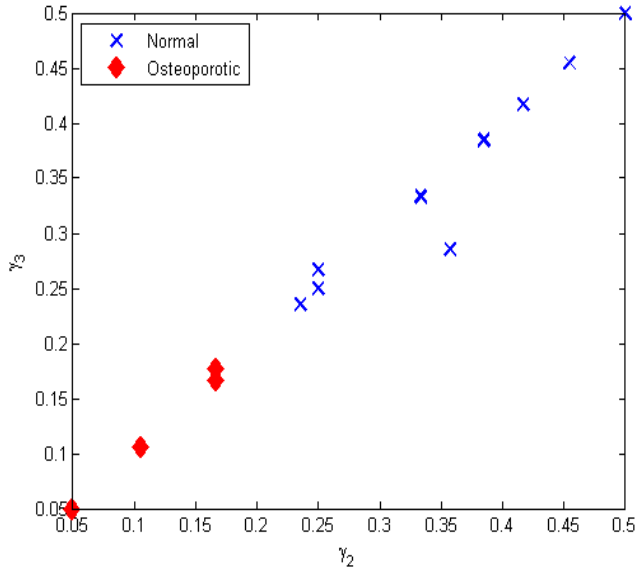

(a)For hip ROIs

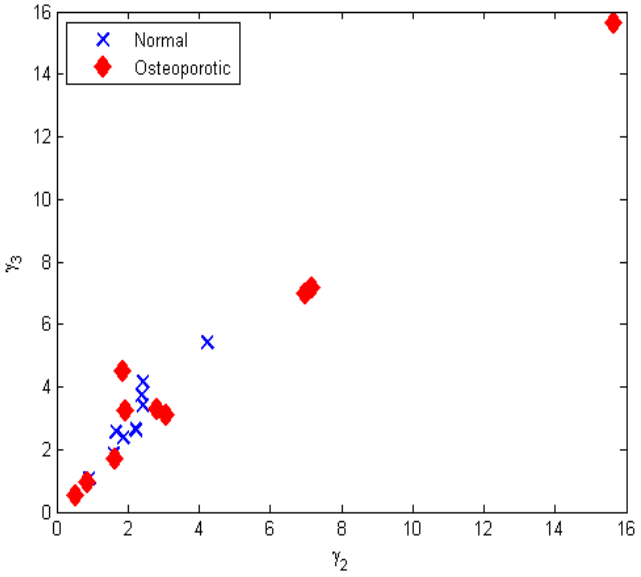

(b)For spine ROIs

Figure 4.10: Plotted the results of γ_2 and γ_3 obtained using the proposed partitioning method, where m=16, of normal and osteoporotic ROIs of Figures 3.6 and 3.7 in (a) and (b), respectively.

4.7 Statistical Analysis of the Experimented Results of ROI Images

Texture analysis on the ROI images using the proposed partitioning method is discussed above. The β, γ_1, γ_2 and γ_3 measures for the ROI images of Figures 3.6 and 3.7 are tabulated in Table A.6, for hip ROIs and Table A.7, for spine ROIs. The tabulated results are plotted in Figure 4.9 for hip and spine DXA scan ROI images.

For the two-sample t-test, the variances of γ_3 measures of the normal and osteoporotic ROIs are assumed to be the same. To test the homogeneity of variances of γ_3 measures, a F-ratio for γ_3 measures is calculated. The F-ratio tests were performed at 5% significance level ($\alpha = 0.05$) and the degrees of freedom (df) both for normal and osteoporotic ROIs is $(n-1) = 9$, because there are 10 samples of ROIs in each group. By F-ratio distribution table lookup [63], the critical value for df=(9,9), and α=0.05, is 3.1789.

The null and alternative hypotheses are

$$H_0 : The\ variances\ of\ \gamma_3\ of\ normal\ and\ osteoporotic\ ROIs\ are\ equal$$

$$H_a : The\ variances\ of\ \gamma_3\ of\ normal\ and\ osteoporotic\ ROIs\ are\ not\ equal$$

The F-ratio test results of γ_3 measures for the hip and spine ROIs are tabulated in Table 4.8. From the tabulated results, it is noticed that the calculated F-ratio value

is larger than the critical value $(-t_\alpha)$ 3.1789. Therefore, comparing the critical value $(-t_\alpha)$ and the F-ratio value it is noticed that the null hypothesis is rejected for the variance of γ_3 measures of hip ROIs of Figure 3.6 which means the variances of γ_3 measures of the normal ROIs are not equal or close to that of the osteoporotic hip ROIs.

Similarly, the F-ratio test results of γ_3 measures for the spine ROIs are tabulated in Table 4.8. From the tabulated results, it is noticed that the calculated F-ratio value, for all distances d, is larger than the critical value $(-t_\alpha)$ 3.1789. Therefore, comparing the critical value $(-t_\alpha)$ and the F-ratio value it is noticed that the null hypothesis is rejected for the variance of γ_3 measures of the spine ROIs which means the variances of contrast of the normal ROIs are not homogeneous to that of the osteoporotic spine ROIs.

Proposed Partitioning Method (F-ratio test)		
Measurement	Hip ROIs	Spine ROIs
F-ratio	5.183	12.979

Table 4.8: F-ratio results of γ_3 measures for all ROIs of Figures 3.6 and 3.7. The critical value $(-t_\alpha)$ for df=(9,9), and α=0.05, is 3.1789.

4.7.1 Mean, Standard Deviation and T-test

As mentioned above, the results of γ_1, γ_2 and γ_3 measures of the ROIs are close to each other, so only γ_3 measures are taken into account to distinguish normal and

osteoporotic ROIs. For the experiments, both one-sample and two-sample t-test are determined using the value of γ_3 obtained from the proposed partitioning method. Two-sample t-tests of γ_3 measures are determined for the ROIs of Figures 3.6 and 3.7. The two-sample t-test determines if there is any difference between the mean of the normal and osteoporotic ROIs. The t-tests were performed at 5% significance level ($\alpha = 0.05$) and the degrees of freedom is $(n + m - 2) = 18$ because there are 10 samples in each group of ROIs. By table lookup (Table III, page T-7 of [22]), the critical value for df=18 and α=0.05, is 2.101.

The null and alternative hypotheses are

$$H_0 : The\ mean\ of\ \gamma_3\ of\ normal\ and\ osteoporotic\ ROIs\ are\ equal$$

$$H_a : The\ mean\ of\ \gamma_3\ of\ normal\ and\ osteoporotic\ ROIs\ are\ not\ equal$$

The two-sample t-test results of γ_3 for all ROI images of Figures 3.6 and 3.7 are shown in Table 4.9. From the tabulated results, it is noticed that the mean of γ_3 of normal hip ROIs are not equal to that of the osteoporotic hip ROIs as the value of H is 1 while the mean of γ_3 of normal spine ROIs are equal or close to that of the osteoporotic spine ROIs as the value of H is 0.

From the tabulated results, it is noticed that the calculated t-value for hip ROIs is greater than the critical value $(-t_\alpha)$ 2.101. Therefore, comparing the critical value $(-t_\alpha)$ and the t-value it is noticed that the null hypothesis is rejected for the hip ROIs of Figure 3.6 which shows the mean of the normal ROIs are not equal to that

of the osteoporotic hip ROIs.

Similarly, from the tabulated results in Table 4.9, it is noticed that the calculated t-value for spine ROIs is smaller than the critical value $(-t_\alpha)$ 2.101. Therefore, comparing the critical value $(-t_\alpha)$ and the t-value it is noticed that the null hypothesis is accepted for the spine ROIs of Figure 3.7 which shows the mean of the normal ROIs are equal or close to that of the osteoporotic spine ROIs.

After analyzing the two-sample t-test results of the hip and spine ROIs of Table 4.9, it is noticed that the normal and osteoporotic hip ROIs have different mean of γ_3 while the mean of spine ROIs are the close.

Proposed Partitioning Method (Two-sample t-test)		
Measurement	Hip ROIs	Spine ROIs
t-value	6.2647	-0.356
H	1	0

Table 4.9: Two-sample t-test results of γ_3 of the partitioning method for all ROIs of Figures 3.6 and 3.7. H indicates whether the hypothesis is accepted or not. The critical value $(-t_\alpha)$ for df=18, and α=0.05, is 2.101.

A one-sample t-test was also done for the normal and osteoporotic ROIs separately, to test a threshold value for the γ_3 measures of the proposed partitioning method. The t-tests were performed at 5% significance level ($\alpha = 0.05$) and the degrees of freedom is $(n - 1) = 9$ because there are 10 samples in each group of ROIs. The critical value for df=9 and α=0.05, is 1.833 [22]. The values for the mean, standard deviation and one-sample t-test for the results of γ_3 of the proposed partitioning method for the ROI images of Figures 3.6 and 3.7 are shown in Table 4.10.

Proposed Partitioning Method (One-sample t-test)				
Measurement	Hip ROIs		Spine ROIs	
	N	O	N	O
$\bar{x}$	0.3216	0.1366	3.2048	6.2650
S	0.1149	0.0420	1.2808	7.2944
t-value	3.3448	-4.7761	7.4188	2.6293

Table 4.10: Mean, standard deviation and one-sample t-test results of γ_3 of the partitioning method for all ROIs of Figures 3.6 and 3.7. The critical value for df=18 and α=0.05, is 1.833

4.7.1.1 Normal vs. Osteoporotic Hip ROI

The mean ($\bar{x}$) obtained for the results of γ_3 of the partitioning method is 0.3216 for normal hip ROIs and 0.1366 for osteoporotic hip ROIs. The standard deviation (s) obtained for the results of γ_3 of the partitioning method is 0.1149 for normal hip ROIs and 0.0420 for osteoporotic hip ROIs.

Following are the results of the one-sample t-test for the above mentioned hip ROI images. The value of γ_3 used for the hypothesis is 0.2 which is taken based upon the experimental results of γ_3 of the partitioning method.

The null and alternative hypotheses are

$$H_0 : \mu = 0.2 \ \ (Normal)$$

$$H_a : \mu < 0.2 \ \ (Osteoporotic)$$

where μ is the value of γ_3 of partitioning method for hip ROIs.

The test is left-tailed because of the less-than sign ($<$) in the alternative hypothesis. The calculated t-value from the expression mentioned earlier is 3.3448, using the

mean and standard deviation of Table 4.10 of the normal hip ROIs. Therefore, comparing the critical value ($-t_\alpha$) and the t-value it is noticed that the null hypothesis is accepted for the normal hip ROIs of Figure 3.6 as the calculated t-value is greater than the critical value ($-t_\alpha$).

On the other hand, the calculated t-value obtained is -4.7761, using the mean and standard deviation of Table 4.10 of the osteoporotic hip ROIs. Therefore, comparing the critical value ($-t_\alpha$) and the t-value it is noticed that the null hypothesis is rejected for osteoporotic hip ROIs of Figure 3.6 as the calculated t-value is smaller than the critical value ($-t_\alpha$). Thus, if the value of γ_3 of hip ROI image is 0.2 or above then it is normal otherwise it is osteoporotic.

4.7.1.2 Normal vs. Osteoporotic Spine ROI

The mean ($\bar{x}$) obtained for the results of partitioning method is 3.2048 for normal spine ROIs and 6.2650 for osteoporotic spine ROIs. The standard deviation (s) is 1.2808 for normal spine ROIs and 7.2944 for osteoporotic spine ROIs.

From the one-sample t-test results for spine ROIs, it is noticed that the calculated t-value is larger than the critical value ($-t_\alpha$) both for normal and osteoporotic ROI images. Therefore, the one-sample t-test results obtained for the normal vs. osteoporotic spine ROIs are non-significant because of the large overlap of the range of γ_3 of the partitioning method for normal spine ROIs with the range of γ_3 for osteoporotic spine ROIs. Therefore, it is difficult to find a specific value for μ to set the null hypothesis for the left-tailed t-test.

4.8 Summary

After analyzing all the tabulated results of DXA scan ROI images using the proposed partitioning method, it is noticed that the proposed partitioning method shows a difference or pattern among the normal and osteoporotic hip ROI images. For the spine ROIs, the results are non-significant because of the large overlap of the range of γ_3 for normal ROIs with the range of γ_3 for osteoporotic ROIs. From the two-sample t-test results of the partitioning method, it is observed that the mean of γ_3 of the normal ROIs are equal to that of the osteoporotic ROIs. Moreover, from the one-sample t-test results of the partitioning method, it is found that if $\gamma_3 \geq 0.2$ then the hip ROIs are normal and if $\gamma_3 < 0.2$, then it is osteoporotic. However, the t-test results of spine ROIs are non-significant because of the large overlap of the range of γ_3 for normal ROIs with the range of γ_3 for osteoporotic ROIs. Thus, it is difficult to find a value for μ to set the hypothesis.

It is observed that the γ_3 measure of the proposed partitioning method is a promising measure to separate normal and osteoporotic ROIs. For spine ROIs, the co-occurrence matrix and fractal dimension based measure and the proposed partitioning methods did not show significant difference between the normal and osteoporotic ROI images; it may be that the intensity differences of the texture is not high enough between normal and osteoporotic spine ROI images. From the grey level intensity difference of normal and osteoporotic spine ROI images of Figure 3.7, it is noticed that the blur image area is larger than the light area.

If a bone scan image of a patient has $\gamma_3 \geq threshold$, the scan may be considered as normal; otherwise it would be considered as abnormal. Texture analyses using the proposed measures based on partitioning show better variations of grey scale patterns of pixels of normal and abnormal samples. Therefore, the diseased bone that is at risk of fracture due to the deterioration of trabecular structure can be identified from the variation of grey scale patterns of pixels, using the partitioning method.

Chapter 5

Conclusion

Although work have been done on texture analysis using existing texture measures such as those based on co-occurrence matrices and fractal dimension, these existing texture measures do not always show subtle variations of the texture of bone very well. Moreover, from the results of texture analysis using the contrast measure of co-occurrence matrices and the mean slope value of fractal dimension based measure, it is difficult to distinguish a normal bone scan image from an osteoporotic bone scan image because there is no specific grey scale pattern of pixels or threshold value that separate each other. This thesis proposes a partitioning method for defining texture measures of DXA images based on the variation of grey level patterns of pixels. These measures seem to produce better results and thresholds which help to discriminate normal and osteoporotic total hip DXA image.

From the tabulated and plotted results of Chapter 3, it is noticed that the discrimination of normal and osteoporotic ROI images is difficult from the contrast results

of co-occurrence matrices of ROIs. However, it is not easy to determine a single grey scale pattern of pixels or threshold value that independently can discriminates all osteoporotic bone scan images from all normal bone scan images using the contrast measure of co-occurrence matrices and the mean slope value of fractal dimension based measure. The texture analysis of normal and osteoporotic bone scan images using the contrast measure of co-occurrence matrices and the mean slope value of fractal dimension based measure did not contribute any grey scale patterns of pixels, for the observed normal and osteoporotic ROIs and the considered parameters (distance, contrast, homogeneity and slope value), that independently discriminate the normal and osteoporotic ROIs.

From the statistical analytical test results of Chapter 3, it is observed that for the DXA scan hip ROI images, the group mean of contrast of normal ROI is higher than the group mean of contrast of osteoporotic ROI images. The group mean of contrast results of spine ROIs do not seem to show better difference because the range of contrast value of co-occurrence matrices for normal spine ROIs have large overlaps with the range of corresponding contrast values for osteoporotic spine ROIs. The homogeneity results of co-occurrence matrices do not show any pattern between the normal and osteoporotic ROIs. The fractal dimension does not show any significant difference between normal and osteoporotic ROIs.

In Chapter 4, the existing quad-tree decomposition and the proposed rectangular segmentation methods were used to get a suitable ROI segment, where most frac-

tures occur, from a DXA image. The results of the quad-tree decomposition and the proposed rectangular segmentation methods show that it is hard to get the required ROI from the whole DXA image using the segmentation technique. Therefore, the ROI image was cropped from the DXA image to apply the texture measures on those ROIs for texture analysis. A partitioning method is proposed for texture analysis of DXA scan ROI images.

From the validation test results of Chapter 4, it is noticed that texture measures using the partitioning method look promising to detect normal and abnormal samples. The partitioning method shows better performance for bone scans of sufficiently high resolutions where the grey level intensity difference is high between normal and osteoporotic bone scans. The experimental results discussed in Chapter 4 for the ROIs show differences between the normal and osteoporotic hip ROIs. The γ_3 measure looks promising for hip ROIs to discriminate the normal and osteoporotic ROI images. For the observed samples of hip ROIs of Figure 3.6, if $\gamma_3 > 0.2$ then the bone of that hip ROI is presumed to be normal and if $\gamma_3 < 0.2$ then it is presumed to be abnormal or osteoporotic. The results are inconsistent for the observed samples of spine ROIs of Figure 3.7.

From the statistical analytical test results of Chapter 4, it is observed that for the DXA scan hip ROI images, the partitioning method seem to show better variation of grey level patterns of pixels to distinguish the osteoporotic and normal ROIs. The threshold value of γ_3 of the partitioning method selected for the t-test is able to dis-

tinguish the observed normal and osteoporotic hip ROI images of bone. For the DXA scan spine ROI images, the partitioning method do not seem to show better variation of grey level patterns of pixels to discriminate the osteoporotic and normal ROIs; it may be that the intensity differences of the texture is not high enough between normal and osteoporotic spine ROI images.

In general, the threshold value selected for the t-test of the partitioning method gives better results than the contrast measure of co-occurrence matrices and the mean slope value of fractal dimension based measure for the observed ROI samples and considered parameters (γ_3), to distinguish the normal and osteoporotic hip ROI images. The threshold value of γ_3 depends on the type of bone scan image. The main idea of using the proposed method for screening patients is that if a bone scan image of a patient has $\gamma_3 \geq threshold$ then the bone is considered to be normal; otherwise the bone is considered to be abnormal, so the bone of that patient need further examination.

There are some limitations of the proposed partitioning method. The first limitation is that the grey level threshold values used for the experiment may not work for all DXA images. The second limitation is that the γ_3 value that is obtained from the experiment results may not be the same to separate the normal and osteoporotic ROIs for all DXA images as they were obtained from a small number of samples. Finally, γ_3 measure of the partitioning method is indirectly BMD dependent.

The effectiveness of γ_i measure of the partitioning method will be tested by conducting experiments on a large samples of DXA images and comparing the obtained discrimination between normal and osteoporotic ROIs with the grouping of DXA images obtained using the other texture analysis measures. More experiments with various values of m and formulations for γ_i and consistency intervals could be conducted to refine the proposed method for more accurate values to predict risk of fracture, osteoporosis and related problems. Experiments on a large number of samples could be conducted to determine a γ_i value that will work as threshold value, to separate normal and osteoporotic DXA scan ROIs, for all DXA images. For experiment, however, the values used for the consistency intervals were $a_i = 0.25i$, where $i = 0, \cdots\cdots, L = 10$. The consistency interval can be changed by varying the value of a_i. More experiments on a large number of samples by varying the consistency intervals could be conducted to determine a more accurate γ_i measure that will work as a threshold value to demonstrate the discrepancy between the normal and osteoporotic DXA scan ROIs.

Appendix A

Numerical Results

The numerical results of Chapter 3 and 4 are tabulated here. The scatter plots of Figures 3.10, 3.11, 3.12 and 3.13 are plotted using the data tabulated in Tables A.1, A.2, A.3, and A.4, respectively. Table A.5 shows the values plotted in Figure 3.18. Tables A.6 and A.7 show the values plotted in Figure 4.9 (a), and (b), respectively. Tables A.1 and A.4 show the values plotted in the Figure 4.9 (a), and (b), respectively. The values plotted in Figure 4.10 (a), and (b), respectively, are shown in Tables A.6 and A.7 too. The mean, standard deviation, coefficient of variation and t-test results of the contrast for all ROIs of Tables 3.3 are tabulated in Tables A.1 and A.2. Similarly, the results of Table 3.4 used the data tabulated in Tables A.3 and A.4. The mean, standard deviation and t-test results of Tables 4.9 and 4.10 are obtained from the tabulated γ_3 measures of the partitioning method in Tables A.6 and A.7.

Co-occurrence Matrix								
	d=(1,1)		d=(2,2)		d=(0,1)		d=(0,2)	
Images	Contrast	Homogeneity	Contrast	Homogeneity	Contrast	Homogeneity	Contrast	Homogeneity
FN1	43.506	0.342	125.022	0.248	18.364	0.400	57.695	0.285
FN2	31.486	0.369	101.315	0.266	17.069	0.430	57.549	0.320
FN3	36.229	0.306	112.681	0.219	22.433	0.377	74.978	0.256
FN4	26.239	0.370	78.779	0.261	12.828	0.448	41.528	0.321
FN5	38.053	0.350	116.519	0.247	23.723	0.434	76.152	0.315
FN6	34.906	0.348	109.092	0.248	22.842	0.402	72.498	0.275
FN7	32.518	0.385	103.974	0.277	16.498	0.458	58.416	0.327
FN8	65.742	0.334	214.346	0.234	38.591	0.382	128.341	0.266
FN9	47.408	0.345	143.012	0.239	23.194	0.475	72.394	0.343
FN10	38.053	0.341	116.011	0.241	17.364	0.404	56.296	0.284
FO1	34.281	0.348	111.805	0.248	21.999	0.434	77.933	0.315
FO2	23.041	0.375	72.557	0.269	14.514	0.442	48.538	0.313
FO3	18.596	0.407	58.487	0.298	10.099	0.503	32.494	0.369
FO4	40.839	0.294	109.285	0.206	27.503	0.359	75.849	0.254
FO5	20.324	0.381	65.153	0.284	14.704	0.430	48.761	0.308
FO6	16.279	0.364	53.007	0.253	6.655	0.474	20.848	0.348
FO7	28.192	0.345	87.009	0.248	13.719	0.431	46.693	0.312
FO8	17.561	0.383	53.137	0.289	12.380	0.443	38.449	0.328
FO9	28.314	0.352	88.033	0.251	15.570	0.451	52.361	0.326
FO10	21.468	0.350	66.237	0.252	12.587	0.412	41.286	0.292

Table A.1: Results obtained using co-occurrence based texture measures for all hip ROI images in Figure 3.6 for distance d=(1,1), d=(2,2), d=(0,1) and d=(0,2).

Co-occurrence Matrix								
	d=(1,0)		d=(2,0)		d=(3,3)		d=(4,4)	
Images	Contrast	Homogeneity	Contrast	Homogeneity	Contrast	Homogeneity	Contrast	Homogeneity
FN1	23.869	0.402	69.968	0.284	200.554	0.205	270.146	0.186
FN2	13.004	0.441	43.319	0.323	189.283	0.210	289.118	0.183
FN3	13.868	0.408	42.741	0.294	201.626	0.180	299.003	0.158
FN4	12.604	0.467	38.048	0.336	141.606	0.218	215.248	0.184
FN5	13.363	0.449	44.539	0.315	208.184	0.216	314.188	0.188
FN6	11.124	0.449	37.546	0.319	193.096	0.206	283.242	0.180
FN7	12.327	0.468	40.093	0.340	195.912	0.236	304.360	0.209
FN8	16.668	0.439	58.345	0.313	389.294	0.190	572.960	0.165
FN9	17.318	0.445	54.355	0.310	257.207	0.191	382.176	0.163
FN10	16.032	0.437	48.602	0.312	201.527	0.193	287.854	0.159
FO1	10.743	0.436	34.569	0.316	211.820	0.209	322.379	0.187
FO2	7.119	0.470	20.797	0.347	130.644	0.227	195.792	0.200
FO3	11.868	0.454	40.292	0.334	108.748	0.249	164.711	0.223
FO4	16.608	0.376	54.146	0.272	178.141	0.165	248.475	0.147
FO5	4.327	0.549	12.228	0.410	123.127	0.243	192.380	0.215
FO6	9.820	0.442	33.151	0.318	98.669	0.211	146.845	0.189
FO7	18.205	0.390	58.610	0.276	158.320	0.205	235.564	0.175
FO8	6.649	0.484	20.718	0.350	93.683	0.247	136.845	0.221
FO9	11.535	0.451	35.260	0.327	155.668	0.200	226.386	0.168
FO10	9.535	0.444	29.951	0.325	115.781	0.200	168.372	0.170

Table A.2: Results obtained using co-occurrence based texture measures for all hip ROI images in Figure 3.6 for distance d=(1,0), d=(2,0), d=(3,3) and d=(4,4).

Co-occurrence Matrix								
Images	**d=(1,1)**		**d=(2,2)**		**d=(0,1)**		**d=(0,2)**	
	Contrast	**Homogeneity**	**Contrast**	**Homogeneity**	**Contrast**	**Homogeneity**	**Contrast**	**Homogeneity**
SN1	152.901	0.180	510.933	0.117	48.096	0.257	167.243	0.170
SN2	100.718	0.208	327.800	0.144	38.933	0.272	135.509	0.181
SN3	163.358	0.177	509.397	0.122	70.432	0.233	233.575	0.155
SN4	169.820	0.173	537.681	0.117	56.876	0.246	191.217	0.167
SN5	182.807	0.174	607.940	0.117	59.247	0.256	210.518	0.169
SN6	137.323	0.191	448.631	0.123	49.621	0.266	171.630	0.178
SN7	126.012	0.202	410.730	0.132	38.447	0.296	130.028	0.200
SN8	135.035	0.198	446.187	0.132	52.561	0.262	186.255	0.173
SN9	138.958	0.192	462.644	0.127	47.438	0.268	166.604	0.179
SN10	131.517	0.191	418.827	0.130	48.461	0.261	159.620	0.178
SO1	164.758	0.186	517.554	0.126	42.620	0.277	137.439	0.189
SO2	105.519	0.211	349.008	0.140	32.378	0.289	112.113	0.194
SO3	179.461	0.179	584.535	0.118	56.442	0.264	186.431	0.179
SO4	201.228	0.163	636.494	0.108	39.823	0.279	132.996	0.191
SO5	125.431	0.202	402.352	0.135	39.378	0.288	135.015	0.199
SO6	73.715	0.239	238.270	0.161	27.655	0.308	95.322	0.211
SO7	190.668	0.173	622.828	0.116	50.741	0.273	172.490	0.184
SO8	140.271	0.191	457.230	0.128	32.465	0.295	108.397	0.199
SO9	206.610	0.168	677.232	0.108	49.168	0.270	172.343	0.181
SO10	93.922	0.215	303.878	0.145	21.393	0.340	71.721	0.235

Table A.3: Results obtained using co-occurrence based texture measures for all spine ROI images in Figure 3.7 for distance d=(1,1), d=(2,2), d=(0,1) and d=(0,2).

Co-occurrence Matrix								
	d=(1,0)		d=(2,0)		d=(3,3)		d=(4,4)	
Images	Contrast	Homogeneity	Contrast	Homogeneity	Contrast	Homogeneity	Contrast	Homogeneity
SN1	103.876	0.204	358.807	0.136	940.876	0.093	1354.391	0.078
SN2	64.343	0.247	218.619	0.168	595.033	0.119	861.072	0.099
SN3	100.166	0.208	325.515	0.138	898.124	0.097	1278.074	0.086
SN4	116.043	0.201	383.713	0.135	926.820	0.097	1250.650	0.086
SN5	121.622	0.207	414.432	0.137	1090.408	0.088	1516.340	0.078
SN6	86.764	0.217	296.002	0.147	796.652	0.097	1101.485	0.085
SN7	87.341	0.223	300.703	0.150	733.785	0.107	1022.863	0.089
SN8	88.344	0.227	306.815	0.151	798.292	0.104	1110.160	0.088
SN9	89.431	0.222	311.491	0.147	841.843	0.101	1191.870	0.085
SN10	85.382	0.228	289.523	0.149	746.616	0.104	1064.698	0.093
SO1	122.968	0.214	411.891	0.141	885.002	0.104	1174.818	0.092
SO2	72.785	0.245	249.116	0.161	626.160	0.110	872.767	0.095
SO3	125.628	0.204	430.512	0.134	1053.307	0.095	1479.072	0.083
SO4	161.321	0.179	530.030	0.119	1072.834	0.087	1401.530	0.079
SO5	92.415	0.223	311.468	0.150	703.526	0.110	966.807	0.098
SO6	50.868	0.272	169.918	0.185	424.249	0.131	595.145	0.116
SO7	139.312	0.195	470.688	0.131	1091.605	0.090	1474.038	0.078
SO8	112.575	0.212	379.588	0.140	822.016	0.099	1144.589	0.087
SO9	162.060	0.182	547.807	0.119	1202.922	0.088	1664.855	0.077
SO10	76.261	0.242	255.912	0.164	536.166	0.119	731.994	0.105

Table A.4: Results obtained using co-occurrence based texture measures for all spine ROI images in Figure 3.7 for distance d=(1,0), d=(2,0), d=(3,3) and d=(4,4).

ROI Image	Mean Slope	ROI Image	Mean Slope
FN1	0.95	SN1	0.86
FN2	0.91	SN2	0.88
FN3	0.94	SN3	0.87
FN4	1.02	SN4	0.84
FN5	0.99	SN5	0.89
FN6	0.96	SN6	0.83
FN7	0.98	SN7	0.89
FN8	1.00	SN8	0.88
FN9	1.02	SN9	0.91
FN10	0.96	SN10	0.86
FO1	0.91	SO1	0.83
FO2	0.94	SO2	0.87
FO3	0.88	SO3	0.89
FO4	0.89	SO4	0.80
FO5	0.93	SO5	0.82
FO6	0.90	SO6	0.85
FO7	0.92	SO7	0.92
FO8	0.81	SO8	0.81
FO9	0.95	SO9	0.89
FO10	0.87	SO10	0.87

Table A.5: Results obtained using fractal dimension based texture measures for all ROI images of Figures 3.6 and 3.7.

Proposed Partitioning Method				
ROI Image	*m=16*			
	β	$\gamma 1$	$\gamma 2$	$\gamma 3$
FN1	0.2528	0.3333	0.3333	0.3333
FN2	0.0396	0.3333	0.3571	0.2857
FN3	0.0210	0.2353	0.2353	0.2353
FN4	0.0416	0.2500	0.2500	0.2500
FN5	0.1452	0.3333	0.3846	0.3846
FN6	0.3548	0.5455	0.4545	0.4545
FN7	0.1509	0.2500	0.2500	0.2667
FN8	0.0926	0.2353	0.2353	0.2353
FN9	0.1822	0.3846	0.4167	0.4167
FN10	0.0764	0.5000	0.5000	0.5000
FO1	0.0384	0.1667	0.1667	0.1765
FO2	0.0315	0.1667	0.1667	0.1667
FO3	0.0148	0.1053	0.1053	0.1053
FO4	0.0077	0.1053	0.1053	0.1053
FO5	0.0097	0.1053	0.1053	0.1053
FO6	0.0009	0.0500	0.0500	0.0500
FO7	0.0282	0.1667	0.1667	0.1667
FO8	0.0095	0.1667	0.1667	0.1667
FO9	0.0241	0.1667	0.1667	0.1667
FO10	0.0066	0.1053	0.1053	0.1053

Table A.6: Tabulated the results of β, γ_1, γ_2 and γ_3 that obtained using a proposed partitioning method, where m=16, of normal and osteoporotic hip ROIs of Figure 3.6.

Proposed Partitioning Method				
ROI Image	*m=16*			
	β	$\gamma 1$	$\gamma 2$	$\gamma 3$
SN1	6.6475	1.2273	1.5882	1.8571
SN2	7.5941	2.3333	2.9167	3.1818
SN3	3.5301	2.1250	2.2143	2.6364
SN4	3.8773	1.6316	1.6667	2.5455
SN5	5.1034	1.3810	1.8667	2.3636
SN6	16.8418	4.0000	4.2222	5.4286
SN7	0.8584	0.9231	0.9091	1.0556
SN8	15.9755	1.5000	2.4167	4.1429
SN9	5.9701	2.1250	2.4286	3.4000
SN10	3.8608	1.9412	2.3846	3.7500
SO1	3.5613	1.2727	1.8667	4.5000
SO2	1.6022	1.8824	1.6250	1.7143
SO3	71.7692	6.1429	7.1667	7.1667
SO4	28.0565	6.1429	7.0000	7.0000
SO5	4.5033	3.1667	3.0909	3.1000
SO6	0.1734	0.5313	0.5333	0.5172
SO7	9.5251	2.1250	2.8333	3.3000
SO8	182.7368	15.6667	15.6667	15.6667
SO9	3.6384	1.5000	1.9333	3.2500
SO10	0.3834	0.8148	0.8636	0.9444

Table A.7: Tabulated the results of β, γ_1, γ_2 and γ_3 that obtained using a proposed partitioning method, where m=16, of normal and osteoporotic spine ROIs of Figure 3.7.

Bibliography

[1] Jerrold T. Bushberg, J. Anthony Seibert, Edwin M. Leidholdt, Jr., and John M. Boone. *The Essential Physics of Medical Imaging*. Lippincott Williams and Wilkins, second edition, 2002.

[2] Jason C. Eck. Bone Density Scan. `http://www.medicinenet.com/bone_density_scan/article.htm`. Accessed on 17.12.08.

[3] J. Stein Carter. Bones and skeletal system. `http://www.biology.clc.uc.edu/Courses/bio105/bone.htm`. Accessed on 17.12.08.

[4] CliffsNotes. Bone structure. `http://www.cliffsnotes.com/WileyCDA/CliffsReviewTopic/Bone-Structure.topicArticleId-22032,articleId-21902.html`. Accessed on 16.01.09.

[5] Aziz Nather, H.J.C. Ong, and Zameer Aziz. Structure of bone. `http://www.worldscibooks.com/medsci/etextbook/5695/5695_chap01.pdf`. Accessed on 17.12.08.

[6] Bupa. Osteoporosis. `http://hcd2.bupa.co.uk/fact_sheets/html/Osteoporosis.html`. Accessed on 16.01.09.

[7] R. Karunanithi, S. Ganesan, T.M.R. Panicker, M. Paul Korath, and K. Jagadeesan. Assessment of bone mineral density by DXA and the trabecular microarchitecture of the calcaneum by texture analysis in pre and postmenopausal women in the evaluation of osteoporosis. *Journal of Medical Physics*, 32(4):161–168, October 2007.

[8] Ann Cranney, Sophie A. Jamal, James F. Tsang, Robert G. Josse, and William D. Leslie. Low bone mineral density and fracture burden in postmenopausal women. *Canadian Medical Association Journal (CMAJ)*, 177(6):575–580, September 2007.

[9] D.J. Baylink and K.H W. Lau. The diagnosis and management of osteoporosis. *Zeitschrift für Rheumatologie*, 59(7):142–144, February 2000.

[10] Jacques P. Brown, Robert G. Josse, and The Scientific Advisory Council of the Osteoporosis Society of Canada. 2002 clinical practice guidelines for the diagnosis and management of osteoporosis in Canada. *Canadian Medical Association Journal*, 167(10):1–34, November 2002.

[11] Osteoporosis Society of Canada. Osteoporosis to the third millennium: Priorities for prevention and treatment. *Summary Report*, pages 1–12, 1996.

[12] Kate Lindemann. Osteopenia - osteopenia treatments. `http://www.osteopenia3.com/medical-definitions-osteopenia.html`. Accessed on 21.01.10.

[13] Manitoba Health. Bone density testing information for professionals. `http:`

//www.gov.mb.ca/health/bonedensity/report.html#definition. Accessed on 21.01.10.

[14] The University Of Kansas Medical Center (KU Medical Center). Osteoporosis. http://www2.kumc.edu/coa/Education/AMED900/Osteoporosis.htm. Accessed on 16.01.09.

[15] S.E. Smith. What is a dxa scan? http://www.wisegeek.com/what-is-a-dxa-scan.htm. Accessed on 13.06.10.

[16] Healthline. Dual-energy x-ray absorptiometry (dexa). http://www.healthline.com/hlbook/nut-dual-energy-x-ray-absorptiometry-dexa. Accessed on 13.06.10.

[17] Society for Endocrinology BES 2009. The limitations of dxa for body composition assessment. http://www.endocrine-abstracts.org/ea/0019/ea0019s78.htm. Accessed on 31.07.10.

[18] Natural Resources Canada. Canada centre for remote sensing. http://www.ccrs.nrcan.gc.ca/resource/tutor/fundam/chapter4/07_e.php. Accessed on 29.08.10.

[19] R. Fisher, S. Perkins, A. Walker, and E. Wolfart. Image synthesis. http://homepages.inf.ed.ac.uk/rbf/HIPR2/snthops.htm. Accessed on 29.08.10.

[20] Mihran Tuceryan and Anil K. Jain. *The Handbook of Pattern Recognition and Computer Vision, by C. H. Chen, L. F. Pau, P. S. P. Wang (eds.)*, chapter 2.1, pages 207–248. World Scientific Publishing Co., second edition, 1998.

[21] John C. Russ. *The Image Processing Handbook*. CRC Press Inc., first edition, 1992.

[22] Neil A. Weiss. *Elementary Statistics*. Addison-wesley Publishing Company, first edition, 1989.

[23] AcaStat Software. Computing f-ratio. `http://www.acastat.com/Statbook/fratio.htm`. Accessed on 31.07.10.

[24] Carol A. Markowski and Edward P. Markowski. Conditions for the effectiveness of a preliminary test of variance. *The American Statistician*, 44(4):322–326, 1990.

[25] Chew Jian Chieh. Making sense of the two-sample t-test. `http://www.isixsigma.com/index.php?option=com_k2&view=item&id=988:making-sense-of-the-two-sample-t-test&Itemid=155`. Accessed on 13.06.10.

[26] The MathWorks. Statistics toolbox. `http://www.mathworks.it/access/helpdesk/help/toolbox/stats/ttest2.html`. Accessed on 10.06.10.

[27] The MathWorks. Statistics toolbox. `http://www.mathworks.de/access/helpdesk_r13/help/toolbox/stats/ttest2.html`. Accessed on 10.06.10.

[28] Laurent Pothuaud. Process of interpretation of two-dimensional densitometry image for the prediction of bone mechanical strength. In *Proceedings of the* 7^{th} *International Conference on Medical Image Computing and Computer-Assisted Intervention (MICCAI)*, pages 1079–1080, September 2004.

[29] Manitoba Health. Manitoba bone density program. `http://www.gov.mb.ca/health/bonedensity/index.html`.. Accessed on 17.12.08.

[30] I. Lima, R. Lopes, and L. Oliveira. *Proceedings of the 2005 International Symposium on Mathematical and Computational Biology BIOMAT 2005*, chapter Characterization of the Bone Trabecular Structure: A Method with 3D Microtomography, pages 112–140. E-papers Servicos Editoriais Ltda., first edition, 2006.

[31] Janet Cochrane Miller. Radiology rounds. *A Newsletter for Referring Physicians*, 3(8):1–3, August 2005.

[32] P. Fratzl and O. Paris. *Neutron scattering in biology: techniques and applications*, chapter Complex Biological Structures: Collagen and Bone, pages 205–223. Springer, first edition, 2006.

[33] E.A. Papadimitropoulos, P.C. Coyte, R.G. Josse, and C.E. Greenwood. Current and projected rates of hip fracture in Canada. *Canadian Medical Association Journal*, 157(10):1357–1363, November 1997.

[34] Osteoporosis Society of Canada. Clinical practice guidelines for the diagnosis and management of osteoporosis. *Canadian Medical Association Journal*, 155(8):1113–33, April 1996.

[35] E. Lespessailles, C. Gadois, I. Kousignian, J. P. Neveu, P. Fardellone, S. Kolta, C. Roux, J. P. Do-Huu, and C. L. Benhamou. Clinical interest of bone tex-

ture analysis in osteoporosis: A case control multicenter study. *Osteoporosis International*, 19(7):1019–1028, July 2008.

[36] Laurent Pothuaud, Pascal Carceller, and Didier Hans. Correlations between grey-level variations in 2D projection images (TBS) and 3D microarchitecture: Applications in the study of human trabecular bone microarchitecture. *Bone*, 42(4):775–787, April 2008.

[37] Laurent Pothuaud. Process of interpretation of two-dimensional densitometry image for the prediction of bone mechanical strength. In *Proceedings of the* 7^{th} *International Conference on Medical Image Computing and Computer-Assisted Intervention (MICCAI)*, pages 1079–1080, September 2004.

[38] Tamara J. Vokes, Ann Pham, Joel Wilkies, Masha Kocherginsky, Siu-Ling Ma, Michael Chinander, Theodore Karrison, Octavia Bris, and Maryellen L. Giger. Reproducibility and sources of variability in radiographic texture analysis of densitometric calcaneal images. *Journal of Clinical Densitometry: Assessment of Skeletal Health*, 11(2):211–220, April 2008.

[39] Philip Caligiuri, Maryellen L. Giger, Murra J. Favus, Hong Jia, Kunio Dio, and Larry B. Dixon. Computerized radiographic analysis of osteoporosis: Preliminary evaluation. *Radiology*, 186(2):471–474, February 1993.

[40] WD Leslie, C. Metge, and L. Ward. Contribution of clinical risk factors to bone density-based absolute fracture risk assessment in postmenopausal women. *Osteoporosis International*, 14(4):334–338, June 2003.

[41] Chi-Men Pun and Chan-Fong Wong. Content-based image retrieval using rectangular segmentation. *International Journal Of Computers*, 2(1):74–79, February 2008.

[42] John A. Kanis, Frederik Borgstrom, Chris De Laet, and et al. Assessment of fracture risk. *Osteoporosis International*, 16(6):581–589, June 2005.

[43] Black DM, Steinbuch M, Palermo L, and et al. An assessment tool for predicting racture risk in postmenopausal women. *Osteoporosis International*, 12(7):519–528, 2001.

[44] Siminoski K, Leslie WD, Frame H, and et al. Recommendations for bone mineral density reporting in canada. *Canadian Association of Radiologists Journal*, 56(3):178–188, June 2005.

[45] UK University of Sheffield. Frax. `http://www.shef.ac.uk/FRAX/.` Accessed on 26.07.10.

[46] William D. Leslie, Colleen Metge, Elizabeth A. Salamon, and C. Kin Yuen. Bone mineral density testing in healthy postmenopausal women: The role of clinical risk factor assessment in determining fracture risk. *Journal of Clinical Densitometry*, 5(2):117–131, July 2002.

[47] Pedro F. Felzenszwalb and Daniel P. Huttenlocher. Efficient graph-based image segmentation. *International Journal of Computer Vision*, 59(2):167–181, September 2004.

[48] Mustafa Özden and Ediz Polat. Image segmentation uing color and texture

features. In *Proceedings of the* 13^{th} *European Signal Processing Conference (EUSIPCO'05)*, September 4–8 2005.

[49] D. Comanicui and P. Meer. Mean shift: A robust approach toward feature space analysis. *IEEE Transaction on Pattern Analysis and Machine Intelligence (PAMI)*, 24(5):603–619, May 2002.

[50] J. Chen, T. N. Pappas, A. Mojsilovic, and B. Rogowitz. Adaptive perceptual color-texture image segmentation. *IEEE Transactions on Image Processing*, 14(10):1524–1536, October 2005.

[51] Jianbo Shi and Jitendra Malik. Normalized cuts and image segmentation. *IEEE Transactions on Pattern Analysis and Machine Intelligence*, 22(8):888–905, August 2000.

[52] John R. Smith and Shih-Fu Chang. Quad-tree segmentation for texture-based image query. In *Proceedings of the Second ACM International Conference on Multimedia (MULTIMEDIA '94)*, pages 279–286, October 1994.

[53] Erik Lieng. *Image Analysis*, chapter Quadtree Decomposition Texture Analysis in Paper Formation Determination, pages 215–273. Springer Berlin / Heidelberg, first edition, 2003.

[54] Anil K. Jain and Kalle Karu. *Image analysis and processing By Carlo Braccini, Leila DeFloriani, Gianni Vernazza (eds.)*, chapter Texture Analysis: Representation and Matching, pages 3–10. Springer, first edition, 1995.

[55] G. N. Srinivasan and Shobha G. Statistical texture analysis. *Proceedings of*

world academy of science, engineering and technology (PWASET), 36(1):1264–1269, December 2008.

[56] S. Kitaguchi, S. Westland, and M.R. Luo. Suitability of texture analysis methods for perceptual texture. In *Proceedings of the* 10^{th} *Congress of the International Colour Association AIC Colour 05*, pages 923–926, May 2005.

[57] MERCK. Hip fractures. `http://www.merck.com/mmhe/sec24/ch299666/ch299666d.html`. Accessed on 28.07.10.

[58] MERCK. Compression fractures of the spine. `http://www.merck.com/mmhe/sec24/ch299666/ch299666f.html`. Accessed on 28.07.10.

[59] Mihran Tuceryan and Anil K. Jain. *The Handbook of Pattern Recognition and Computer Vision, by C. H. Chen, L. F. Pau, P. S. P. Wang (eds.)*, chapter Texture Analysis, pages 207–248. World Scientific Publishing Co., second edition, 1998.

[60] Robert M. Haralick. Statistical and structural approaches to texture. *Proceedings of the IEEE*, 67(5):786–804, May 1979.

[61] The MathWorks. Image processing toolbox. `http://www.mathworks.com/access/helpdesk/help/toolbox/images/index.html?/access/helpdesk/help/toolbox/images/qtdecomp.html&http://www.google.ca/search?sourceid=navclient&aq=h0&oq=qua&ie=UTF-8&rlz=1T4ADBF_enCA256CA265&q=quadtree+decomposition`. Accessed on 10.02.09.

[62] A. Materka and M. Strzelecki. Texture analysis methods: A review. Technical University of Lodz (1998), COST B11 Report.

[63] StatSoft Electronic Statistics Textbook. Distribution tables. `http://www.statsoft.com/textbook/distribution-tables/`. Accessed on 31.07.10.

[64] Rafael C. Gonzalez and Richard W. Woods. *Digital Image Processing*. Prentice Hall, second edition, 2002.

[65] F. Jahan and D.J. Walton. Texture analysis of osteoporotic bone scan images vs. normal bone scan images. In *Proceedings of the Ninth IASTED International Conference on Visualization, Imaging, and Image Processing (VIIP 2009)*, pages 1–6, Cambridge, UK, July 2009.